Mechanistic Studies of Tellurite-Based Glasses for Enhancing Visible Transparency and Ionic Conductivity

by

Xuanzhao Pan

A thesis submitted for the
degree of Doctor of Philosophy

In the

Faculty of Sciences

School of Physical Sciences

September 2021

Supervisors:

Heike Ebendorff-Heidepriem

Jiangbo (Tim) Zhao

Bruno Poletto Rodrigues

Abstract

TeO_2-based glasses have attracted growing attention due to their unique combination of properties (e.g., high refractive index, visible-to-infrared transparency window, high rare-earth solubility), which are promising for a wide range of applications. This thesis presents a mechanistic study on the relationship between glass-structure and properties of TeO_2-based glasses with the aim of (i) enhancing visible transparency of TeO_2-ZnO-Na_2O (TZN) glass film and (ii) understanding ionic conductivity of TeO_2-Na_2O-NaX (TNN) glass system with X=Cl, Br, I.

The first focus of this thesis is driven by the notorious issue that metallic-Te formed in TZN *sol-gel* films deteriorates the transparency. Previous research has revealed that metallic-Te is formed due to the chemical reduction of Te^{4+} to Te^0 during the synthesis process. Applying O_2 rich atmosphere during the thermal treatment (for converting organic *sol* to inorganic TZN glass) can suppress the formation of metallic-Te. However, the complete prevention of metallic-Te formation has not been achieved to date. In this thesis, the research on non-hydrolytic *sol-gel* (*NHSG*) process of making TZN transparent glass film elucidates the mechanism of metallic-Te formation, which reveals the use of O_2 combined with a longer *sol* aging time (30~60 days) and an optimized *sol* heating temperature (150 °C) can completely prevent the formation of metallic-Te. The TZN glass film prepared via this optimized protocol has a transmission close to the theoretical limit. The achievement of high-transparent TeO_2-based glass film paves the way to develop hybrid optoelectronic films by incorporating diverse nanoparticles with unique functionalities.

The second part of this thesis focuses on ionic conductive glasses that rely on the migration of mobile alkali (sodium or lithium) ions. The conductivity of such glasses is determined by the concentration and mobility of mobile alkali ions. The research on traditional oxide glasses (SiO_2-, B_2O_3, P_2O_5-based) has revealed that the incorporation of halides enhances the conductivity. This

thesis investigates the impact of halides on the conductivity of the less-explored glass system, which is TNN glasses with varied (type and concentration) NaX. The conductivity depends on the mobility and concentration of the mobile ions. This research reveals the increase of free volume with increasing NaX concentration, which suggests an increase of space for ion migration thus mobile ion mobility. The Raman spectra confirm the expansion of glass network caused by the introduced NaX. The conductivities of NaCl and NaBr containing glasses remain constant while the mobile ion mobility increases with increasing NaCl or NaBr concentration, which infers a decrease of mobile Na^+ ion concentration. The conductivity of NaI containing glasses significantly increases with increasing NaI concentration, which suggests an increase of mobile Na^+ ion concentration in addition to the increase of the mobility. This research achieved the enhancement of conductivity while maintaining a good transparency of TeO_2-based glasses. In addition, the mechanistic understanding of the relationship of halides, glass-structure and conductivity is a valuable guidance to the future research on ionic conductive glasses.

Declaration

I certify that this work contains no material which has been accepted for the award of any other degree or diploma in my name, in any university or other tertiary institution and, to the best of my knowledge and belief, contains no material previously published or written by another person, except where due reference has been made in the text. In addition, I certify that no part of this work will, in the future, be used in a submission in my name, for any other degree or diploma in any university or other tertiary institution without the prior approval of the University of Adelaide and where applicable, any partner institution responsible for the joint-award of this degree. I give permission for the digital version of my thesis to be made available on the web, via the University's digital research repository, the Library Search and also through web search engines, unless permission has been granted by the University to restrict access for a period of time.

I acknowledge the support I have received for my research through the provision of an Australian Government Research Training Program Scholarship.

Signed:

Date: 25/01/2022

Table of Contents

List of Figures

List of Tables

Acknowledgements

As a survey reported by *nature* in 2019 suggests, nearly 29% of PhD candidatures are suffering from anxiety or depression. Fortunately, I am not one of those 29%, since in these 4 years, I was accompanied by many people, who offered me helps, supports and kind concerns. Without them, I would never make this journey till the end. I would like to sincerely give my acknowledgements to everyone who have contributed to my PhD and my apology to those are not listed below, all your efforts are appreciated.

Firstly, I would like to gratefully acknowledge my supervisors, Heike Ebendorff-Heidepriem, Tim (Jiangbo) Zhao and Bruno Poletto Rodrigues, for professionally and mentally guiding me on the right direction of academic research. Heike's knowledge on material sciences, specially on glasses, makes her a fantastic principal supervisor and great leader during my PhD. Tim plays an irreplaceable role on the TZN *sol-gel* part for his skills on problem solving and insight to the nature of phenomena, his knowledge on physics also makes a significant contribution to the TNN conductive glass part. Bruno has a powerful skill on correlating the experimental data to a theoretical physics model, which is inspiring and has progressed the conductive TNN part to a level that I could never achieve alone. More importantly, their enthusiasm on scientific research makes me aware of how to be an excellent researcher. Extra thanks to Heike and Tim for helping me with my PhD scholarship application. I would like to thank Tara Pukala, my postgraduate coordinator, for helping me with signing a lot of "annoying" documents.

I would like to acknowledge the Australian National Fabrication Facility (ANFF) OptoFab node for offering the tools for glass fabrication and characterisation. Special thanks must give to Alson Kwun Leung Ng of ANFF, who has helped me with all the equipment training and materials ordering, more importantly, for his patient on the mistakes I made. I would like to acknowledge the Adelaide Microscopy for the helps on sample characterisation, specifically, thanks to Ken Neubauer for his help on SEM and to Benjamin Wade for his help on EPMA. I would like to acknowledge my colleagues of Fibres and Photonics Materials group at the Institute for Photonics and Advanced Sensing (IPAS) for their helping on discussion with regard to me research.

I would like to acknowledge my collaborators, Andrew Abell (The University of Adelaide), Gujie Qian (Flinders University), Xiaozhou Zhang and Yinlan Ruan for their helps on the research of

Dedication

Journal / conference publication:

Riesen, N., Pan, X., Badek, K., Ruan, Y., Monro, T.M., Zhao, J., Ebendorff-Heidepriem, H. and Riesen, H., 2018. Towards rewritable multilevel optical data storage in single nanocrystals. Optics Express, 26(9), pp.12266-12276.

Riesen, N., Pan, X., Badek, K., Ruan, Y., Monro, T., Zhao, J., Ebendorff-Heidepriem, H. and Riesen, H., 2018, September. Rewritable multilevel optical data storage in BaFCl nanocrystals. In Optical Data Storage 2018: Industrial Optical Devices and Systems (Vol. 10757, p. 1075704). International Society for Optics and Photonics. (Conference paper)

Pan, X., Zhao, J., Qian, G., Zhang, X., Ruan, Y., Abell, A. and Ebendorff-Heidepriem, H., 2020. Mechanistic insight into the non-hydrolytic sol–gel process of tellurite glass films to attain a high transmission. RSC Advances, 10(4), pp.2404-2415.

Conference abstracts:

Pan, X., Zhao, J., Qian, G., Zhang, X., Ruan, Y., Bachus, K., and Ebendorff-Heidepriem, H., Preparation of high transparent tellurite-based glass coating for high index application by sol-gel method, *21st International Symposium on Non-Oxide and New Optical Glasses, Jun 2018*. (Accepted as oral presentation)

Pan, X., Zhao, J., Qian, G., Zhang, X., Ruan, Y., Bachus, K., and Ebendorff-Heidepriem, H., Fabrication of highly transparent high-refractive index tellurite-based glass film by non-hydrolysis sol-gel method, *International Conference of Young Researchers on Advanced Materials, Nov 2018*. (Accepted as poster presentation)

Pan, X., Zhao, J., Qian, G., Zhang, X., Ruan, Y., Bachus, K., and Ebendorff-Heidepriem, H., High-transparent, high-refractive index tellurite glass film via an optimal non-hydrolysis sol-gel synthesis route, *the 9th International Otto Schott Colloqium, to be held in conjunction with the 4th International Symposium on Glass and Entropy, Oct 2019*. (Accepted as poster presentation)

Abbreviations

BO	**B**ridging **O**xygen
BSED	**B**ack-**S**cattered **E**lectron **D**etector
CN	**C**oordination **N**umber
CPE	**C**onstant **P**hase **E**lement
DC	**D**irect-**C**urrent
EPMA	**E**lectron **P**robe **M**icro-**A**nalyzer
ETD	**E**verhart-**T**hornley **D**etector
FTIR	**F**ourier **T**ransform **I**nfrared **S**pectroscopy
HSG	**H**ydrolytic *Sol-Gel*
IS	**I**mpedance **S**pectroscopy
LPE	**L**one **P**air of **E**lectrons
MNI	**M**obile **Na$^+$ i**on
NBO	**N**on-**B**ridging **O**xygen
NHSG	**N**on-**H**ydrolytic *Sol-Gel*
OG	**O**rganic **G**roup
PTSA	**P**-**T**oluene **S**ulfonic **A**cid
SCM	**S**canning **C**onfocal **M**icroscope
SEM	**S**canning **E**lectron **M**icroscope
STA	**S**imultaneous **T**hermal **A**nalysis
TG-DSC	**T**hermo-**G**ravimetric and **D**ifferential **S**canning **C**alorimetry
TLL	**T**eO$_2$-**Li**$_2$**O**-**Li**X (X=Cl, Br)
TNN	**T**eO$_2$-**Na**$_2$**O**-**Na**X (X=Cl, Br, I)
TZN	**T**eO$_2$-**Z**nO-**Na**$_2$O
UV-Vis	**U**ltraviolet-**vis**ible
XRD	**X**-**R**ay **D**iffraction
For sol-aging only	
F	**F**resh
L	**L**ong
M	**M**edium

S   **S**hort

Chapter 1 - Introduction

1. 1 Introduction of TeO$_2$-based glass materials

Since the first report of TeO$_2$-based glass published in 1952 [1], this glass system has attracted a growing interest in these 70 years. Compared to the other oxide glass systems, TeO$_2$-based glass system has a unique combination of properties, such as visible-infrared range transmission, high refractive index, low melting temperature, high rare earth solubility, and special glass-structure, etc. Such outstanding advantage has sparked the research of TeO$_2$-based glass progressing in material science, including compositions, synthesis methods, glass-structure, properties, and applications [2-4].

The components in a glass system can be classified as glass formers, glass modifiers and glass intermediates [5, 6]. In the TeO$_2$-based glass system, TeO$_2$ plays the role as glass network formers, which it forms the interconnected network of the glass system [2]. Glass modifiers (e.g. Na$_2$O, K$_2$O) are added to the TeO$_2$-based glass system as a second component, which interrupt the continuous glass network and create non-bridging oxygens (NBO), consequentially altering the properties of the glass, e.g., lowering the melting temperature range and viscosity [7]. ZnO and Al$_2$O$_3$ are typically added to TeO$_2$-based glasses as network intermediates, which act as network formers or network modifiers depending on the glass composition [8].

TeO$_2$-based glasses are synthesised via a range of methods. One prevalent method of synthesizing TeO$_2$-based glasses is the melt-quench method [1], where the batched raw materials are melted at elevated temperature, followed by rapidly quenching (e.g. casting in a brass mould) the melt to achieve amorphous status. In light of thin film configuration, *sol-gel* method [9-11] and sputtering deposition method [12] are often used, permitting controllable thickness (from sub-mm to mm scale).

The glass-structure describes the arrangement of atoms in a glass system, extensive research have been performed to study the structure of TeO_2-based glasses [13-16]. In this thesis, the TeO_2-based glass structure is inclusive of (i) the structure and connection of polyhedra which form the glass-network, (ii) the connection or existence of ion offered by glass modifier, (iii) the redox states of tellurium.
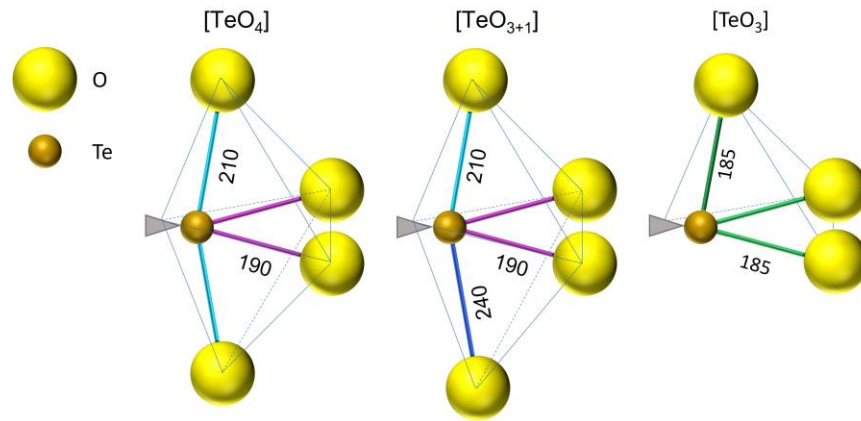
Figure 1-1 Schematic diagram of [TeO_4], [TeO_{3+1}] and [TeO_3] polyhedra [2]. The bond lengths are in pm unit.

(i) TeO_2-based glasses are composed of corner-sharing [TeO_4], [TeO_{3+1}] and [TeO_3] polyhedra. Tellurium element has six valence electrons (ground state electron configuration: $[Kr]4d^{10}5s^25p^4$), which are four p-electrons and two s-electrons. Four p-electrons are hybridized with the valence electrons of O element to form a polyhedra, resulting in Te^{4+} and O^{2-}, leaving s-electrons existing as lone pair of electrons (LPE) [2, 17]. The LPE occupies an equatorial site and repulses the Te-O bonds at both axial and equatorial directions, resulting in the asymmetric trigonal bipyramid [TeO_4] or [TeO_{3+1}] (or trigonal pyramid for [TeO_3] polyhedron) structure (**Figure 1-1**) [18]. In these polyhedra, the axial Te-O bond is longer than the equatorial Te-O bond. The interaction of the LPE with an oxygen of an adjacent polyhedron forms a weak inter-polyhedral Te···O bond.

(ii) The mobile ions in a TeO_2-based glass system arise from the glass modifiers (e.g., Na_2O or Li_2O). The concept of mobile ion will be introduced later in section 3. 1. 1.

(iii) In this thesis, the redox states of the poly-valent tellurium are considered as the glass-structure. Ideally, the tellurium in TeO_2-based glass exists as Te^{4+}, however, the Te^{4+} can be reduced to Te^0 and form metallic-Te, which is usually undesired for optical applications since metallic-Te causes coloration and scattering.

TeO_2-based glasses possess a range of unique properties compared to the other oxide glass systems (e.g., silicate glasses, boron oxide glasses and phosphate glasses), such as:

1) high rare-earth solubility [19].

2) a transmission window of 0.3 μm to about 6.5 μm through millimetre scale thickness (0.6 ~ 4 μm in metre scale) [2, 20], whereas for silicate glasses the transmission window is limited from 0.2 μm to 3 μm [19].

3) high refractive index for the optical frequency concerned (about 2.0).

4) high third-order non-linear optical susceptibilities [2].

5) TeO_2-based glasses have relatively higher dielectric constants at microwave range (i.e. about 13 to 35) compared to other oxide glasses (e.g. about 4 for silicate glasses).

6) TeO_2-based glasses are one of the oxide glass systems with the lowest phonon energy.

7) TeO2-based glasses are classified as soft glass for their relatively lower preparation temperature (e.g. about 900 °C for TZN glass), hence promising to text concepts for advanced materials (e.g., embedding upconversion particles) [21].

TeO_2-based glasses are promising materials for a wide-range of applications, such as optical waveguide laser and amplifier [22], supercontinuum generation [23], sensors [24, 25], etc [20], due to the

flexibility in compositions, diversity in shapes and preparation methods, and the unique combination of properties (e.g. high refractive index combined with wide transmission window).

1. 2 Thesis outline

1. 2. 1 Motivation and novelty

This thesis has advanced the science of TeO_2-based glass in two aspects, i) achieving high transparency for the TeO_2-ZnO-Na_2O (TZN) glass film (chapter 2); ii) gaining in-depth knowledge the in-depth knowledge of the impact of halides on the structure and properties (e.g., ionic conductivity) of TeO_2-Na_2O-NaX (TNN, X=Cl, Br, I) glasses (chapter 3).

Hybrid TZN glass films with embedded luminescent nanoparticles are promising for optical applications. The refractive index of TZN glass films is ~2.0, which is close to the refractive indices of luminescent particles (> 2.0) [26-29]. The reduced index contrast suppresses the scattering and enhances excitation efficiency. However, the application of TZN glass film as high refractive index coating is hindered by the low transparency (colouration) caused by metallic-Te. To overcome this challenge, the dependence of glass-structure (redox state of tellurium) and transparency on synthetic conditions (heating temperature, heating time and atmosphere) was investigated (*Figure 1-2*), via elaboration of the mechanism of metallic-Te formation at different steps of *sol-gel* process. As a result, the optimal protocols of synthesizing highly transparent TZN glass film are proposed and examined.
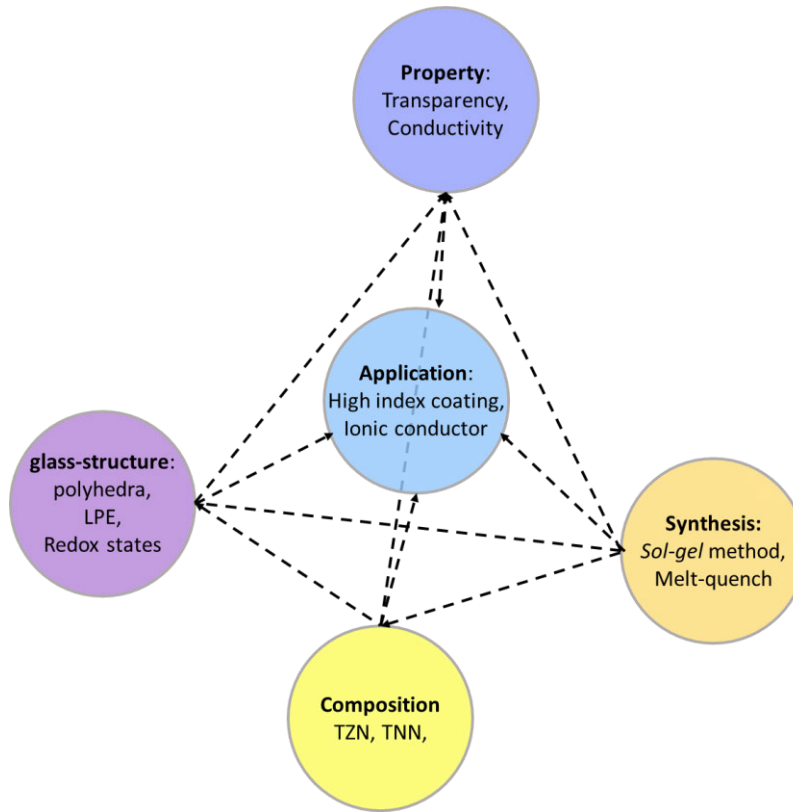
Figure 1-2 The correlation between compositions, synthesis, glass structure, properties and applications for the research of TeO_2-based glasses presented in this thesis.

As mentioned in section 1. 1, the TeO_2-based glasses have been explored for optical waveguide laser and amplifier applications [30-33], but less efforts have been made to evaluate the potential of TeO_2-based glasses as transparent conductive material. Although transparent electronic conductive coatings (usually in the nanoscale thickness) have been developed [34-37], it is rare to achieve transparency in the visible range for electronic conductive materials with millimetre thickness, due to the competition of the underlying physics of electronic conduction and transparency (details in supplementary B1. 2). This leaves an excellent opportunity for ionic conductive materials. The ionic conduction of traditional glasses (SiO_2-, B_2O_3-, P_2O_5-based) has been extensively studied (supplementary B1. 1) [38], revealing that adding halides is one effective route to enhance their conductivities (section 3. 1. 2). Following the principle of material science research (**Figure 1-2**),

this thesis focus onto the impact of halides on the conductivity of TeO_2-Na_2O-NaX glass. This part uncovers the relationship of compositions (NaX concentrations), glass-network and the properties (e.g., conductivity and transparency).

1. 2. 2 Thesis structure

The structure of this thesis is presented by the flowchart in **Figure 1-3**. For the TZN transparent glass film part, the formation of metallic-Te deteriorating transparency is identified as the challenge on preparing TeO_2-based glass film via *sol-gel* method (section 2. 1). The experimental methods (samples preparation) and characterization (including X-ray diffraction analysis, thermal analysis and transmission spectra, etc.) are introduced prior to the discussion of the results (section 2. 3. 1). The results and discussion section commences with transmission and XRD analysis to illustrate the impact of oxide crystals and metallic-Te on transparency (sections 2. 3. 2. 1-2). Subsequently, the chemical reactions and structure evolutions are discussed for understanding the mechanism of metallic-Te formation (sections 2. 3. 2. 3-8). Accordingly, an optimal protocol is proposed to prepare TZN glass thin film with high transparency (section 2. 3. 2. 9). This work has been summarized in a journal publication in 2020 [10].

For the TNN conductive glass part, to justify the selection of the TNN glass system, the research on TeO_2-based ionic conductive glasses is reviewed (section 3.1). In section 3.2, sample preparations and characterization methods (e.g., Raman spectroscopy, density, and X-ray diffraction) are introduced. The results of the characterizations of those samples are presented and discussed in section 3. 3, including the identification of glass forming regions (section 3. 3. 1) and the discussion of the impacts of composition variation on structure evolution and conductivity (section 3. 3. 2-7).

Finally, the implications and prospects on both parts are made in chapter 4.
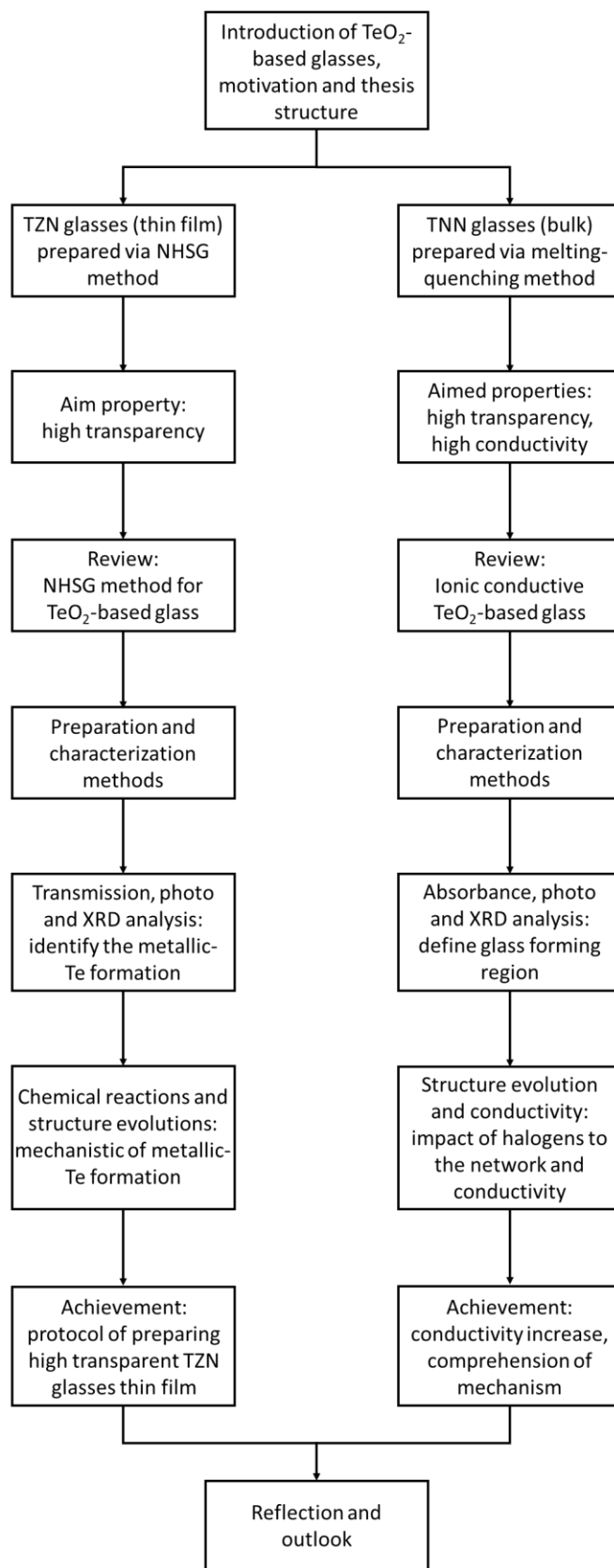
Figure 1-3 A flowchart indicating the structure of this thesis

Chapter 2 - TeO$_2$-based transparent glass film

2. 1 Literature review of TeO$_2$-based glass film prepared via *Sol-Gel* method

Compared to organic films, inorganic TeO$_2$-based glass films have superior chemical resistance and thermal stability. TeO$_2$-based glass films can be prepared using the *sol-gel* method, which can be categorised into *hydrolytic sol-gel* method (*HSG*) and *non-hydrolytic sol-gel* method (*NHSG*). The Te-alkoxide, which is used to prepared TeO$_2$-based glass via *HSG*, reacts rapidly with H$_2$O and results in undesired precipitation of particles, hampering the formation of a continuous film. Equation 2.1 shows an example of Te-alkoxide hydrolysed with H$_2$O.

$$Te(OR)_4 + 2H_2O \rightarrow TeO_2 \downarrow + 4ROH \qquad\qquad 2.1$$

In this reaction, the O of H$_2$O is used as oxygen donor of *NSG*. To avoid the unwanted hydrolysis, the *NHSG* method has been developed. As the name suggests, *NHSG* method is a *sol-gel* chemical route that uses various oxygen donors (e.g. ethers, carboxylates, alcohols, or the metal-alkoxide itself, etc) rather than H$_2$O [39], to evolve the polymerisation for *sol*, *gel* and then film formation. An example of the reaction for *NHSG* is showed in equation 2.2 [40].

$$Te(OR)_4 + (OR)_4Te \rightarrow (OR)_3Te\text{-}O\text{-}Te(OR)_3 + ROR \qquad\qquad 2.2$$
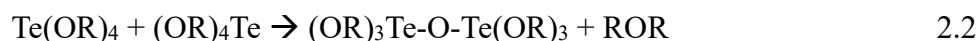
The procedure of synthesizing TeO$_2$ glass thin films using *NHSG* method was reported in-detail by Heng-yong Wei et al. in 2009 [11]. Basically, the *NHSG* process includes 3 steps, (i) preparation of Te-alkoxide Te(O$_2$C$_3$H$_6$)$_2$ precursor solution, (ii) condensation of the precursor *sol* at low temperature (e.g. 80 ^{o}C), and (iii) combustion of residual hydrocarbons at elevated temperature (e.g., 300 ^{o}C). Infrared spectroscopy and ^{1}H-nuclear magnetic resonance characterizations suggest the chemical reactions of transforming the Te-alkoxide to TeO$_2$ network (equation 2.3) as follows [11]:

$$nTe(O_2C_3H_6)_2 \rightarrow nTeO_2 + nC_6H_{12}O_2 \hspace{3cm} 2.3$$
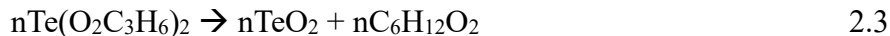
where the $Te(O_2C_3H_6)_2$ acts as the oxygen donor.

Building upon the works of Heng-yong Wei et al., Binbin Zheng et al. reported the preparation of multicomponent TeO_2-ZnO-Na_2O (TZN) film with controllable thickness and superior homogeneity [41]. My Master research followed his *NHSG* protocol to synthesize TZN glass thin films [42]. Most of the parameters presented in this thesis were adopted from Zheng's paper, other than the ramp-up rate (10 ^{o}C/min in my work). A fast ramp-up rate was chosen, which reduced the time that the specimens were exposed to moisture (of open air).
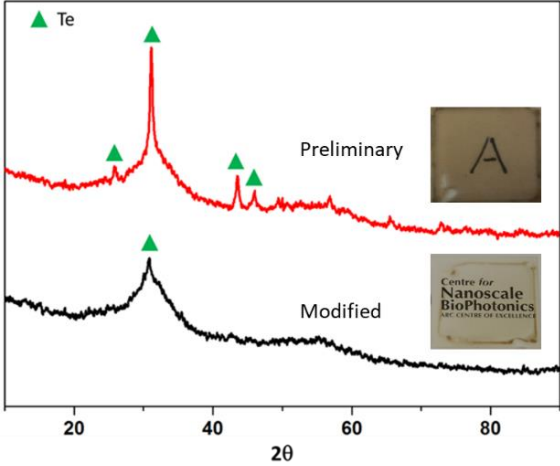
However, this prepared specimen encounters deep brown colour (photo in **Figure S. 2**), which prevents its optical applications. According to the micro-XRD and TG-DSC analysis, the coloration was found to be caused by the formation of metallic-Te [42]. Therefore, suppressing metallic-Te formation is the key to obtain high-transparent TZN glass thin films.

To suppress the formation of metallic-Te, Heng-yong Wei et al. proposed a pre-treatment step of heating the sample at 200 ^{o}C in O_2 rich atmosphere [11]. In addition to adopting this pre-treatment step, I have also investigated the impact of ramp-up rate, dwelling time and cooling rate on the formation of metallic-Te using absorbance spectra. The results indicated that a slow ramp-up rate (i.e. 0.5 ^{o}C/min or 1 ^{o}C/min) and a fast cooling rate (i.e. air quenching) are beneficial to suppress the metallic-Te formation. A modified *NHSG* protocol was developed according to those findings. The film prepared using this modified *NHSG* protocol had a higher transparency and lower concentration of metallic-Te (**Table 2-1**), compared to the preliminary TZN glass thin film prepared following Binbin Zheng et al.'s procedure.

As illustrated by the photo and micro-XRD spectrum (**Table 2-1**), the modified TZN glass thin film still has a light brown colour and a broad metallic-Te XRD peak, which indicates the removal of metallic-Te in the films is not complete yet.

Table 2-1 The comparison of the specimens prepared using reported protocols and the modified protocols (findings of my master project). The micro-XRD spectra are collected from the TZN glass coating on Si wafers, while the attached images indicate the appearance of TZN glass coating on coverslips.

Thermal treatment protocols	Comparison
Adopted protocol: 1) Ramp up from room temperature to 80 $^{\circ}$C with a rate of 10 $^{\circ}$C/min. 2) Dwell at 80 $^{\circ}$C for 12 hours. 3) Ramp up to 300 $^{\circ}$C with a rate of 0.5 $^{\circ}$C/min. 4) Dwell at 300 $^{\circ}$C for 2 hours. 5) Cool down in furnace.	
Modified protocol: 1) Ramp up from room temperature to 130 $^{\circ}$C with a rate of 10 $^{\circ}$C/min. 2) Dwell at 130 $^{\circ}$C furnace for about 12 hours. 3) Transfer to a furnace with O_2 flow and dwell for 2 hours. 4) Turn off the O_2 flow, then ramp up to 300 $^{\circ}$C with a rate of 0.5 $^{\circ}$C/min. 5) Dwell at 300 $^{\circ}$C for 1.5 hours. 6) Quench in air.	

2. 2 Statements

Contribution on conceptualization

The idea of developing TZN glass film was proposed by Jiangbo (Tim) Zhao, and protocols for successful proof-of-concept demonstration were suggested by him during my master period. At the end of my master project, Heike Ebendorff-Heidepriem firstly noticed the colouration was caused by metallic-Te. During my PhD period, I progressed on the understandings of chemistry mechanism related to the metallic-Te formation of TZN sol-gel. The chemical reactions regarding preparation of pure Te-alkoxide and polymerization reactions were mainly developed by Xuanzhao Pan and Jiangbo (Tim) Zhao. The idea of structural model was firstly raised by Heike Ebendorff-Heidepriem, and completed by Xuanzhao Pan, Jiangbo (Tim) Zhao and Heike Ebendorff-Heidepriem. The optimal NHSG protocol was proposed based on the understanding of chemistry mechanism (by Xuanzhao Pan, Jiangbo (Tim) Zhao, and Heike Ebendorff-Heidepriem).

Contribution on realization

Most of the experiments, data collection and data processing were performed by Xuanzhao Pan under the supervision and guidance by Heike Ebendorff-Heidepriem and Jiangbo (Tim) Zhao, except for the micro-XRD measurements and XRD peaks identification were performed by Gujie Qian.

Contribution on documentation

The TZN *sol-gel* work performed during my PhD period has been published in a journal paper [10]. The sample preparation and characterisation methods, results and discussion, and conclusion parts of this paper are presented in this thesis. Preliminary version of the paper was drafted by Xuanzhao Pan. Jiangbo (Tim) Zhao and Heike Ebendorff-Heidepriem offered significant helps on paper

structuring, content presenting and language polishing, followed by feedback from other co-authors. Other authors have helped with paper revision.

Declaration and permission

I declare that the above statement of contribution is accurate, and I give the permission of this publication to be presented in this thesis. Section 2.3 is directly copied from the paper [10] with minor change, e.g., updating figures numbers and fonts.

2. 3 Mechanistic insight into the *NHSG* process of TZN glass films (adopted from my paper [10])

2. 3. 1 Sample preparation and characterisation methods

2. 3. 1. 1 Synthesis

Reagents: TeO$_2$ powder (TeO$_2$, Suzhou Sinosun, 99.999%), Zn-acetate di-hydrate crystals (Zn(CH$_3$COO)$_2$·2H$_2$O, Sigma Aldrich, 99.0%), Na-acetate crystals (CH$_3$COONa, Sigma Aldrich, 99.0%), 1,2-propanediol solvent (Sigma Aldrich, 99.5%), and p-toluene sulfonic acid monohydrate crystals (PTSA, Sigma Aldrich, 98.5%) were used as received without purification or pre-treatment.

Preparation of Te-alkoxide (Te(O$_2$C$_3$H$_6$)$_2$): In brief, TeO$_2$ powder and PTSA crystals (as catalyst) were added into 1,2-propanediol in a 100-ml round bottom flask, with a molar ratio of 0.1:0.01:1. By heating the mixture at 150 °C under refluxing with moderate stirring (~1000 rpm) for about 6 h, a considerable number of Te-alkoxide crystals were obtained with by-products. To extract high-purity Te-alkoxide crystals, the resulting mixture was processed *via* suction filtration. To enhance

the extraction rate of Te-alkoxide crystals, we collected this filtration when the mixture was hot. Te-alkoxide crystals were then precipitated by retaining the filtrate in a refrigerator (at ~2 $^{\circ}$C) for > 3 days, during which particulate-form Te-alkoxide was recrystallized from the saturated solution. Subsequently, high-quality Te-alkoxide crystals were collected by centrifugation and vacuum-drying. This as-prepared Te-alkoxide was used as the precursor for synthesis of TZN *sol-gel* [41].

Preparation of TZN sol: Firstly, Te-alkoxide (1 M), Zn-acetate (1 M) and Na-acetate (1 M) solutions were prepared *via* dissolving the respective crystals in 1,2-propanediol under heating (~60 $^{\circ}$C) and stirring (~1000 rpm) for about 30 mins in a round-bottom flask. These solutions were then mixed, with a molar ratio of Te:Zn:Na = 80:10:20, followed by heating at 80 $^{\circ}$C for 2 h to form TZN *sol*. The *sol* was aged in a desiccator at room temperature for different days as summarized in Table 1. Prior to the film preparation, the TZN *sol* was centrifuged at 14800 rpm for 15 mins to remove any unwanted large particulates. Note refluxing was applied for steps with heating.

Preparation of TZN-based glass film in open air: The aged TZN *sol* was deposited onto a substrate by spin coating, e.g., 2000 rpm for 60 seconds with an acceleration of 100 rpm/s. The coated substrates were subsequently heated (ramp up rate 5 $^{\circ}$C/min) for 12-72 h at varying temperatures (72 h at 80 $^{\circ}$C, 12 h at130 $^{\circ}$C, and 12h at 150 $^{\circ}$C) to acquire TZN *xerogel* films, which were further processed at elevated temperatures (300 $^{\circ}$C, 400 $^{\circ}$C and 500 $^{\circ}$C) with a heat up rate of 1 $^{\circ}$C/min and dwell time of 1 h. With regard to the substrate used for film preparation, pre-cleaned Si wafers and glass coverslips were selected for μ-XRD analysis and optical characterizations, respectively.

Preparation of TZN-based xerogel powder in open air: The same aged TZN *sols* used for glass film production were placed in opened vials and heated for 12-72 h at different temperature (72 h

at 80 °C, and 12 h at 130 °C, 150 °C or 160 °C). The collected TZN *xerogel* powders were used

for colour inspection and TG-DSC measurement.
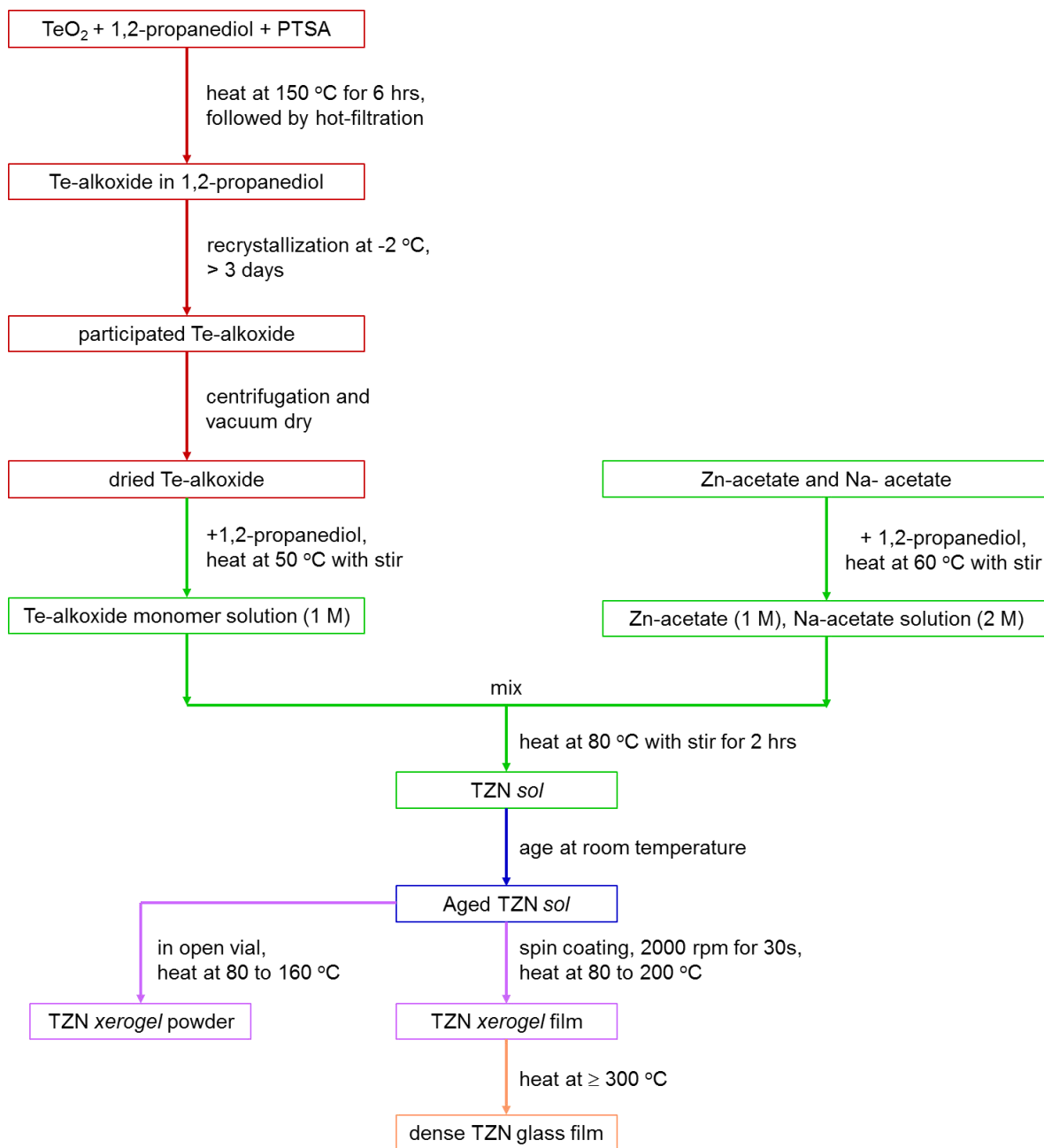
Figure 2-1 The flow chart shows the synthetic processes in detail, where different colours represent the

five steps in the whole process: Te-alkoxide (red), TZN *sol* (green), aged TZN *sol* (purple), TZN *xerogel*

(pink) and dense TZN glass film (orange).

Preparation of TZN-based glass film in O₂-rich atmosphere: A tube furnace with a glass liner was used to prepare dense TZN glass films in dry O_2 atmosphere. The film samples were placed in the glass liner at room temperature. Then one end of the liner was connected to the dry O_2 supply, and the other end was connected via a glass valve to a vacuum pump (**Figure 2-2 a**). To remove the air and fill the liner with dry O_2, 4 cycles of vacuuming and O_2 purging were used. After that, the glass valve was disconnected from the vacuum pump and connected to a pipe where part of it was inserted in a flask filled with silicone oil (**Figure 2-2 b**) to be able to monitor the constant O_2 flow through the glass liner and to prevent backflow of air. The O_2 flow was initially purged at 5 L/min for 30 min to quickly enrich O_2 in the chamber, followed by tuning down to ~0.1 L/min prior to heating up to undertake the *sol*-heating and *xerogel*-heating steps. Such reduced O_2 flow rate is sufficient to replenish and maintain the high O_2 partial pressure, but also to avoid the formation of large temperature gradient across the film sample within the hot zone of the furnace. Under continuous provision of O_2, the placed film samples were then heated as follow: (1) from room temperature to 80/150 °C with a rate of 5 °C/min and dwelled for 12 h; (2) heating to 300 °C with a rate of 1 °C/min and dwelled for 1 h.
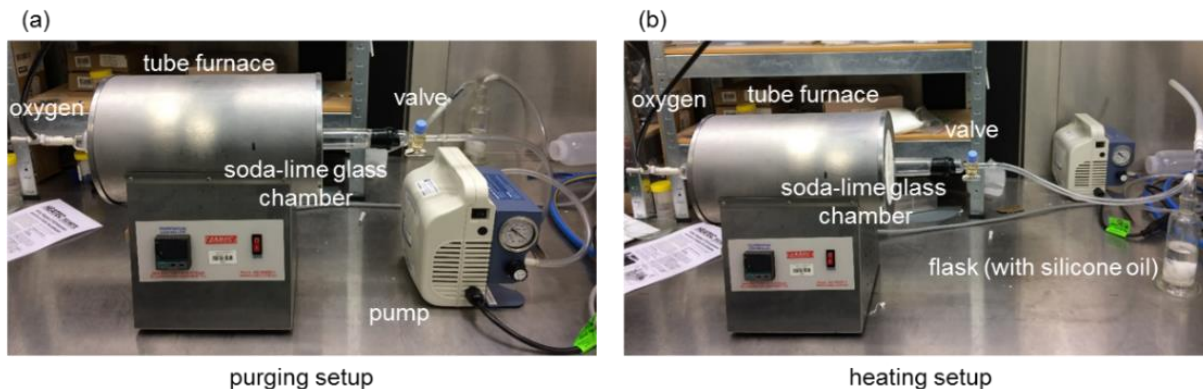
Figure 2-2 The heating system used for preparing TZN-based glass films in O_2-rich atmosphere. (a) 4 cycles of vacuuming and O_2 purging to enrich O_2 in the chamber; (b) *sol* heating and *xerogel* heating processes under O_2 flow at ~0.1 L/min which is exhausted via a pipe in a silicone-oil filled flask.

2. 3. 1. 2 Thermal analysis

Thermogravimetric and differential scanning calorimetry (TG-DSC) analysis of TZN *xerogel* powders was performed over the range of 30 to 700 °C by a thermal analysis system (TG-DSC 2 STARe, Mettler Toledo). The TG-DSC curves were acquired with a ramping rate of 10 °C/min under specific atmosphere, i.e. 20% O_2 + 80% N_2 and 80% O_2 + 20% N_2 with flow rate of 3 L/min, respectively. All powder samples were placed in alumina crucibles for TG-DSC analysis. The first derivative of TG data was calculated for differentiate-TG (DTG) curve, which allows to visualize the rate of weight change across the temperature range under consideration.

Simultaneous thermal analysis (STA) was run to monitor the discharged gaseous molecules during heating TZN *xerogels* from 30 to 350 °C, by using hyphenated Fourier transform infrared spectroscopy (vapor-FTIR) (Spectrum 400, Perkin Elmer). The spectra were recorded in the wavenumber range of 500-4000 cm^{-1}, with a resolution of 2 cm^{-1}. The sample chamber was heated at the ramping rate of 5 °C/min and purged with dry air (1.8 L/min).

16

2. 3. 1. 3 X-ray diffraction

The micro-XRD analysis of the TZN-based films on Si wafers was conducted using a micro-diffractometer (D/MAX-Rapid II Microdiffractometer, Rigaku) with a Cobalt Kα radiation (wavelength 1.7902 Å, accelerating voltage 40 kV, and filament current 15 mA) at a fixed incident angle of 10°. A 0.1 mm collimator, equivalent to an X-ray beam size of approximately 150×150 μm, was used for the analysis. Exposure time (on the imaging plate) for each analysis was set to be 10 min. The computer software 2DP was used to convert original 2D imaging data (Debye-Scherrer rings) collected from the curved imaging plate to 1D profiles (i.e. diffraction intensities vs. 2θ), during which, the Si diffraction is eliminated. The powder-XRD analysis of TZN-based powder samples was completed by Rigaku miniflex600 with a copper Kα radiation (wavelength 1.5418 Å, accelerating voltage 40 kV, and filament current 15 mA). The default widths of incident and receiving Soller slits were set to be 2.5°, and the size of divergence slit was selected to be 1.25 °. The widths of scattering slit and receiving slit were all 13 mm. The scanning speed was set at 3° per minute, with a stepping size of 0.02°. The crystalline phases were indexed according to the Rigaku PDXL XRD analysis software and ICDD PDF-2 database.

2. 3. 1. 4 Ultraviolet-visible spectroscopy

The transmission measurements of TZN glass films on coverslips from 300 nm to 800 nm were performed by using a UV-Vis spectrophotometer (Cary 5000, Agilent Technologies), with a scanning speed of 600 nm/min and a step interval of 1 nm. The diameter of the aperture allowing light pass though the samples is 5 mm.

2. 3. 1. 5 Mass spectrometry

The molecular weight of Te-alkoxide was identified using mass spectrometry (Bruker, HCT ultra, Germany). Te-alkoxide was dissolved in methanol with a concentration of 0.05 mg/mL, and the resulting solution was subjected to Bruker Daltonik ion-trop MS with a flow rate of 0.1 mL/min. A full scan of the mass ranges from 220 to 1800 g/mol was acquired by using high capacity spherical traps (HCT) for ionization (by electrospray) of the sample.

2. 3. 1. 6 Scanning confocal microscope

An in-house built scanning confocal microscope was used to investigate the optical properties of films, by acquiring the fluorescence intensities distribution of the film in a 2D profile and recording the fluorescent spectra of an arbitrary spot of the film, respectively. The collimated laser beam 532 nm (Crystal Laser, LC-532-100 LO) with a power of 2.56 µW was guided through a 100× magnification objective (Nikon TU Plan Apo, CF 160-2, NA=0.9) and focused onto the film samples. By moving a scanning stage (Piezo XYZ with E-545 PInano$^@$ Piezo controller) with a stepping resolution of 0.3 µm/step, an area of 200 µm × 200 µm was scanned. The fluorescence from film samples was collected by a 2×2 multimode bifurcated fiber (Thorlabs FCMH2-FC), by passing through a 532 nm dichroic beam-splitter (BrightLine$^@$, Di03-R532-t1-25x36) and a 532 nm long-pass filter (RazorEdge$^@$, LP03-532RU-25). These signals were split equally and separately delivered to a photon detector (SPCM, Excelitas Technologies) for imaging acquisition and a spectrometer (iHR320, HORIBA Scienctific) for spectral analysis. The photon counts acquired by photon detector were converted to obtain a 200 µm × 200 µm scanned fluorescence

image. The selected spots from the scanned images were pinpointed for fluorescence spectral measurement, recorded by the spectrometer with an exposure time of 30 s.

2. 3. 2 Results and discussions

2. 3. 2. 1 Steps of chemical reaction for preparing TZN glass films along with sample coding

The *NHSG*-based TZN glass films were prepared via a five-step procedure (**Figure 2-3**, and experimental details in supporting information and **Figure 2-1**), comprising molecular Te-alkoxide preparation, TZN *sol* preparation, *sol* aging to enhance polymerization, *sol* heating to obtain dry porous *xerogel*, and finally *xerogel* heating to form inorganic glass film.

The first step was the preparation of high purity Te-alkoxide ($Te(O_2C_3H_6)_2$) via an alcoholization reaction between TeO_2 powder and 1,2-propanediol solvent [43-45], catalysed with p-toluene sulfonic acid (PTSA). This reaction takes place when anhydrous α-TeO_2 and PTSA monohydrate are dispersed and dissolved in 1,2-propanediol at 150 ^{o}C (with reflux). Details of the chemical reactions are described in Section 2. 3. 2. 3.

The second step was to prepare the TZN *sol*, which is the precursor for the subsequent *NHSG* process. TZN *sol* is formed by heating the mixture of Te-alkoxide molecules, Na-acetate and Zn-acetate in 1,2 propanediol at 80 ^{o}C (with reflux), followed by a high-speed centrifugation (14800 rpm for 15 min) to remove any impurities. Te-alkoxide, Zn-acetate and Na-acetate are added in molar ratio of Te:Zn:Na = 80:10:20.

In the third step, aging the *sol* at room temperature over weeks or months in a closed glass vial was conducted to prepare the so-called aged TZN *sol*. This relates to the fact that the polymerization of the TZN *sol* occurs at room temperature to a different extent, dependent on the

aging duration (details described in Section 2. 3. 2. 4). The *sol*-aging times of 9 days (F), 60 days (S), 90 days (M) and 300 days (L) were applied, where F, S, M and L denote fresh-aged, short-aged, medium-aged and long-aged *sol*, respectively.

In the fourth step, heating aged *sol* at temperatures between 80-150 °C for 12-72 h obtains the dry porous *xerogel* via simultaneously evaporating the solvent and facilitating the polymerization. Two different forms of *xerogel* samples, dry *xerogel* powders and dry *xerogel* films, were prepared in this work.

In the final step, the compact, pore-free, inorganic TZN glass films with the nominal molar composition of $80TeO_2\text{-}10ZnO\text{-}10Na_2O$ were acquired by heating the *xerogel* films at the temperatures of ≥300 °C for 1 h. The temperature was reached using a rate of 1 °C/min from room temperature.
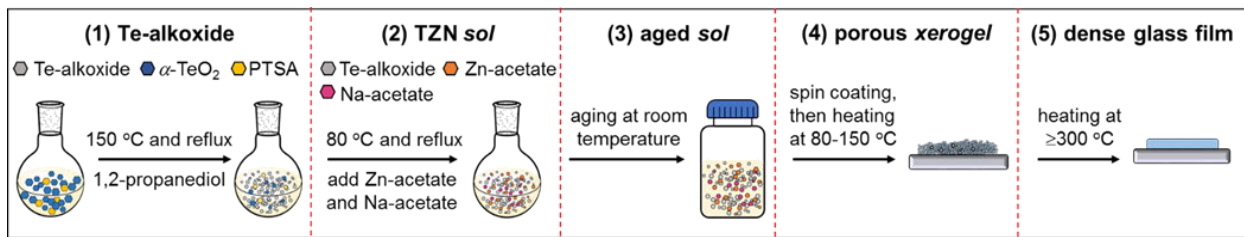
Figure 2-3 Schematic illustration of the five-step procedure to prepare dense TZN glass films. (1) Te-alkoxide synthesized via a catalytic cycle reaction at 150 °C under reflux with starting materials of TeO_2, p-toluene sulfonic acid monohydrate crystals (PTSA) and 1,2-propanediol. (2) TZN *sol* prepared via mixing Te-alkoxide, Na-acetate and Zn-acetate in 1,2-propanediol at 80 °C under reflux. (3) Aged *sol* prepared via storing the *sol* at room temperature in a sealed flask for 9-300 days. (4) Porous *xerogel* film made by heating the wet *sol* film (made via spin coating) at 80-150 °C for 12-72 h. (5) Dense glass film prepared by heating the porous *xerogel* films at ≥300 °C.

Table 2-2 lists the *xerogel* powders used for thermal analysis and the *xerogel*/glass film samples used for optical transmission measurements, X-ray diffraction (XRD) and scanning confocal microscope (SCM) analysis. Transparent glass coverslips were used as film substrates for the optical transmission measurements, while Si wafers were used as substrates for XRD and SCM measurements.

Table 2-2 Summary of the *xerogel* powders and *xerogel*/glass film samples prepared via various conditions, including *sol*-aging time, *sol*-heating temperature, and *xerogel* heating temperature. The *sol*-aging time is classified into 4 categories: "fresh (F)" 9 days, "short (S)" 30-60 days, "medium (M)" 90 days and "long (L)" 300 days.

Samples	Sample code	*Sol* aging (days)	*Sol* heating (ºC-days)	*Xerogel* heating (ºC)
xerogel powder	F-80	9	80-3	
	F-150	9	150-1	
	S-130	60	130-1	
	M-80	90	80-3	
	L-80	300	80-3	
xerogel/glass film	S-130	30	130-0.5	
	S-130-200	30	130-0.5 and 200-0.5	
	S-130-300	30	130-0.5	300
	S-130-400	30	130-0.5	400
	S-130-500	30	130-0.5	500
	S- 80-300	60	80-0.5	300
	S-150-300	60	80-0.5	300

2. 3. 2. 2 Identification of metallic-Te and tellurite crystal formation

We commenced with using the previously reported processing conditions [11, 41]; the S-130-300 TZN glass film was produced via spin-coating short-aged *sol* on a glass coverslip, followed by heating (in air) at 130 °C for 12 h to form a dry *xerogel* film and then heating at 300 °C for 1 h to obtain a

dense glass film. This glass film shows relatively good transmission but a brown colour appearance (**Figure 2-4 a**). Based upon previous observations for other tellurite-based glass films [46] and bulk tellurite glass [47], this colour appearance is attributed to the presence of reduced tellurium species or metallic-Te [11, 46, 48].
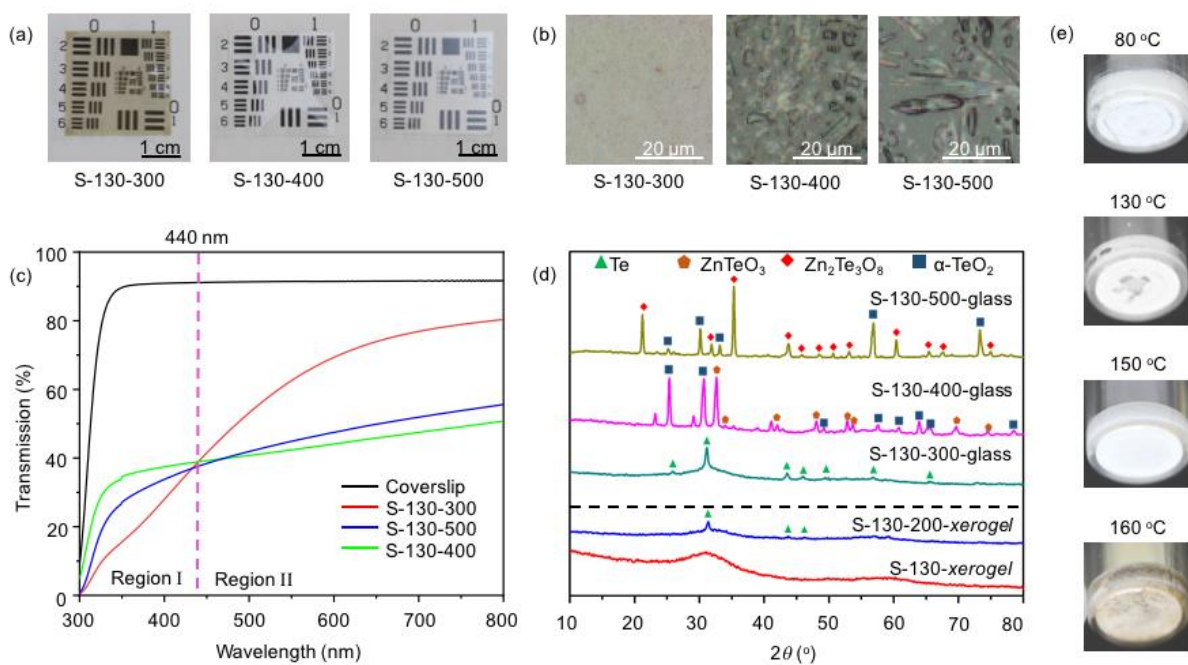
Figure 2-4 Characterizations of TZN films and *xerogel* powders. (a) Photographs, (b) Optical microscope images, and (c) Transmission spectra of TZN glass films on glass coverslips. (d) Micro-XRD patterns of TZN films on Si wafers, where the narrow diffractions indicate the presence of crystal phases, while the broad 'hump' at ~32º reflects the amorphous characteristic. (e) Photographs of *xerogel* powders made by heating short-aged *sol* at 80, 130, 150 and 160 ºC.

In order to eliminate the undesired colour via oxidization of the metallic-Te in the film, higher *xerogel* heating temperatures of 400 ºC and 500 ºC were applied. The increased *xerogel* heating temperatures successfully eliminated the brown colour but led to white and opaque appearance (**Figure 2-4 a**). These visual characteristics are reflected in the transmission spectra (**Figure 2-4**

c). Relative to the spectrum of an uncoated glass coverslip, the S-130-300 glass film exhibits a lower transmission over the measured wavelength range of 300-800 nm. The low transmission particularly in the UV-blue spectral range is associated with the presence of metallic-Te [46]. The low transmission at 800 nm suggests that the metallic-Te exhibits scattering that extends into the infrared region. In contrast to the S-130-300 glass film, the transmission spectra of the S-130-400 and S-130-500 glass films show higher UV-blue transmission, but lower transmission at longer wavelengths >440 nm, which is consistent with their opaque white appearance.

In agreement with the transmission measurements, micro-XRD analysis indicates the diffraction peaks of metallic-Te for the S-130-300 film but not for the S130-400 and S-130-500 samples (**Figure 2-4 d**). The optical micrographs (**Figure 2-4 b**) show that the glass films processed at higher temperatures of 400 °C and 500 °C contain micron-sized crystals with different morphologies (mainly platelets at 400 °C and mainly needles at 500 °C), suggesting the formation of different crystal phases at 400 °C and 500 °C, respectively. This was confirmed by micro-XRD, showing the diffraction peaks of $ZnTeO_3$ crystals for S-130-400 and those of $Zn_2Te_3O_8$ crystals for S-130-500 films. In addition, α-TeO_2 diffractions were found in both films [11, 49]. The optical microscopy and XRD results are consistent with the opaque white appearance and overall reduced transmission of the S-130-400 and S-130-500 films.

To determine the temperature threshold of forming metallic-Te, XRD was used to analyse the *xerogel* films S-130 and S-130-200 (**Figure 2-4 d**). It shows that the S-130 film only exhibits a broad diffraction 'hump', corresponding to an amorphous structure, whereas the S-130-200 film gives the characteristic diffraction peaks of metallic-Te. To determine more precisely the onset temperature of generating metallic-Te, *xerogel* powders were prepared by heating short-aged *sol* using different temperatures of 80, 130, 150, 160 °C. These *xerogel* powders show that only the

160 ºC-processed powder displays the brown appearance of metallic-Te (**Figure 2-4 e**), suggesting formation of metallic-Te commences around 160 ºC. This is consistent with the observation in producing S-130-200 film, where heating of the S-130 *xerogel* film at 200 ºC led to the metallic-Te.

The characterization results of the TZN film and powder samples reveal that metallic-Te is formed when heating *sol* or *xerogel* samples at temperatures >150 ºC but <350 ºC. The amount of metallic-Te is increased for higher *xerogel* heating temperature of 300 ºC compared to 200 ºC. Further increase of *xerogel* heating temperatures to 400 ºC and 500 ºC induces oxidation of metallic-Te (formed at lower temperatures) into crystalline TeO_2 and other crystallinity in TZN glass [49]. These results suggest the only pathway of obtaining a high-transparency colourless TZN glass film lies in preventing the formation of metallic-Te prior to or during heating the *xerogels* into a dense glass. For this purpose, the chemistry with respect to metallic-Te formation at different stages during *NHSG* synthesis is investigated in detail in the following sections, with the aim to identify suitable synthesis conditions to achieve metallic-Te free TZN glass films.

2. 3. 2. 3 Chemical reactions during preparation of Te-alkoxide pre-cursor

As shown in **Figure 2-5 a** (black arrows), the catalysed alcoholization reactions of producing Te-alkoxide molecules begins when the hydrogen atom (H) of the sulfonic acid group of PTSA is displaced by Te in TeO_2 at 150 ºC. This forms the intermediate compound p-toluene sulfonic tellurium (PTS-Te) [43-45], followed by the exchange of the H atom of the hydroxyl groups of 1,2-propanediol with the Te atom of the intermediate PTS-Te. The desired Te-alkoxide is obtained and the catalyst PTSA is regenerated to participate in another catalytic cycle [43]. The resultant Te-

alkoxide dissolved in the solution (**Figure 2-5 a**, bottom-middle photo), was separated from the sediment via hot filtration; the latter contains white powder with interspersed black particles (**Figure S. 2**). The generation of Te-alkoxide $Te(O_2C_3H_6)_2$ (green framed in **Figure 2-5 a**) with a molecular weight of 278 g/mol (isotope ^{130}Te) was confirmed by electrospray ionization mass spectrometry measurement.
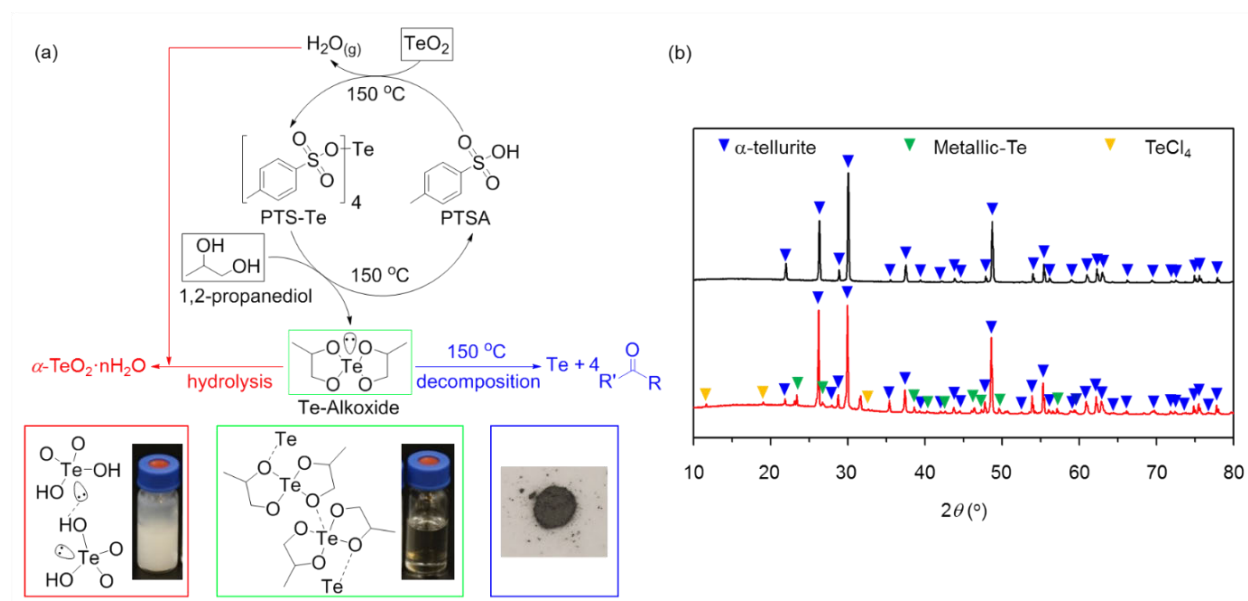
Figure 2-5 Chemical reactions during Te-alkoxide preparation. (a) Catalysed cyclic alcoholization between TeO_2 and 1,2-propanediol generates Te-alkoxide molecules (black arrows). Hydrolysis of Te-alkoxide by in-situ formed H_2O results in the formation of undesired amorphous TeO_2 hydrolytic *gel* (red arrows). Under the thermal activation of 150 °C, Te-alkoxide decomposes to metallic-Te and carbonyl compound (R and R' are organic groups) (blue arrow). The bottom photos from left to right correspond to the TeO_2 hydrolytic *gel* (formed via enhanced hydrolysis by adding H_2O to Te-alkoxide solution), the as-prepared transparent Te-alkoxide solution, and HCl acid-treated sediment. (b) Powder-XRD of the collected sediment before (top graph) and after (bottom graph) HCl treatment.

In the Te-alkoxide molecule, the Te atom is coordinated with the four oxygen atoms of the two branched alkoxy groups, denoted as the intramolecular Te–O bonds. The lone pair of electrons

(LPE) of the Te atom leads to a bipyramidal coordination geometry for Te and a weak intermolecular bond between Te-alkoxide molecules, depicted by a dotted line Te⋯O (**Figure 2-5 a**, bottom-middle molecular structure) [11].

The white powder and the black particles of the sediment indicate undesired formation of TeO_2 precipitate and metallic-Te, respectively, due to the side reactions of hydrolysis and thermal decomposition, which are facilitated by the LPE and bipyramidal coordination of the Te atom as follows.

During the alcoholization forming Te-alkoxide via liberation of H and O from PTSA and TeO_2, H_2O is in-situ produced. The nucleophilic attack of O in H_2O to the bipyramidal coordinated Te in the Te-alkoxide molecule can occur, [50] corresponding to a process known as hydrolysis (**Figure 2-5 a**, red arrows). To illustrate the effect of hydrolysis reaction, a large amount of H_2O (much more than H_2O generated in-situ) was intentionally added to the Te-alkoxide solution, resulting in a white TeO_2 precipitate (**Figure 2-5 a**, bottom-left). This hydrolysis effect agrees with the sediment by-product containing white powder.

As a consequence of the LPE weakening effect, the Te–O bond can be relatively easily broken, particularly under thermal activation. This bond cleavage leads to decomposition of Te-alkoxide molecules into metallic-Te and carbonyl-containing (C=O) compounds (**Figure 2-5 a**, blue arrow). In order to confirm that the black particles in the sediment are metallic-Te, powder-XRD measurement of the collected sediment was used. However, only α-TeO_2 diffractions were detected (**Figure 2-5 b**, top graph). Given that TeO_2 is soluble in HCl solution but not metallic-Te, the sediment was processed by HCl to extract metallic-Te from the large amount of TeO_2. As shown in **Figure 2-5 a** (bottom-right photo) and 3**b**, the diffractions of HCl-treated sediment show the metallic-Te peaks, confirming the source of the black particles in the sediment, which results from

the thermal decomposition. In addition, TeCl$_4$ and α-TeO$_2$ diffractions were observed (**Figure 2-5 b**, bottom graph), which are attributed to the reaction between TeO$_2$ and HCl, and residual TeO$_2$, respectively.

2. 3. 2. 4 Insight into chemical reactions during sol aging, sol heating and xerogel heating

Overview of TG-DSC results

The onset temperature of forming metallic-Te during the preparation of *sol* and *xerogel* was determined to be ~160 °C (**Figure 2-4 e**). Transforming organic-group (OG)-containing *xerogel* into OG-free (inorganic) glass requires heating temperatures ≥ 300 °C, which is markedly higher than the threshold temperature of metallic-Te formation (~160 °C). In order to identify how to avoid metallic-Te formation despite using *xerogel* heating temperature above the onset temperature, we investigated the impact of preparation conditions *sol* aging, *sol* heating and *xerogel* heating on the extent of metallic-Te formation, by using TG-DSC measurements on a series of TZN *xerogel* powders. To this end, F/M/L-80 samples were prepared at low *sol*-heating temperature of 80 °C, using different *sol* aging time (9, 60, 300 days). F-150 sample was prepared at high *sol* heating temperature of 150 °C with 9 days *sol* aging. In addition, S-130 sample was prepared using the same *sol* heating temperature (130 °C) and *sol* aging time (60 days) as for the S-130 *xerogel* film described in Section 2. 3. 2. 2 (**Figure 2-4 a**).
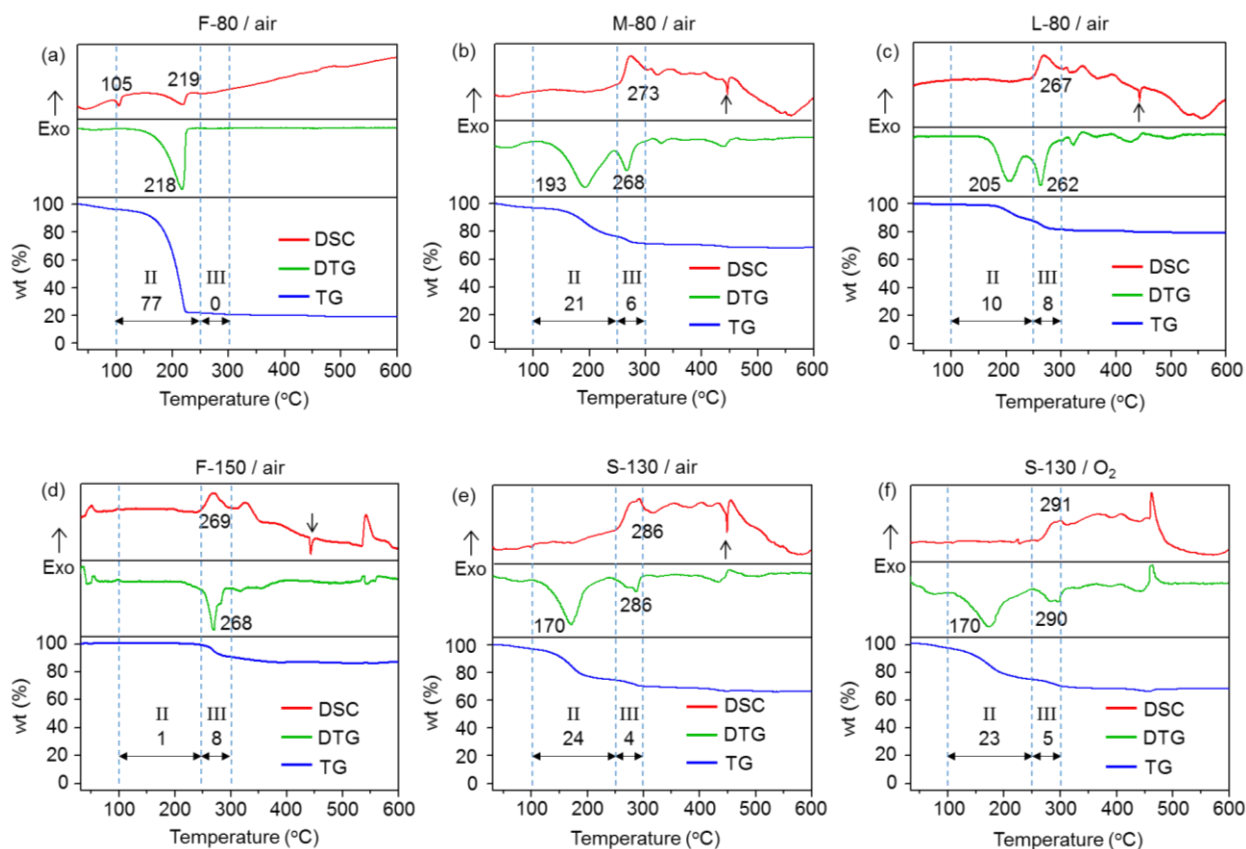
Figure 2-6 TG-DTG-DSC analysis of various *xerogel* powders under gas flow of 20% O_2 / 80% N_2 (referred to as air in the name panel of each sub-figure), or 80% O_2 / 20% N_2 (referred to as O_2 in the name panel of the sub-figure). Other preparation conditions (*sol* aging time and *sol* heating temperature) for the *xerogel* samples are given in the name panel above each sub-figure. The temperatures listed in the graphs of the DTG and DSC curves correspond to the DTG and DSC dips/peaks in regions of II and III, respectively. The numbers above the horizontal arrows at the bottom panel of each graph represent wt% of weight loss in regions II and III, respectively, normalized to total weight loss in these two regions. The short black vertical arrows pointing at the endothermic dip of 446-449 °C at the top panel of DSC curves assign to the melting of metallic-Te. The ratios of weight loss in region III over region II are 0.0, 0.3, 0.8, 8.0 and 0.2 for F-80, M-80, L-80, F-150, S-130, respectively.

The TG-DTG-DSC curves of all *xerogel* powders can be classified into five different regions (I-V) as shown in **Figure 2-6**:

I: 30 to 100 °C: The residual solvent evaporation leads to small TG weight loss of 1-4% for various *xerogel* powders.

II: 100 to ~250 °C: The liberation of OGs via an endothermic reaction results in varying weight loss, corresponding to the DTG peak with an endothermic DSC dip.

III: ~250 to 300 °C: The weight loss relevant to the liberation of OGs via an exothermic reaction appears in this region, indicated by the DTG peak in accompany with an exothermic DSC peak. This observation is opposite to the endothermic liberation of OGs in region II.

IV: 300 to ~500 °C: Negligible weight loss is observed for all *xerogel* samples heated at temperatures > 300 °C, indicating the OGs are completely removed. The pronounced narrow endothermic DSC dip at 443-449 °C is ascribed to the melting of metallic-Te in accordance with the melting temperature of bulk tellurium (449 °C) [51]. This suggests metallic-Te is formed in S/M-80, S-130 and F-150 samples. The absence of the metallic-Te peak in the F-80 sample is related to the evaporation of Te-alkoxide prior to forming metallic-Te (detailed explanation in the supporting information). The exothermic DSC peaks at ~360, ~400 and ~460 °C are attributed to the formation of TeO_2, $ZnTeO_3$ and $Zn_2Te_3O_8$ crystals as identified in tellurite glass (**Figure S. 3**) [52-54] and in S-130-400 and S-130-500 glass films (**Figure 2-4 d**).

V: >500 °C: Further increase of the heating temperature melts the crystals formed in the region IV and the glass film itself, corresponding to the broad endothermic dip with negligible weight loss.

In regions II and III, the different *xerogel* samples show profound differences of weight losses, as indicated in the caption of Figure 4. With increasing *sol* aging time, the ratio of weight loss in region III is enhanced relative to region II, e.g., from 9 to 300 days, the ratio increases from 0.2 to 0.8. The ratio is particularly large with a value of 8 for the *sol* heated at 150 °C. In addition, with

increasing *sol* aging time, the total weight loss over 100-300 ºC in regions II and III decreases (from 77% for 9 days to 18% for 300 days). Surprisingly, the use of 150 ºC *sol* heating temperature leads to a particularly low weight loss (9%). Given that the weight loss during *xerogel* heating (in regions II and III) originates from the liberation of OGs, these results suggest that OG liberation is highly dependent on the conditions of preparing *xerogel*, including *sol* aging and *sol* heating.

For the *xerogel* powder samples (S/M-80, S-130 and F-150) and the *xerogel* film samples (S-130-200 and S-130-300), both the metallic-Te formation and OG liberation coincide in the same temperature range of 160-300 ºC. This strongly implies that the liberated OGs reduce Te(IV) into Te(0), i.e., the formation of metallic-Te [11]. Therefore, the decisive factor in determining the formation of metallic-Te is closely related to the conditions used to prepare the *xerogel* samples. To elucidate this interrelation, we studied how these conditions affect the polymerization reactions and in which way they govern the amount of OGs in the *xerogel*.

2. 3. 2. 5 Polymerization reactions forming the xerogel network

The polymerization process of addition reaction (so-called addition polymerization) has been demonstrated to generate a *xerogel* network via binding the Te-alkoxide precursor molecules [11]. Initially, the Te-O bond weakened by LPE would be subject to heterolytic cleavage of Te-O and C-O bonds (in different Te-alkoxide precursor molecules, as shown in the grey box in **Figure 2-7**). New covalent C-O-C bonds are subsequently formed between these disrupted molecules, and weak intermolecular Te···O-Te bonds are transformed to strong intramolecular Te-O-Te bond. In this process, an O-R-O group with R=CH(CH$_3$)-CH$_2$ (hereafter referred to as cyclic group) is disrupted

and transformed into a short -O- bridge (hereafter referred to as oxo bridge) and a long -O-R-O-R-O- bridge (hereafter referred to as alkoxy bridge).
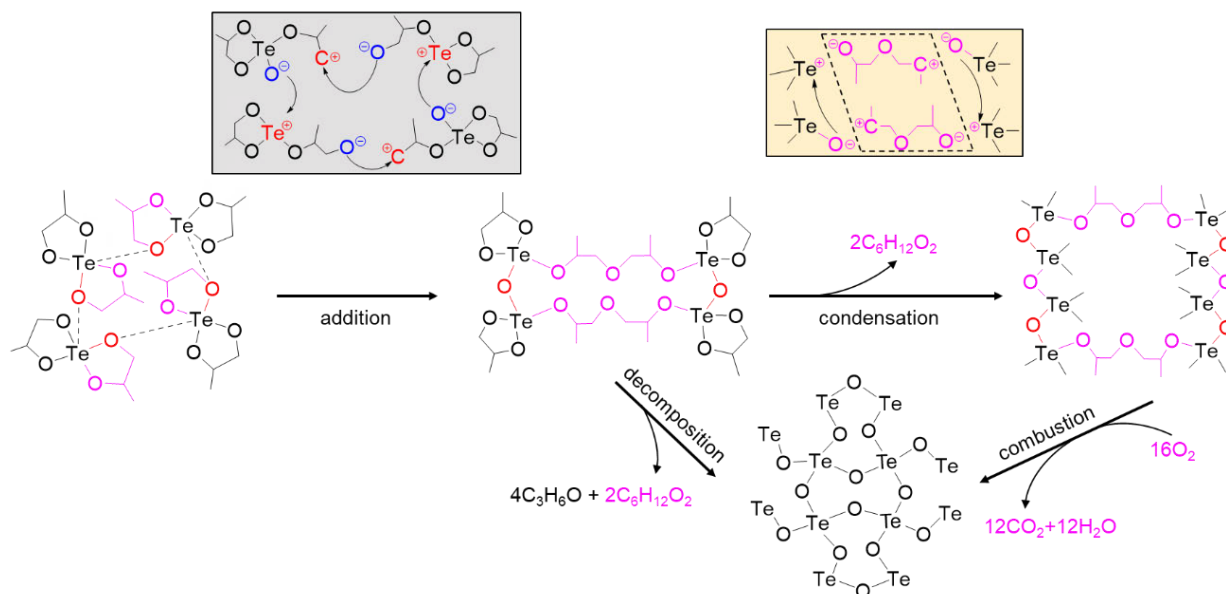
Figure 2-7 Schematic illustration of the chemical formulae of the reactions towards forming dense TZN glass. The weakly linked Te-alkoxide molecules are used as a precursor to produce a ring-shaped molecule via addition reaction. The ring-shaped molecules undergo either a decomposition reaction, or sequential condensation and combustion reactions to generate an inorganic glass network. The schematics in the shaded boxes show the respective bond forming mechanisms: addition polymerization reaction (grey box) initialized by the Te-O and C-O bond cleavages within Te-alkoxide molecules, and condensation polymerization reaction (light-yellow box) within alkoxy bridges.

For our TZN *sol* composition with molar ratio of 80 Te-alkoxide: 10 Zn-acetate: 20 Na-acetate, the complete removal of all OGs, i.e. the liberation of $C_6H_{12}O_4$ from $Te(O_2C_3H_6)_2$, and $C_4H_6O_4$ from $Zn(C_2H_3O_2)_2$ and $(NaC_2H_3O_2)_2$, corresponds to a theoretical weight loss of 44 wt%. Intriguingly, the experimental weight losses in regions II and III for the *xerogel* samples of M/L-80, S-130 and F-150 are within 9-28 wt% (**Figure 2-7**), all of which are considerably lower than

31

the theoretical weight loss. Since the liberation of OGs is completed at the upper bound temperature of region III (300 °C), the weight loss discrepancy between the experimental observation and theoretical expectation can only result from the liberation of OGs prior to the TG-DSC analysis. In other words, a part the of OGs is already liberated during *sol* aging and *sol* heating before *xerogel* heating.

The liberation of OGs during *xerogel* preparation suggests that the condensation polymerization, which is accompanied with elimination of OGs, is involved in forming the *xerogel* network, rather than only the addition polymerization as proposed in Ref [11]. This agrees with the fact that the condensation reaction is the leading polymerization mechanism in *sol-gel* chemistry [55]. As the addition reaction involves C-O and Te-O bond cleavages within cyclic groups of different Te-alkoxide molecules (grey box in **Figure 2-7**), we propose that the condensation reaction occurs concurrently within the same alkoxy bridge via C-O and Te-O bond cleavages (light-yellow box in **Figure 2-7**), leading to new oxo bridges between Te atoms through the release of small OGs.

Given that the condensation reaction is based on bond cleavages within alkoxy bridges that are formed via addition reaction, the condensation reaction can only proceed with the occurrence of the addition reaction. This agrees with the previous report that the condensation reaction in *NHSG* systems is catalysed by their own reaction products [55]. Accordingly, we identify that both polymerization reactions contribute to the resultant *xerogel* network to different extents, depending on the *sol* aging time and *sol* heating temperature used to prepare the *xerogel*.

In conclusion, the evolution of the *xerogel* network commences with the addition reaction, leading to the formation of alkoxy bridges, which allows the condensation reaction to occur concurrently. Both polymerization processes contribute to the formation of the resultant *xerogel* network to different extents depending on the *sol* aging time and *sol* heating temperature employed to prepare

the *xerogel*. To reveal the impact of the extent of the polymerization reactions on the thermal behaviour of a *xerogel*, we developed the following structural model of [TeO$_4$] polyhedra in the *xerogel* network.

2. 3. 2. 6 Structural model of the xerogel network

Analogous to the structural units of TeO$_2$ crystals and TeO$_2$-based glasses, the basic unit of Te-alkoxide is a trigonal bipyramidal [TeO$_4$] polyhedron with the oxygen atoms at four corners [56]. These bipyramidal [TeO$_4$] polyhedra can be connected either via oxo bridges (i.e. two adjacent polyhedra share a corner, as in crystalline and amorphous TeO$_2$) [56] or via alkoxy bridges (i.e. two adjacent polyhedra share an alkoxy bridge) in the *xerogel* network. This flexibility leads to various types of polyhedral [TeO$_4$] to constitute the *xerogel* network, as depicted in **Figure 2-8**:

- 'P' polyhedra (***precursor molecules***): They refer to [TeO$_4$] polyhedra only consisting of cyclic groups. They are dispersed individually without forming oxo or alkoxy bridges with adjacent polyhedra. 'P' polyhedra are found in a low-degree polymerized *xerogel* network.

- 'O' polyhedra: These are formed via condensation reaction that liberates OGs, leading to the formation of **o**xo bridges. Therefore, alkoxy bridges are absent in 'O' polyhedra.
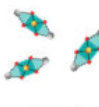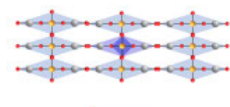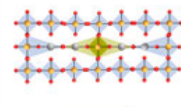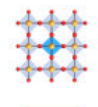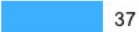
- 'A' polyhedra: These are formed via addition reaction that forms at least one ***alkoxy bridge***. An 'A' polyhedron exhibits either (1) one cyclic group, one oxo bridge and one alkoxy bridge, or (2) two oxo and two alkoxy bridges. The presence of alkoxy bridges makes 'A' polyhedra the source of liberating OGs upon heating. The bond rearrangements (bond cleavages and bond formation) during OG liberation result in two types of 'A' polyhedra that differ by the presence or

absence of alkoxy bridges in their second and third nearest neighbourhood, as illustrated in Figure 2-8. Specifically,

- 'Aa' polyhedra: They are surrounded by other 'A' polyhedra via alkoxy bridges, i.e. they are embedded in a network with many alkoxy bridges and cyclic groups.

- 'Ao' polyhedra: They are surrounded by 'O' polyhedra.

Figure 2-8 Schematic illustration of the 4 types of [TeO$_4$] polyhedra constituting the *xerogel* network: 'P' polyhedron: ; 'Aa' polyhedron: ; 'Ao' polyhedron: ; and 'O' polyhedron: . The deep-colour squared frames of the molecular structures designate the [TeO$_4$] polyhedron, and the light-colour regions specify the atoms belonging to a [TeO$_4$] polyhedron in terms of respective weight ratio. The horizontal-coloured bars designate the weight ratios of the different types of polyhedra in the *xerogels* prepared using different times and temperatures.

The short oxo and long alkoxy bridges exhibit different conformational mobility, which leads to high and low steric hindrance of the polyhedra network, respectively. As the polyhedra differ in their types of bridges (and thus in their conformational mobility), the four types of polyhedra cause different liberation rates of OGs, i.e., different thermal behaviours upon heating (**Figure S. 4**):

- 'P' polyhedra are essentially precursor molecules and thus are expected to show the same thermal behaviour as Te-alkoxide crystals (**Figure S. 5**), namely melting at ~105 °C and evaporation at higher temperatures ≤250 °C. This leads to large weight loss in region II.

- 'Aa' polyhedra are connected via alkoxy-bridges with high conformational mobility. Thus, they liberate their OGs via endothermic decomposition, resulting in weight loss in the low temperature range of region II.

- 'Ao' polyhedra are surrounded by polyhedra with low conformational mobility. Therefore, they require the surplus energy of exothermic combustion to liberate OGs, leading to weight loss in the high temperature range region III.

- 'O' polyhedra do not have alkoxy bridges and thus do not show OG liberation. They constitute the weight remains at the end temperature of region III.

2. 3. 2. 7 Interrelation of sol aging time and heating temperature on OGs content in xerogel samples

The characteristic thermal behaviour of each type of $[TeO_4]$ polyhedron allows us to determine their weight fractions in the respective *xerogel* samples (detailed explanation and calculation given in the supporting information associated with **Figure S. 4**).

The F-80 *xerogel* consists of 'Aa' polyhedra (41 wt%) and 'P' polyhedra (59 wt%). The large portion of 'P' polyhedra suggests that only a portion of the precursor molecules is involved in polymerization due to the short *sol* aging time (e.g., 9 days) and the low *sol* heating temperature (e.g., 80 °C over 3 days). The absence of 'Ao' and 'O' polyhedra indicates that the condensation reaction does not proceed to a considerable extent during the short *sol* aging time and at the low

sol heating temperature. The evaporation of 'P' polyhedra during heating of F-80 *xerogel* causes large weight loss (Te-alkoxide precursor begins to evaporate at 100 °C, **Figure S. 5**), suggesting the F-80 *xerogel* is not an appropriate option to prepare a glass film.

For the M-80 and L-80 *xerogel* samples, the fractions of 'Ao' and 'O' polyhedra increases with *sol* aging time. This indicates that condensation reaction occurs progressively as a function of *sol* aging time, which consequently increases the fractions of 'Ao' and 'O' polyhedra, leading to a reduced amount of OGs that is liberated during *xerogel* heating.

Compared to S-130, M-80 contains a lower amount of 'Aa' polyhedra but higher amounts of 'Ao' and 'O' polyhedra (**Figure 2-8**). Since the condensation reaction is facilitated with prolonged aging time, this result indicates that the longer *sol* aging time (90 days for M-80 versus 60 days for S-130) considerably increases the formation of 'Ao' and 'O' polyhedra.

Despite the short aging time of only 9 days, F-150 shows a network mainly composed of 'O' and 'Ao' polyhedra with minor portions of 'Aa' polyhedra (**Figure 2-8**). This result indicates that, due to thermally enhanced bond cleavage and re-arrangement, 150 °C *sol* heating temperature particularly facilitates the condensation reaction.

The different portions of $[TeO_4]$ polyhedra in F-80 and F-150 *xerogel* samples account for their different behaviour in the liberation of OGs. Due to the evaporation of 'P' polyhedra and decomposition of 'Aa' polyhedra F-80 shows only a DTG peak in region II, while due to combustion of 'Ao' polyhedra, F-150 presents almost only a DTG peak in region III. To shed more light on the liberation of OGs via decomposition and combustion in different temperature regions, these two samples with contrasting thermal behaviour were analysed by vapor-FTIR spectroscopy.

Figure S. 6 displays the temperature dependence of the FTIR bands for the vibrational bonds O-H (stretching: 3400 to 3700 cm⁻¹), C=O (stretching: 1700 to 1830 cm⁻¹) [57, 58], C-H (stretching: 2800

to 2931 cm^{-1}, bending: 1300 to 1400 cm^{-1}) [59, 60], C-O (stretching: 917 to 1226 cm^{-1}) [61], and Te-O (stretching: 600 to 660 cm^{-1} in [TeO$_4$] polyhedron) [62]. The F-80 sample shows released compounds with Te-O and C-H bonds as well as an increased amount of compounds with C-O and C=O bonds in the range of 180-210 °C. This agrees with the TG-DSC results, showing precursor evaporation and alkoxy bridge decomposition starting at >100 °C, peaking at 219 °C and finishing at 230 °C. No enhanced amount of CO$_2$ was found in the gaseous release from the F-80 sample. By contrast, the F-150 sample shows no C-H, C-O and C=O groups but release of vapor containing CO$_2$ which appears at 220 °C and reaches highest amount at 300 °C. The release of CO$_2$ due to combustion is in good agreement with the TG-DSC result of F-150 sample, which shows combustion commencing at 250 °C, peaking at 269 °C and finishing at 300 °C. The absence of Te-O bonds in the vapor-FTIR of F-150 sample indicates a lack of precursor evaporation, which is consistent with the TG-DSC result and ascribed to the high degree of polymerization.

It is also worth noting that with increasing 'Ao' and 'O' polyhedra content, the peak temperature of the decomposition increases while the peak temperature for combustion slightly decreases (**Figure S. 7**). The increased 'Ao' and 'O' contents are accompanied with enhanced steric hindrance and reduced amount of OGs. A higher steric hindrance hampers the decomposition, thus requiring higher thermal activation. The lower amount of OGs is likely to facilitate the combustion, leading to reduced combustion temperature. These results consolidate the correlation of the decomposition and combustion with the steric hindrance imposed by oxo bridges around alkoxy bridges.

In summary, the high *sol* heating temperature of 150 °C was found to have a remarkable impact. Compared to both S-130 and L-80, F-150 has a higher amount of 'O' polyhedra despite the short *sol* aging time of 9 days relative to 30 days for S-130 and even 300 days for L-80. This indicates

that the effect of temperature increasing from 80 or 130 to 150 ºC counterbalances the effect of *sol* aging time decrease from 300 or 30 to 9 days. The highest amount of 'O' polyhedra for F-150 of all *xerogel* samples suggests that its *xerogel* network is mainly formed via condensation. As a result, a large amount of OGs is liberated during *xerogel* preparation and only a small residual amount of OGs is released during *xerogel* heating. This is beneficial to suppress the formation of metallic-Te.

2. 3. 2. 8 Suppression of metallic-Te formation by the provision of O_2

For the *xerogel* samples heated under dry air, the endothermic DSC peak at ~449 ºC corresponds to the melting of metallic-Te. This suggests that even the lowest amount of OGs in the F-150 *xerogel* causes the formation of metallic-Te when heated in air. Therefore, in order to suppress the metallic-Te formation, the liberated OGs need to be oxidized prior to their involvement in reducing Te(IV). For this purpose, the impact of O_2 during *xerogel* heating was investigated via TG-DSC measurement of the S-130 *xerogel* sample (containing a medium amount of OGs of all investigated *xerogel* samples). This TG-DSC analysis was carried out under O_2-rich atmosphere (80% O_2 and 20% N_2) compared to dry air (20% O_2 and 80% N_2). The purging of O_2-rich atmosphere during *xerogel* heating eliminated the melting peak of metallic-Te (449 ºC) (Figure 4e versus f), which proves that the provision of O_2 facilitates the oxidization of the liberated OGs and thus has the potential to prevent metallic-Te formation.

2. 3. 2. 9 Optimal chemical route to synthesize metallic-Te free TZN glass film

The insights into formation, evolution and thermal behaviour of different types of $[TeO_4]$ polyhedra in *xerogel* samples demonstrated that the appropriate choice of *sol* aging time, *sol* heating temperature, and O_2 atmosphere is critical. To identify the optimal synthesis conditions for transparent TZN glass films, conditions that enable complete transformation of precursor molecules into a *xerogel* network and finally a dense OG-free and crystal-free glass structure were selected. Specifically, short *sol* aging time (20-80 days), low and high *sol* heating temperatures (80 ºC and 150 ºC), and *xerogel* heating temperature (300 ºC) were investigated (S-80-300 and S-150-300 samples). In addition, impact of dry O_2 flow compared to ambient air atmosphere was explored. It is worthwhile to note that dry O_2 flow was used during both the *sol* heating and the *xerogel* heating processes. O_2 flow during *sol* heating allows diffusion of excess O_2 into the *xerogel* films, which is then available to react with the liberated OGs in the subsequent *xerogel* heating process. O_2 flow during *xerogel* heating is conducted to suppress the out-diffusion of O_2 from *xerogel* films.

To quantitatively analyse the content of metallic-Te in the glass films, optical micrograph, UV-Vis transmission spectroscopy, confocal microscopy and fluorescence spectroscopy were utilized.
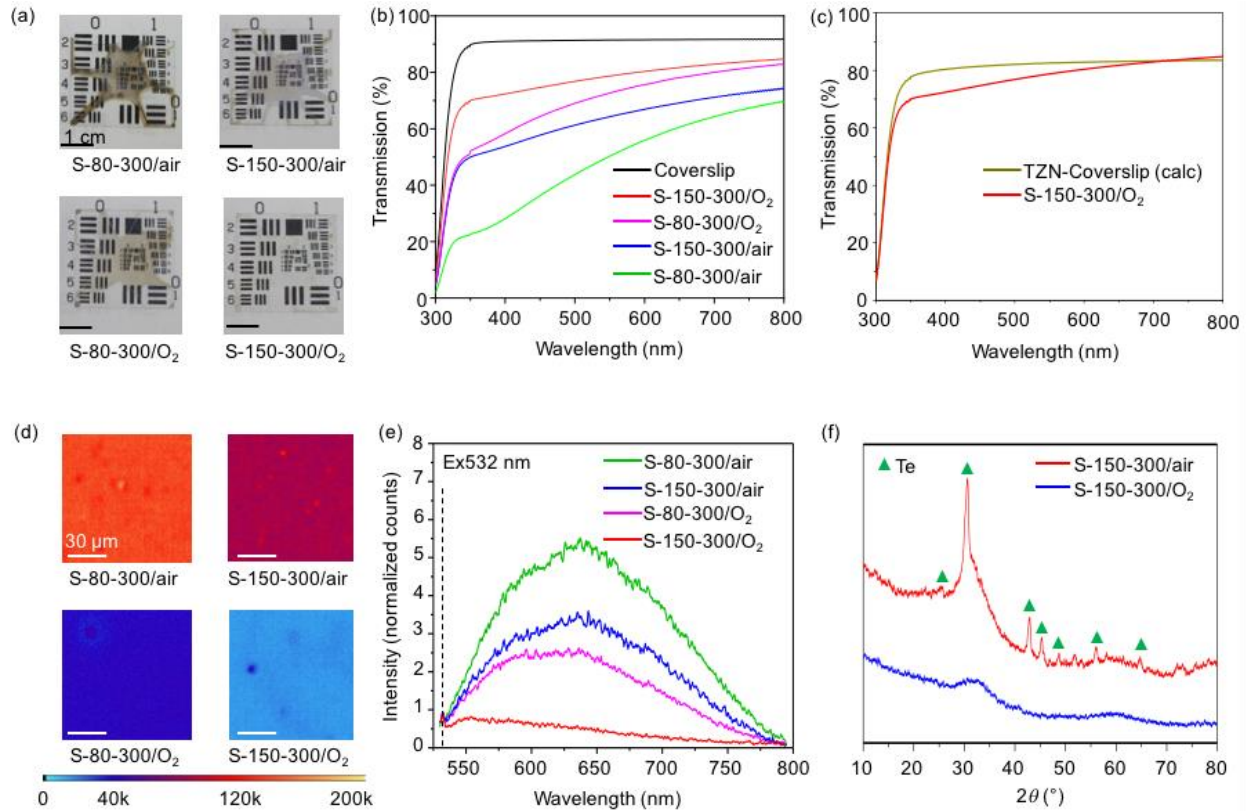
Figure 2-9 Optical and structural characterizations of TZN glass films prepared under different temperatures and atmospheres in the course of *sol* heating and *xerogel* heating. (a) Photographs and (b) Experimental transmission spectra of various *xerogel* samples. (c) Theoretical transmission spectrum of $75TeO_2$-$15ZnO$-$10Na_2O$ glass [20] on D 263™ T coverslip, relative to the measured transmission spectrum of S-150-300/O_2. (d) Confocal microscope images, and (e) Fluorescence spectra of TZN glass films on glass coverslips. The fluorescence spectra were taken from arbitrary spots of the films and normalized to the excitation power of 532 nm (2.56 µW for all measurements). (f) Micro-XRD patterns of TZN films on Si wafers, showing the characteristic diffractions of metallic-Te and the amorphous structure with a broad 'hump' at ~32°.

For both air and O_2 atmosphere, the S-150-300 samples exhibit lower intensities of the characteristic metallic-Te properties (brown colour, reduced UV-Vis transmission and presence of fluorescence) than the S-80-300 samples (**Figure 2-9**). The higher *sol* heating temperature of S-

150-300 enhances the condensation reaction, which decreases the amount of OGs and thus suppresses the metallic-Te formation.

For the glass films prepared at the same *sol* heating temperature, the use of O_2 flow markedly reduces the intensities of the characteristic metallic-Te properties (**Figure 2-9**). However, for the S-80-300/O_2 sample, light brown colour, and slightly reduced UV-Vis transmission and pronounced fluorescence were still observed. This indicates that inhibiting the metallic-Te formation cannot only rely on the use of O_2, but must be used in combination with suitable *sol* aging time and *sol* heating temperature.

The S-150-300/O_2 film shows the absence of the characteristic metallic-Te properties, as well as the omission of the characteristic diffractions of metallic-Te. As a result, the S-150-300/O_2 film shows a transmission that is closest to the theoretical transmission limit given by the Fresnel reflection for a TZN film on a coverslip and the UV edge of the coverslip (**Figure 2-9 c**, calculation of the theoretical transmission limit provided in supporting information) [21]. Specifically, the transmission is within 10% of the theoretical limit for wavelengths <700 nm and at the theoretical limit for wavelengths >700 nm. The lower transmission between 350-700 nm is attributed to the Rayleigh scattering effect of the film surface roughness.

2. 3. 3 Summary

We have elucidated the mechanisms of forming metallic-Te during the different steps of the NHSG route. We unravelled that the use of O_2 during the film preparation is not sufficient to completely prevent the metallic-Te formation, since the amount of OGs in the *xerogel* films plays a decisive role in determining the formation of metallic-Te during the subsequent heating to form a dense

glass film. Therefore, the use of O_2 need to be combined with appropriate choice of *sol* aging time and *sol* heating temperature to minimize the amount of OGs in the *xerogel* films.

This in-depth understanding allowed us to develop a synthesis protocol to produce metallic-Te free TZN films. Firstly, we applied *sol* aging at room temperature for 30-60 days, which allowed all precursor molecules to undergo polymerization via addition and condensation reactions. Secondly, we used *sol* heating temperature at 150 °C to accelerate the condensation reaction, which leads to the highest 'O' polyhedra content and the lowest OGs fractions of all *xerogel* samples investigated. Thirdly, we constantly purged O_2 during both the *sol* heating at 150 °C and the *xerogel* heating at 300 °C, so that the liberated OGs react with the O_2 to form volatile gases rather than with Te(IV) to generate metallic-Te.

The absence of metallic-Te in the TZN film synthesized using these optimal conditions led to a high optical transmission over the whole intrinsic transmission window of tellurite glass, i.e. from the UV to the infrared range. To the best of our knowledge, this is the highest transmission achieved for a tellurite *sol-gel* glass films relative to the theoretical limit. Reducing the surface roughness of the films is expected to minimize the scattering-induced transmission loss in the visible spectral range. The preparation of high-transmission TeO_2-based *sol-gel* glass films paves the way to develop hybrid optoelectronic films by incorporating diverse nanoparticles with unique functionalities.

Chapter 3 - TeO₂-based ionic conductive glass

3. 1 Literature review and research design

3. 1. 1 Mechanism of ionic conduction

Ionic conduction in solid state materials relies on the diffusion of mobile ions driven by an external electrical field [63-65], where the mobile ions play the role as charge carrier. The ionic conductivity can be described by the Nernst-Einstein expression [64]:

$$\sigma = nq^2 D/k_B T \qquad\qquad 3.1$$

where apart from Boltzmann's constant (k_B), the conductivity (σ) is determined by temperature (T), the charge (q), concentration (n) and diffusion coefficient (D) of mobile ions. For instance, it shows that under constant temperature, ionic conductivity is determined by the concentration and diffusion coefficient. The diffusion coefficient to measure the mobility of mobile ions, which is expressed as [66]:

$$D = a^2 v/6 \qquad\qquad 3.2$$

where a is the distance between the sites where the ions hop, and v is the migrating frequency, 6 is the geometry factor originated from the isotropic nature of the glass. According to the above equations 3.1 and 3.2, the ionic conductivity depends on the:

1) the concentration of mobile ions (alkali ions for the ionic conductive glasses). At absolute zero (-273.15 °C), the alkali ions that are weakly linked to the anions in a glass are immobile. At room temperature (25 °C), the thermal energy can excite a portion of alkali ions to be mobile [64, 67]. Hence, when higher temperature or an external electric field is applied, a higher portion of alkali ions are activated to be mobile [67].

2) the factor a, which is related to atomic configuration and the space of mobile ions in glass.

3) the frequency of alkali ions traveling from one site to another is referred to as the hopping frequency ν, which depends on the free energy barrier of ions hopping between two sites (E_ν) and the site frequency (υ_0):

$$\nu = \upsilon_0 \exp\left(-\frac{E_\nu}{k_B \mathrm{T}}\right).$$

3.3

3. 1. 2 Literature review and gap identification

3. 1. 2. 1 Literature review of the impact of halides on glass properties

This section reviews the impact of introducing halides to oxide glass systems (SiO_2- [68, 69], B_2O_3- [70, 71], P_2O_5- [72, 73] and TeO_2-based [74]) on their ionic conductivity and structure. The replacement of the alkali-oxide (e.g. Li_2O or Na_2O) in B_2O_3-based glasses by alkali-halide was found to result in the increase of ionic conductivity (**Table 3-1**) [70, 71]. H. Jain et.al discovered that [71], the halide ions exist in the interstitial sites of the network formed by glass former (no boron-halide bond formed), thus opening the glass network and creating more space for the migration of mobile ions [71]. Furthermore, the energy required to break the weakly linked lithium-halide bond is lower than that for the lithium-oxygen bond [72]. Due to the expansion of network and the reduction of binding energy, the conductivity of B_2O_3-Li_2O glass increases as Li_2O is replaced by LiX. A larger ionic size of halide opens the network thus benefits the conductivity as evidenced by the enhanced conductivity for Br against Cl (**Table 3-1**).

The conductivity of P_2O_5-based glasses increases as the concentration of halide increases (**Table 3-1**) [72, 75]. Steve W, Martin (1991) reviewed the research on the ionic conductive $LiPO_3$-LiX (X=Cl, Br, I) glasses [72], he found that the conductivity follows an order of $70LiPO_3$-$30LiI >$ $70LiPO_3$-$30LiBr > 70LiPO_3$-$30LiCl > 100LiPO_3$. He explained this phenomenon based on the consideration of the bond energies following the order of Li-I < Li-Br < Li-Cl. This order suggests

the mobile Li^+ ion (charge carrier) concentration of $70LiPO_3$-$30LiI$ is higher than that of $70LiPO_3$-$30LiBr$ and $70LiPO_3$-$30LiCl$. Bruno Poletto Rodrigues et al. (2019) found that the activation energy (of DC conductivity) of $60NaPO_3$-$40NaCl$ glass is lower than that of $100NaPO_3$ glass [75]. They also discovered that the number of charge carriers is reduced while the ion mobility is improved by adding NaCl to $NaPO_3$ glass. The enhanced conductivity of the $60NaPO_3$-$40NaCl$ glass suggests the extent of ion mobility increase is larger than the charge carrier concentration decrease. The ion mobility is enhanced, because the network is opened by the Cl^- ions located in the interstitial sites of the network.

The conductivity of SiO_2-based glasses is improved by adding halides [68, 69]. A. Abd El-Mongy investigated the conductivity and the molar volume of SiO_2-Na_2O-NaX (X=Cl, Br, I) glasses and revealed that, the glasses containing NaI have a higher conductivity then those containing NaBr and NaCl [69]. Furthermore, the molar volume is increased as Na_2O is substituted by NaX, suggesting the network is opened by the halides. Since I^- has a larger size then Br^- and Cl^-, SiO_2-Na_2O-NaI glass has the highest conductivity. It was hypothesized that the halides form Si-X bond with Si, but no evidence has been provided to support this proposition.

The conductivity of $70TeO_2$-$30Li_2O$ decreases as Li_2O is replaced by LiX (X=Cl, Br). For $60TeO_2$-$40Li_2O$, the conductivity increases as the Li_2O is replaced by LiCl. When the Li_2O of $60TeO_2$-$40Li_2O$ is replaced by LiBr, the conductivity is firstly increased then decreased (**Table 3-1**) [74]. Katsuhisa Tanaka et.al observed in IR spectra that, as the Li_2O is replaced by LiCl, the band corresponding to the vibration of Te-O at equatorial direction decreases distinctly. They explained this observation as follows: the halides added to the TeO_2-based glass replace the oxygen of tellurium-oxygen polyhedra and form Te-X bonds [74, 76, 77]. It was not mentioned in the paper whether the bridging oxygen or non-bridging oxygen was replaced. This replacement of oxygen

by halide is supported by the Bent's rule [78]: the element with lower electronegativity favours the orbitals rich in s character. As Cl and Br have lower electronegativities then O, they preferentially occupy the equatorial position of tellurium-oxygen polyhedron rich in s character. Katsuhisa Tanaka et.al also found that, the glass transition temperatures (Tg) of TeO_2-Li_2O-LiBr glasses are higher than those of TeO_2-Li_2O and TeO_2-Li_2O-LiCl glasses. Compared to the TeO_2-Li_2O glass, the higher Tg of the LiX-containing glass indicates a compacter glass network, which is caused by the formation of Te-X bond. Therefore, Katsuhisa Tanaka et.al suggested that the formation of Te-X bond is responsible for the decrease of $70TeO_2$-$(30-x)Li_2O$-$xLiX$ glass conductivities. However, I remain skeptical towards this statement. I speculate that, the decrease of conductivity is attributed to the reduction of Li^+ ion concentration. Since one Li_2O was replaced by one LiX, the concentration of Li^+ ion was reduced by half. For the variation of the conductivity of $60TeO_2$-$(40-x)Li_2O$-$xLiX$ glasses, no explanation was presented in the paper by Katsuhisa Tanaka et.al.

Table 3-1 Conductivity or activation energy data of B_2O_3-, P_2O_5, SiO_2, and TeO_2-based glasses (with and without halides) adopted from literatures.

Glass type	halide in network	Changes	Composition	σ S/cm	Ea eV	Trend
B_2O_3-based (200 °C) [71], (150 °C) [79]	X$^-$ ions exists in the interstitial sites of boron-oxygen network (proved by IR spectra [80])	Weaken the boron-oxygen glass network, open the structure, reduce the attraction of Li$^+$ ions to non-bridging oxygen	$65B_2O_3$-$35Li_2O$	$10^{-6.6}$		σ increase
			$65B_2O_3$-$31Li_2O$-$4LiCl$	$10^{-6.4}$		
			$65B_2O_3$-$31Li_2O$-$4LiBr$	$10^{-6.4}$		
			$65B_2O_3$-$35Na_2O$	10^{-7}		
			$65B_2O_3$-$31Na_2O$-$4NaCl$	$10^{-6.6}$		
			$65B_2O_3$-$31Na_2O$-$4NaBr$	$10^{-6.6}$		
			$70B_2O_3$-$30Li_2O$	$10^{-6.2}$		σ increase
			$70B_2O_3$-$21Li_2O$-$9(LiCl)_2$	$10^{-5.4}$		
			$70B_2O_3$-$23Li_2O$-$7(LiBr)_2$	$10^{-4.9}$		
P_2O_5-based (RT) [72], Ea [75]	Not mentioned	Mobile Li$^+$ ion concentration increases (hypothesis)	$100LiPO_3$	$10^{-8.8}$		σ increase
			$70LiPO_3$-$30LiCl$	10^{-7}		
			$70LiPO_3$-$30LiBr$	$10^{-6.7}$		
			$70LiPO_3$-$30LiI$	10^{-6}		
	Occupy the interstitial spaces (cited from [81])	Enhance Na$^+$ mobility, decrease mobile Na$^+$	$100NaPO_3$		0.73	Ea decrease
			$60NaPO_3$-$40NaCl$		0.55	
SiO_2-based [69]	forming Si-X bonds (hypothesis of authors)	Increasing the molar volume	$75SiO_2$-$25Na_2O$		0.85	Ea decrease
			$75SiO_2$-$5Na_2O$-$20NaCl$		0.69	
			$75SiO_2$-$5Na_2O$-$20NaBr$		0.685	
			$75SiO_2$-$5Na_2O$-$20NaI$		0.64	
TeO_2-based (100 °C) [74]	Forming Te-X bonds (proved by IR spectra [76, 77])	Compact glass network, Li$^+$ ion decreases	$70TeO_2$-$30Li_2O$	$10^{-8.9}$		σ decrease
			$70TeO_2$-$5Li_2O$-$25LiCl$	$10^{-9.7}$		
			$70TeO_2$-$5Li_2O$-$25LiBr$	$10^{-9.7}$		
		Weaken the glass network, Li$^+$ ion decreases	$60TeO_2$-$40Li_2O$	$10^{-8.2}$		σ increase
			$60TeO_2$-$20Li_2O$-$20LiCl$	$10^{-7.6}$		
			$60TeO_2$-$8Li_2O$-$32LiCl$	$10^{-7.5}$		
			$60TeO_2$-$40Li_2O$	$10^{-8.2}$		σ increase then decrease
			$60TeO_2$-$20Li_2O$-$20LiBr$	$10^{-7.5}$		
			$60TeO_2$-$8Li_2O$-$32LiBr$	$10^{-8.5}$		

3. 1. 2. 2 Identify the gaps of research on TeO₂-based conductive glasses

The gaps of knowledge on TeO$_2$-based glass containing halides (denoted as TM-X) are identified and presented in this section based on the literature review on ionic conduction and the effect of halide addition.

The theory of ionic conduction suggests the alkali ions play the role as charge carriers in TM-X glass. As defined above, the conductivity of TM-X glass depends on the concentration of alkali ions that are mobile. The mobility of alkali ions is determined by the distance between the sites for ions migration, and this distance is correlated to the free volume of the sample. Thus, the mobility can be illustrated by the free volume. The concentration of mobile alkali ions depends on both the internal atomic arrangement and external surroundings (stimuli to make the ions mobile). In general, the external conditions refer to the temperature and the external electric field that are applied to the glass. The intrinsic conditions include:

i) the concentration of added alkali ions. Mostly, a higher concentration of added alkali leads to an increase of the concentration of mobile alkali ions.

ii) the concentration of the anions that are linked to the alkali ions (i.e., non-bridging oxygen and halide ions). Although this binding is weak, it hinders the alkali ions to migrate. This type of anions is specifically denoted as alkali-binding anion in this thesis.

iii) the binding energy between alkali ions and anions. For the system with larger binding energy, it reduces the probability of alkali ion diffusion.

Katsuhisa Tanaka et.al. investigated the TeO$_2$-Li$_2$O-LiX glass, where one Li$_2$O was replaced by one LiX [82]. In this case, the molar concentration of anion (O^{2-} + X$^-$) remains constant, but the concentration of Li$^+$ is reduced. The reduced concentration of alkali ions diminishes the concentration of mobile ions thus the conductivity. However, they have not considered the

48

contribution of alkali ion concentration to the variation of conductivity. Therefore, one way to clarify the impact of halide is to maintain the concentration of alkali ion.

I believe, there are at least two aspects worth considering in terms of replacing alkali oxide by alkali halide. Firstly, this replacement decreases the concentration of alkali-binding non-bridging oxygen. Secondly, the concentration of added halide could affect the concentration of alkali-binding anion. Specifically, if the halides form Te-X via the reaction X + Te-BO-Te = Te-X + Te-NBO, the concentration of alkali-binding anion (defined as bound halide) will remain constant; if the halides exist in the interstitial sites (defined as ionic halide), the concentration of charged anion will increase. Yet it is unclear whether the first or the second effect dominates the conductivity of tellurite-halide glasses. Furthermore, Katsuhisa Tanaka et.al's work of TLL glass only covers Cl and Br, without studying I (iodine), which is larger than Cl and Br in size and electronegativity.

In summary, my thesis aims to fill the knowledge gaps about the impact of halides (including Cl, Br, and I) on the conductivity of TeO_2-based glass by maintaining the concentration of alkali ions.

3. 1. 3 Selection of glass compositions

The alkali ions Li^+ and Na^+ are widely selected as charge carrier for ionic conductive materials. Compared to Li^+, the Na^+ has a lower binding energy with anions since Na^+ has a larger size than Li^+ [83]. This means, a lower energy is required to dissociate the weak bond between Na^+ ions and anions. Therefore, when the same amount of energy is supplied to the glass with sodium or with lithium, the mobile ion concentration of the former is higher than that of the latter.

Li^+ (radius=59 pm) has a smaller radius than Na^+ (radius=99 pm) [84], which means Li^+ can have a higher mobility than Na^+. Considering the TeO_2-based glasses have an open network, which provides sufficient space for the migration of Li^+ or Na^+, the ionic size plays a less significant role on the conductivity [85]. Furthermore, sodium is a more abundant element in the Earth's crust than

lithium. The structure of the TeO_2-Na_2O glass system has been studied using Raman spectroscopy [86]. Therefore, the Na^+ is selected in this research.

The previous research on the $(100-x)TeO_2$-xNa_2O glass system demonstrated the effect of Na_2O concentration on conductivity [87]. Therefore, to achieve a higher conductivity, a binary composition with the maximum Na_2O concentration was selected as the base glass composition for the further study. To investigate the impact of halides on the conductivity of TeO_2-based glasses, the TeO_2-Na_2O-NaX glasses were prepared via substituting one Na_2O by two NaX (X=Cl, Br and I) to prepare the ternary system denoted as $68TeO_2$-$(32-x)Na_2O$-$x(NaX)_2$. The molar ratio of Te:Na is maintained to keep the concentration of sodium constant. Additionally, the crystallization was avoided for all glasses to ensure a high transparency.

3. 2 Sample preparations and characterisation methods

3. 2. 1 TeO₂-Na₂O-NaX (X=Cl, Br, I) glasses preparation

Raw materials, crucibles and furnace: Raw materials TeO_2 (99.999%, CNBM, optoelectronic materials, Chengdu, China), Na_2CO_3 (99.5%, Chem-Supply), NaCl (99.7%, Chem-Supply), NaBr (99%, General-Purpose-Reagent), NaI (99.5%, Chem-Supply) were used to prepare the specimens. All the raw materials are stored in a glovebox purged with N_2 gas. Ceramic crucible with platinum lid or gold crucible with gold lid were used for the melting process. A melting furnace (open air, Tetlow Kilns & Furnaces, Australia, customized) and an annealing furnace (open air, Ceramic Engineering Furnace Manufacturers, Australia, customized) were applied for heat treatment.

Composition, preparation, and sample coding:

$68TeO_2$-$32Na_2O$ (X-0) was selected as the base composition since it has the maximum concentration of sodium without crystallization (section 3. 3. 1). Each Na_2O of $68TeO_2$-$32Na_2O$

was substituted by two NaX (X=Cl, Br and I) to prepare the $68TeO_2$-$(32-x)Na_2O$-$x(NaX)_2$ glasses. The abbreviations for the glass systems and specimens are presented as below (**Figure 3-1**):

1) The TeO_2-Na_2O-NaX glass system is denoted as TNN, which covers all the systems introduced below.

2) TeO_2-Na_2O glass series is denoted as TN.

3) The TNN glass systems with NaCl, NaBr and NaI are specifically named as TN-Cl, TN-Br and TN-I, respectively. All the glass series with halide is denoted as TN-X.

4) The coding of each specimen is given according to the corresponding compositions. **Table 3-2** lists the sample coding and relevant information of all specimens that are presented in this thesis part.
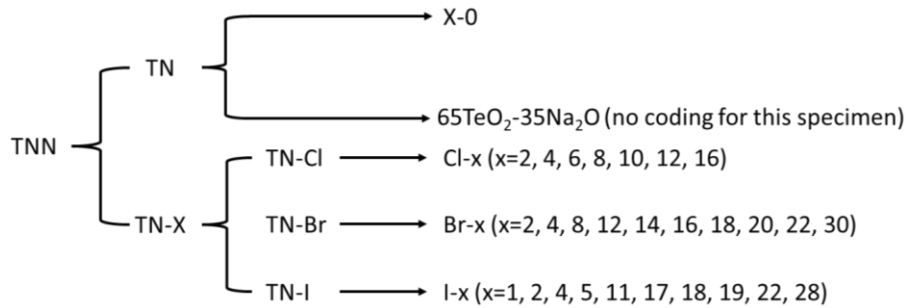
Figure 3-1 A schematic diagram showing the relationship of abbreviation for glass systems and specimens.

Table 3-2 The sample coding and the corresponding compositions of TN-Cl and TN-Br specimens presented in this thesis. The number used in coding is equal to 2x. Most of the specimens were prepared in ceramic crucible, a few of them prepared in gold crucible for comparison.

Coding	Composition			Crucible
	TeO_2	Na_2O	$(NaCl)_2$	
$65TeO_2$-$35Na_2O$	65	35	0	Ceramic
X-0	68	32	0	Ceramic/gold
Cl-2	68	31	1	Gold
Cl-4	68	30	2	Gold
Cl-6	68	29	3	Gold
Cl-8	68	28	4	Gold
Cl-10	68	27	5	Ceramic/gold
Cl-12	68	26	6	Ceramic/gold
Cl-16	68	24	8	Ceramic
	TeO_2	Na_2O	$(NaBr)_2$	
Br-2	68	31	1	Ceramic
Br-4	68	30	2	Ceramic
Br-8	68	28	4	Ceramic
Br-12	68	26	6	Ceramic
Br-14	68	25	7	Ceramic/gold
Br-16	68	24	8	Ceramic
Br-18	68	23	9	Ceramic
Br-20	68	22	10	Ceramic
Br-22	68	21	11	Ceramic
Br-30	68	17	15	Ceramic

For all glasses (except for I-17 and I-18), the raw materials TeO_2, Na_2CO_3 and NaX corresponding to 15 g $68TeO_2$-$(32-x)Na_2O$-$x(NaX)_2$ glass were firstly batched and transferred to a crucible. This step was performed in a glovebox to avoid moisture absorption. The mixture (in the crucible) was transferred to the melting furnace which had been heated to 150 °C.

For preparing all TNN glasses (except for I-17 and I-18), the temperature was ramped up from 150 °C to 450 ˚C with a rate of 20 ˚C/min and then dwelled for 2 hours at 450 °C. This step was applied to decompose Na_2CO_3 into Na_2O and CO_2 at low temperature [88], to avoid releasing large amount of CO_2 glass at high melting temperature of 750 °C, which leads to the formation of excessive

bubbles and deterioration of transparency. Subsequently, the furnace was heated up to 750 ˚C with a rate of 10 ˚C/min and dwelled for 0.5 hours to fully melt the mixtures. Finally, the melt was cast into a brass mould (30*15*18 mm^3) and placed into the annealing furnace. Both the mould and annealing furnace were pre-heated to 160 ºC to avoid thermal shock of glass specimens. The total time for this casting process was about 90 seconds, timing began as the melting furnace door was opened and ended as the door of annealing furnace was closed.

Table 3-3 Overview of the nominal concentration of NaI, melting procedure for preparing TN-I, the real compositions of prepared specimens, and concentration of evaporated NaI. Note: i) the first step of the melting procedure is 450 ºC for 2 hours for all samples.

Coding	nominal concentration (mol%)	Melting procedure		normalized real composition (mol%)			Loss (mol%)
	$(NaI)_2$	Step 2	Step 3	TeO_2	Na_2O	$(NaI)_2$	$(NaI)_2$
I-1	1	750 ºC 30 mins		68.3	31.2	0.5	0.5
I-2	2	750 ºC 30 mins		68.7	30.3	1	1
I-4	3	750 ºC 30 mins		68.7	29.3	2	1
I-5	4	750 ºC 30 mins		69.0	28.5	2.5	1.5
I-11	6	550 ºC 60 mins		68.3	26.1	5.5	0.5
I-17	10	*750 ºC 30 mins*	600 ºC 30 mins	69.0	22.3	8.6	1.4
I-18	10	*750 ºC 30 mins*	630 ºC 30 mins	68.7	22.2	9.1	0.9
I-19	11	550 ºC 60 mins		69.0	21.3	9.7	1.3
I-22	12	550 ºC 40 mins		68.7	20.2	11.1	0.9
I-28	15	550 ºC 30 mins		68.9	17.2	14.1	0.9

The annealing program was set to heat up from 160 ºC to 195 ºC with a rate of 1 ºC/min, then dwelled at 195 ºC for 2 hours. Such dwelling temperature was selected considering the glass transition temperature of $70TeO_2$-$30Na_2O$ glass at about 220 ºC [89]. Afterward, the temperature was

gradually reduced to 180 °C with a rate of 0.1 °C/min then to 150 with a rate of 0.2 °C/min, and finally to ~90 °C with a rate of 0.4 °C/min. The specimen was removed from the annealing furnace as soon as the temperature reached ~90 °C to minimize the time of exposure in open air.

X-0, TN-Cl and TN-Br showed only a small amount of weight loss (i.e. ~1%) during melting, which means the real compositions of these glasses are equal to the nominal compositions. In contrast, TN-I glasses showed significant weight loss due to the evaporation of NaI, whose melting point is 661 °C. Electron probe microanalyzer (EPMA) was used to determine the real compositions of the TN-I glasses. The weight loss was demonstrated to be attributed to the evaporation of NaI (EPMA results section 3. 2. 2). Violet gas was observed when TN-I melts were removed from the melting furnace (supplementary **Figure S. 9**). This gas could be the I_2, which has a violet colour. It is proposed that the evaporated NaI reacts with oxygen in air and produces I_2 gas (reaction 3.4).

$$4NaI + O_2 = 2Na_2O + 2I_2\uparrow. \qquad\qquad 3.4$$
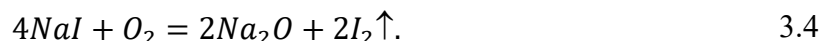
Since the melting temperature of NaI (661 °C) is lower than the temperature of the glass melt (750 °C), the TN-I glasses melted at 750 °C show significant weight loss >1%, which hinders the preparation of TN-I glasses with high NaI concentration. Therefore, temperatures lower than 661 °C were applied to prepare TN-I glasses with high NaI concentration, so that NaI evaporation could be suppressed. Specifically, two methods of preparing TN-I glasses were studied: the low-temperature melting method and the three-steps melting method (**Table 3-3**).

For the low-temperature melting method, batches with nominal $(NaI)_2$ concentration of 6, 11, 12, 15 were melted at 550 oC for 60 mins, 60 mins, 40 mins and 30 mins, resulting in the specimens I-6, I-11, I-19 and I-22, respectively.

The specimens I-17 and I-18, whose nominal compositions are both $68TeO_2$-$22Na_2O$-$10(NaI)_2$, were prepared using the three-step melting method. A piece of $68TeO_2$-$22Na_2O$ specimen was prepared via step one (450 ^{o}C for 2 hours) and step two (750 ^{o}C for 30 mins), no NaI was added for these two steps. Afterward, the as-prepared $68TeO_2$-$22Na_2O$ specimen was ground into powder and mixed with 10 $(NaI)_2$ to prepare the mixture with nominal composition of $68TeO_2$-$22Na_2O$-$10(NaI)_2$. Next, such mixture was heated for 30 mins at 600 ^{o}C or 630 ^{o}C, and resulted in glasses I-17 or I-18, respectively. The process for annealing TN-I glasses is the same as that used for TN-Cl and TN-Br glasses.

Table 3-3 summarises the nominal compositions and the real compositions, and the coding of TN-I specimens based on the real compositions. Due to the evaporation of NaI, the concentrations of Na in TN-I glasses are lower than that of nominal Na concentrations. However, considering the reduction of $(NaI)_2$ concentration is below 1.5%, this small variation of Na concentration is assumed to cause limited effects on the properties of TN-I glasses.

The samples were all prepared by Xuanzhao Pan.

3. 2. 2 TN-I real compositions measured via electron probe microanalyzer (EPMA)

The quantitative compositional measurements of TN-I glasses were performed using a Cameca SX-Five electron probe microanalyzer (EPMA), equipped with 5 tuneable wavelength-dispersive spectrometers. The instrument is running PeakSite v6.2 software for microscope operation, and *Probe for EPMA* software (distributed by Probe Software Inc.) for all data acquisition and processing. Operating conditions utilized were 15 kV/20nA with a defocused beam of 20 µm. The full list of elements analysed along with primary and interference standards are presented in supplementary **Table S. 3** & **Table S. 4**. Oxygen was calculated by stoichiometry. Matrix corrections of Armstrong-Love/Scott $\varphi(\rho z)$ [90] and Henke MACs were used for data reduction.

Beam damage and alkali element migration in glass analyses were minimized via use of a defocused electron beam, in addition to use of the Mean Atomic Number (MAN) background correction [91, 92] over traditional 2 point background interpolation. This allows single point analysis time to be greatly shortened (from ~2 min to ~30 seconds), reducing the aforementioned effects of beam damage and element migration and their subsequent impact on the quality of analysis. In addition, all elements (i.e. Te, Na, I) were analysed using the Time Dependent Intensity (TDI) correction feature of probe for EPMA [93]. Using this method, the decay of x-ray counts over time is measured and modelled to return a t=0 intercept, and from this a concentration is calculated. This is especially important for Na analysis in glass where element migration effects are prevalent, and thus can be reviewed and corrected for the analysis using this TDI method.

The collected EPMA data is presented in supplementary B 2.1 along with the calculation process. Among the measured concentrations of Te, Na and I (supplementary

Table S. 5), the concentration of I (iodine) has the lowest errors, while that of Na has the highest errors. The regional inhomogeneity of Na element is attributed to the migration of Na^+ ions. In contrast, I^- ions are immobile thus do not induce regional inhomogeneity of I elements. Therefore, the concentration of I was used to stoichiometrically calculate the x number of $68TeO_2$-$(32-x)Na_2O$-$x(NaI)_2$. The measured concentration of NaI ($NaI_{m(mol\%)}$) and real x numbers are listed in **Table 3-4**.

Table 3-4 Summary of the NaI concentration (mol%) calculated according to the weight changes and that obtained from EPMA measurements. Accordingly, the real value of 2x of $68TeO_2$-$(32-x)Na_2O$-$x(NaI)_2$ are determined by the measured NaI concentration. The sample coding is designated using the approximated values of 2x.

Coding	Nominated 2x	Calculated NaI concentration (mol%)	Measured NaI concentration (mol%)	Measured 2x
TN-1NaI	2	1.132	1.3 ± 0.05	$1.31 \approx 1$
TN-2NaI	4	2.095	2.0 ± 0.08	$2.02 \approx 2$
TN-4NaI	6	3.676	3.6 ± 0.09	$3.67 \approx 4$
TN-5NaI	8	4.908	4.7 ± 0.16	$4.81 \approx 5$
TN-11NaI	12	9.693	10.0 ± 0.25	$10.53 \approx 11$
TN-17NaI	20	15.024	15.4 ± 1.72	$16.68 \approx 17$
TN-18NaI	20	15.511	16.8 ± 0.26	$18.34 \approx 18$
TN-19NaI	20	17.032	17.6 ± 0.47	$19.30 \approx 19$
		Calculated NaI concentration	Corrected NaI concentration	calculated 2x
TN-22NaI	24	18.796	20.4	$22.2 \approx 22$
TN-28NaI	30	22.999	24.7	$28.2 \approx 28$

The NaI concentration ($NaI_{c(mol\%)}$) was calculated based on the assumption that the weight loss is only attributed to the evaporation of NaI. To examine this assumption, the $NaI_{c(mol\%)}$ is compared with the $NaI_{m(mol\%)}$, whereby the assumption is proven if the calculated and measured NaI concentrations have close values.

The weight loss (W_L) was calculated based on the weight of produced glass (W_G), residual weight in crucible (W_C) and nominal weight of product (15g):

$$W_L = 15 - (W_G + W_C). \qquad\qquad 3.5$$

This weight loss is assumed to be attributed to the evaporation of NaI. The molar concentration of remaining NaI was calculated according to:

$$NaI_{c(mol\%)} = \frac{\frac{W_{NaI}}{M_{NaI}} - \frac{W_L}{M_{NaI}}}{\frac{W_{NaI}}{M_{NaI}} + \frac{W_{Na_2O}}{M_{Na_2O}} + \frac{W_{TeO_2}}{M_{TeO_2}}} * 100\% \qquad 3.6$$

where *W* and *M* refer to the weight and molar mass, the subscriptions indicate the corresponding components.
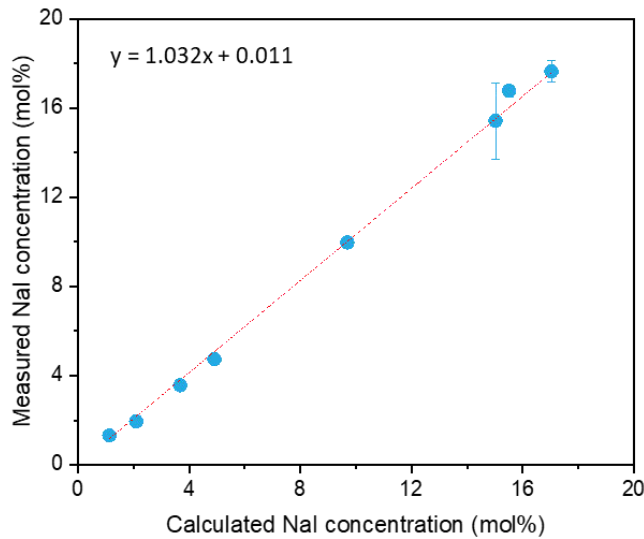
Figure 3-2 The plot of measured NaI concentration (y-axis) against the calculated NaI concentration (x-axis). Linear fitting was performed to demonstrate their linear relationship.

The $NaI_{m(mol\%)}$ and the $NaI_{c(mol\%)}$ were plotted in **Figure 3-2**, a linear fitting was performed to compare their values. A slope of 1.032 ($\approx$1) and an intercept of 0.01 (close to zero) was obtained from linear fitting, which validates the assumption that the weight loss was caused by the evaporation of NaI.

Since the specimens I-22 and I-28 manifest inhomogeneity in composition due to the occurrence of crystals, their compositions were not measured using EPMA. The known relationship of $NaI_{m(mol\%)}$ and $NaI_{c(mol\%)}$ was used to determine the concentration of NaI of I-22 and I-28. This concentration is denoted as corrected NaI concentration, which is obtained via:

$$NaI_{cor(mol\%)} = NaI_{c(mol\%)} * 1.032 + 0.01. \qquad 3.7$$

the factor 1.032 and intercept 0.01 were obtained from the fitting mentioned above.

The EPMA measurements were all performed by Benjamin Wade of Adelaide Microscopic. The real compositions were calculated by Xuanzhao Pan.

3. 2. 3 Polishing

Glass slides with two parallel fine-polished surfaces were prepared for optical and electrical properties characterizations. The bulk glasses were sliced into thin specimens with thickness of 1.5 mm by precision saw (Struers Accutom-100). The polishing was done by the company Jung Precision Optics.

The below details of grinding and polishing procedures were provided by the company. The specimens were bonded onto a 170 mm glass disc with wax. Then the exposed surfaces of the samples were ground with 3 different abrasives, starting with 25 µm diameter Al_2O_3 followed by 15 µm and then 9 µm. The abrasive in powder form was mixed with ethylene glycol instead of water to reduce water absorption of the glasses. The grinding procedure was carried out using a flat iron grinding tool (diameter = 250 mm). After ground, the specimens were finely polished on polyurethane pad using slurry of 0.3 µm Al_2O_3 mixed with ethylene glycol. Once a surface was ground and polished, the specimen was removed from the glass disc, turned upside down and the polished surface was bonded to the glass disc to grind and polish the other surface in the same

way. The specimens with both sides polished were firstly cleaned by Isopar [TM] E (high purity synthetic isoparaffinic hydrocarbon fluid) to remove the wax, following by a final clean with acetone. The fine polished specimens were stored in a desiccator filled with silica-gel desiccant beads.

Xuanzhao Pan cut the bulk glasses into small slides, Danny Jung of Jung Precision Optics polished the specimens.

3. 2. 4 X-ray diffraction

XRD was used to identify the occurrence and type of crystalline phases (Rigaku MiniFlex 600), using a copper Kα radiation (wavelength 1.5418 Å, accelerating voltage 40 kV, and filament current 15 mA). The default widths of incident and receiving Soller slits were set to be 2.5°, and the size of divergence slit was selected to be 1.25°. The widths of scattering slit and receiving slit were all 13 mm. The powder specimens were firstly ground into powder using agate mortar and pestle. The scanning speed was set to be 3° per minute with a stepping size of 0.02°. The crystalline phases were identified by the Rigaku PDXL XRD analysis software and ICDD PDF-2 database.

The XRD measurements were performed and analysed by Xuanzhao Pan.

3. 2. 5 UV-Vis spectroscopy

The optical absorbance spectra in the visible range were measured by a UV-Vis spectrophotometer (Cary 5000, Agilent Technologies). The fine-polished TNN glass slide samples were mounted to an aperture with 5 mm diameter hole which allows the light passing through. The scanning speed and step interval were set as 600 nm/min and 1 nm, respectively. The measured absorbance includes surface absorbance (i.e. no sample thickness dependence) and volume absorbance (i.e. sample thickness dependence), i.e.

$$A_m = A_s + A_v. \qquad\qquad 3.8$$

To obtain the extinction coefficient of a material, i.e. volume absorbance (A_v) normalised by thickness, the surface absorbance (A_s) needs to be subtracted. The surface absorbance comprises Fresnel reflection (A_f) and surface scattering (A_σ, e.g., surface imperfection from polishing), thus,

$$A_m = A_f + A_\sigma + A_v. \qquad\qquad 3.9$$

In this thesis, the Fresnel reflection is considered. The incident light (I_0) is reflected by the entrance surface and the exit surface, then the light reflected at the exit surface is partly reflected back to the entrance surface, and so on. At this condition, the transmitted intensity can be expressed as:

$$T_f = I_0 * \left(\frac{2n}{n^2 + 1}\right). \qquad\qquad 3.10$$

The n is the refractive index of the specimen. Thus, the absorbance due to Fresnel reflection is:

$$A_f = \log_{10}\frac{1}{T_f}. \qquad\qquad 3.11$$

Since the refractive indices of the samples were not measured, the refractive index of the $80TeO_2$-$20Na_2O$ glass (~1.976 at 632.8 nm) was adopted, which is proposed to be close the refractive index of TNN glasses [94]. The A_f calculated using this refractive index represent ~75% of the A_m of X-0 specimen at the corresponding wavelength (632.8 nm).

Surface scattering is caused by surface imperfection such as scratches and surface crystals. The intensity of surface scattering is found to be wavelength independent as supported by the plot (**Figure S. 10**) of a sample with surface crystals (surface scattering). Because TNN glasses show low concentration of volume crystals (and hence low volume scattering, details in section 3. 3. 2), the absorbance at 800 nm is assumed to be caused solely by surface effects (Fresnel reflection and surface scattering). Therefore, the volume absorbance A_v can be approximated as:

$$A_v = A_m - A_{m-800nm} \qquad\qquad 3.12$$

where the $A_{m\text{-}800nm}$ is the absorbance at 800 nm, which is approximated to the Fresnel refraction and surface scattering over the whole wavelength range, i.e., $A_{m-800nm} = (A_f + A_\sigma)$. The extinction coefficient (α) is obtained using:

$$\alpha = \frac{A_v}{d} \qquad\qquad 3.13$$

where d is the thickness of the specimen. The uncertainty of wavelength is estimated to be 2 nm according to the equipment sensitivity [95].

The UV-Vis spectra were collected and processed by Xuanzhao Pan.

3. 2. 6 Experiment and data processing of Raman spectroscopy

3. 2. 6. 1 Experimental method

Raman spectroscopy is a non-destructive structural characterization technique which is based on the inelastic scattering (Raman scattering) of photons. The laser light is scattered when it interacts with a sample. Most of the scattered light is at the same wavelength as the laser light, which is called Rayleigh scattering. But a small amount of light is non-elastic scattered, resulting in scattering light at different wavelengths, which is called Raman scattering, associated with the features (e.g., frequency and intensity) of the vibrations of bond/group. Here, the term "bond" is referred to the connection of elements (e.g., Te-O bonds or Te-BO-Te linkages), while the term "group" is referred to the medium range connection of several structural units (e.g., 4~5 polyhedra).

The Raman spectra were measured by Renishaw inVia™ Raman microscope equipped with a highly sensitive Peltier-cooled charge-coupled device, a motorized *xyz* microscope stage, a 2400 lines/mm diffraction grating, and an 50X magnification lens. The 514.5 nm Ar-ion laser beam (beam diameter=1 μm) with low laser power (0.1 mW/μm^2), which avoids sample damage, was

used as excitation source for the measurements. The spectra were collected at room temperature with a resolution of 2 cm^{-1}. The Raman spectra were acquired under vertical-vertical (VV) polarisation, where both the polarisations of exciting laser beam and scattered light are vertical. The TNN glass specimens were heated up to 170 $^{\circ}$C for the impedance measurements prior to the Raman spectroscopic analysis (detailed in section 3. 2. 8). Right before the Raman measurements, the gold layers on the specimen surfaces were removed by wiping with acetone. Then the specimens were polished using sandpapers with grit sizes of 2000 and 4000 (roughness: 1.5~2 and <0.5 μm), which removes the surface crystallization caused by hydrolysis. Clean and non-crystalline spots were intentionally selected via the optical microscope for the Raman measurements.

3. 2. 6. 2 Data processing

Temperature correction

A temperature correction was performed to remove the impact of temperature on the as-collected Raman spectra. Specifically, the Raman scattering intensity *I(ω)* of a material can be expressed in terms of the densities of states $\rho_b(\omega)$ in different vibrational bonds (subscript *b*) [96-98], i.e.

$$I(\omega) = [n(\omega, T) + 1]\omega^{-1} \sum_b C_b \rho_b(\omega) \qquad 3.14$$

where *ω* is the wavenumber, *T* is the absolute temperature in Kelvin (K), and C_b is a polarization dependent coupling constant. *n(ω,T)* is the Bose-Einstein occupation number represented as:

$$n(\omega, T) = \left[\exp\left(\frac{h\omega}{k_B T}\right) - 1\right]^{-1}. \qquad 3.15$$

As indicated by equation 3.15, the Raman scattering intensity is affected by the temperature. Thus, to produce a Raman spectrum free of spurious feature caused by thermal effect, the as-measured

Raman spectra (I_{mea}) were corrected for temperature and frequency factors to give the temperature corrected Raman spectra (I_{cor}):

$$I_{cor} = \frac{I_{mea}}{\omega\,[n(\omega, T) + 1]}.$$

3.16

Where h and k_B are the Plank and Boltzmann constants, respectively.

Normalization

The fluctuation of laser power, inconsistency of sample alignment, surface roughness and other effects caused experimental uncertainties. Therefore, to quantitatively compare the spectral features of samples, the experimental uncertainties need to be removed via normalization. Since the spectral area represents the sum of Raman scattering vibration, each data point is divided by the area of this spectrum to normalize a spectrum.

Deconvolution

Each Raman spectrum was deconvoluted (using software Fityk) into 8 peaks, which contain structural information of the TNN glasses [54, 86, 99, 100], including 1 Boson peak following log-normal distribution and 7 vibrational peaks following Gaussian distribution. Since the results obtained from auto-fitting depend on the initial parameters, the initial positions of the peaks were selected according to the literature. The full-width-half-maximum (FWHM) and amplitudes of the peaks were manually selected to fit the outlook of spectrum. Finally, an auto-fitting was applied to obtain the optimal parameters.

Raman peak parameters

In this research, the peak positions and peak areas are used to investigate the glass structure of the specimens. The peak position depicts the frequency of the corresponding vibration, which reflects the energy of the vibrating bond/group [101, 102]. The peak area represents the vibration intensity, which indicates the concentration of the corresponding bond/group as defined [101].

Uncertainty estimation

The measurement uncertainty and data processing uncertainty were considered to determine the total uncertainty of the obtained peak parameters. The measurement uncertainty is caused by the variation of environment (e.g., temperature), equipment and the specimen inhomogeneity. The data processing uncertainty originates from the deconvolution of Raman spectrum.

For each specimen, Raman spectra of two spots on each sample were collected for the evaluation of the measurement uncertainty. According to the comparison (**Figure S. 12**), the two Raman spectra of the same sample overlap, which indicates a reliable consistency, i.e., small measurement uncertainty and negligible sample inhomogeneity.

Positions and areas of deconvoluted peaks were used for discussion. Evaluating the uncertainties (or errors) of deconvoluted peaks encountered difficulty, since the parameters of deconvoluted peaks are not independent, e.g., changing the position of a peak can result in the changes of all peak positions. Furthermore, the mathematical deconvolution of a Raman spectrum can generate infinite solutions, but only a few of them presents meaningful structural information. Therefore, the uncertainties presented in this thesis were obtained based on estimation. Specifically, the uncertainty of peak position was approximated to be the resolution of the Raman spectrometer, which is 1 cm^{-1}. The uncertainty of the peak area was estimated according to the area difference between collected spectrum and the sum of deconvoluted peaks (in %):

$$ERR_{peak\ area} = \frac{|Area_{spectrum} - Area_{peak\ sum}|}{Area_{spectrum}} * 100\%. \qquad 3.17$$

*The Raman spectra were collected by Benzine Omar of the Friedrich-Schiller-Universität Jena. The data processing was performed by Xuanzhao Pan.

3. 2. 7 Density measurement and data processing

3. 2. 7. 1 Density measurement

The densities were measured by Archimedes method using A&D GX-1000 precision weighing balance. Since the TNN glass specimens are hygroscopic, 1,2-propanediol solvent (Sigma Aldrich, 99.5%), whose density is 1.036 g/cm^3, was used instead of water for the density measurements. The density is calculated according to the Archimedes theory as detailed below. The buoyancy is expressed as:

$$F = \rho_L * V * g \qquad\qquad 3.18$$

where ρ_L, V and g are the density and volume of liquid, and the gravitational acceleration, respectively. The gravity of a sample in air is expressed as:

$$G_{air} = \rho * V * g = m_a * g \qquad\qquad 3.19$$

where m_a is the mass measured in air, and ρ is the density of sample.

The gravity of sample in liquid is expressed as:

$$G_{liquid} = (\rho - \rho_L) * V * g = m_b * g \qquad\qquad 3.20$$

where m_b is the mass measured in liquid.

Since:

$$m_a = \rho * V \qquad\qquad 3.21$$

thus:

$$V = \frac{m_a}{\rho}. \qquad\qquad 3.22$$

According to equation (3.20) and (3.22), we have:

$$m_b = \frac{m_a}{\rho}(\rho - \rho_L). \qquad\qquad 3.23$$

Thus:

$$\rho = \frac{m_a}{m_a - m_b} * \rho_L. \qquad\qquad 3.24$$

The measurement uncertainty of density was approximated to be the standard deviation of 5 measurements.

3. 2. 7. 2 Calculation of molar mass, molar volume and molar free volume

The molar mass, molar volume, number density and free volume are calculated from the measured density data to extract more information of the specimens. Considering the glass system can be regarded as a mixture of serval compounds, the molar mass, M, can be calculated according to [103]

$$M = \sum M_i * x_i \qquad\qquad 3.25$$

where M_i and x_i are the molar mass and molar ratio of each component (i.e., TeO_2, Na_2O, NaX), respectively. The molar volume, V, can be calculated according to,

$$V = \frac{M}{\rho} \qquad\qquad 3.26$$

where ρ is the density of the specimen.

In order to estimate the space for ion migration, the total free molar volume is calculated based on the compositions and densities [104]. The molar free volume, V_{free}, is approximated as the molar volume subtracting the molar hard-sphere volume:

$$V_{free} = V - V_{hard-sphere}. \qquad\qquad 3.27$$

The molar hard-sphere volume is the volume of all ions approximated as hard sphere without any vibration:

$$V_{hard-sphere} = \sum A_i * \frac{4\pi}{3} * r_i{}^3 * N_A \qquad \text{3.28}$$

where A_i is the atomic ratio and r_i (specified in this thesis) is to the ionic radii of the elements (i.e. Te, Na, O and halide), respectively. Combining equations 3.26 and 3.28 yields the molar free volume as:

$$V_{free} = \frac{\sum M_i * x_i}{\rho} - \sum A_i * \frac{4\pi}{3} * r_i{}^3 * N_A. \qquad \text{3.29}$$

The uncertainty propagation of function $f = \frac{A}{B}$ is $\sigma = |f|\sqrt{(\frac{\sigma_A}{A})^2 + (\frac{\sigma_B}{B})^2}$, where σ_A and σ_B are the error of factors A and B, respectively [105, 106]. Therefore, the uncertainty of the molar volume can be estimated using the uncertainty of density as:

$$\sigma_V = V * \frac{\sigma_\rho}{\rho} \qquad \text{3.30}$$

where σ_ρ is the uncertainty of density.

The uncertainty of the molar free volumes was estimated as:

$$\sigma_{V_{free}} = V_{free} * \frac{\sigma_V}{V}. \qquad \text{3.31}$$

The densities were collected and processed by Xuanzhao Pan.

3. 2. 8 Impedance spectroscopy

3. 2. 8. 1 Concepts and definitions

The electric properties were analysed by the impedance spectroscopy (IS), which is a non-destructive method used to characterize the electric properties (e.g. conductivity) of thin layers, bulk, surfaces (interfaces) and films [107]. In this study, the parallel plates method, which sandwiches a bulk specimen between two electrodes for measurement, was used to measure the ionic

conductivity of the TNN glasses [108]. A detailed introduction of the theory of IS is presented in supplementary B2. 4.

The symbols, terminologies, and definitions of parameters that are related to IS are given below [109]. The parameters used in this thesis are highlighted by underlines.

<u>Z</u>: impedance, is the measure of the opposition that a circuit presents to a current when a voltage is applied. It is presented as complex impedance function of frequency in IS, i.e., $Z^*(\omega)$.

<u>ε: dielectric constant / dielectric permittivity</u> (or in complex form ε^*), is a measure of electric polarizability of a material in response to an electric field with frequency from $\sim 10^{-1}$ to $\sim 10^9$ Hz. ε_0 is the dielectric permittivity of free space, $= 8.854 * 10^{-12}$ F/m.

M: modulus function / complex electric modulus (M^*), is defined as the inverse of complex relative permittivity (ε).

Y: admittance / complex admittance (Y^*), is a measure of how easily a circuit or device will allow a current to flow. It can be obtained from the reciprocal of impedance.

<u>C_c</u>: is the capacitance of the empty cell with electrode area A and electrode separation length l (these A and l are also the area and length of specimens). C_c is a constant for each sample, independent of compositions, just depends on the geometry of the specimen.

<u>C</u>: capacitance, is the ratio of electric charge stored in a conductive system over the electric potential.

<u>R</u>: resistance, is a measure of the opposition to the flow of electric current. In circuit, the R is referred to a resistor element in the circuit.

<u>L</u>: inductance, describes the tendency of an electrical conductor to oppose a change in the electric current through it. It is presented as inductor element in circuit.

CPE: constant phase element, is an empirical circuit element that models the behaviour of an imperfect capacitor. It replaces the capacitor in the equivalent circuit to represent the non-ideal electrode, for example, the electrode with rough or porous surfaces.

l/A: length / area, called geometry factor, is used for calculation of conductivity.

σ: conductivity, is a measure of the material ability of conducting electricity.

τ: time constant, is the time required to charge or discharge the capacitor.

E_a: activation energy, specifically referred to the activation energy for conduction in the IS measurement. The activation energy of an ionic conducting process includes i) the energy of deforming the structure to pass an ion, and ii) the energy of migrating the ion.

3. 2. 8. 2 System configuration and sample preparation

The IS of $68TeO_2$-$(32-x)Na_2O$-$x(NaX)_2$ glasses was measured by the Novocontrol Alpha-A analyser paired with a Novotherm temperature control system to study the electrical property. Such equipment enables the impedance range across 18 orders (10^{-3} to 10^{15} Ω) and the ultra-wide capacity range (10^{-15} to 1 F). The frequency of 10^{-1} to 10^7 Hz was applied to measure the impedance spectra of specimens, i.e., including DC conduction [110, 111].

Before being measured, the two parallel surfaces of a glass slide (thickness ~1.5 mm) were finely polished to reduce the surface roughness (polishing section 3. 2. 3), for a good contact between the glass surfaces and copper plates. When an electric field is applied to an ionic conductive glass, an unwanted effect called "electrode polarization" occurs. This effect arises from the building up of ions close to electrodes, which generates a large capacitance to the measured impedance. To minimize the build-up of ions near surfaces, a 10 nm gold layer was thus coated on both surfaces

as blocking electrode [112, 113]. This gold layer coating also improves the electrode-sample contact. This as-prepared specimen was placed between two copper plates. The temperature of the sample cell was ramped from room temperature up to 50 ºC, 80 ºC, 110 ºC, 140 ºC and 170 ºC, respectively.

3. 2. 8. 3 Impedance spectroscopy data processing procedure

Figure 3-3 shows a flow diagram of the general characterization procedure using IS [107, 111]. The measured complex impedance data $Z_{exp}^{*}(\omega)$ comprises real part $Z_{exp}'(\omega)$ and imaginary part $Z_{exp}''(\omega)$. The electrical properties (or behaviours) of TNN glasses were analysed by two steps (with details discussed in section 3. 2. 1):

1) First, the experimental data were fitted by an *empirical equivalent circuit* according to the shape of the impedance spectrum. From such fitting, the equivalent circuit impedance $Z_{eq}^{*}(\omega)$ and electrical parameters (e.g. resistance and capacitance) of the equivalent circuit were obtained.

2) Second, a *mathematical model* was proposed based on the macro-structure of the specimen, and then the conductivity and activation energy were calculated according to such model.

The uncertainty of IS measurement results from the equipment, sample inhomogeneity and data processing. The measurement uncertainty was estimated to be about 2.1% according to reference [114], which includes the uncertainty caused by the equipment and sample mounting. Though repeated measurements on each sample enables to estimate the measurement uncertainty, this is not performed because the surface condition can be already different before and after measurement due to hygroscopic TNN glasses (SEM image, **Figure 3-20**).

The data processing uncertainty was evaluated based on the difference between experimental data $Z_{exp}^{*}(\omega)$ and fitting data $Z_{eq}^{*}(\omega)$, i.e.

$$Error_{impedance} = \sqrt{(\frac{|Z'_{exp} - Z'_{eq}|}{Z'_{exp}})^2 + (\frac{|Z''_{exp} - Z''_{eq}|}{Z''_{exp}})^2} * 100\%. \qquad 3.32$$
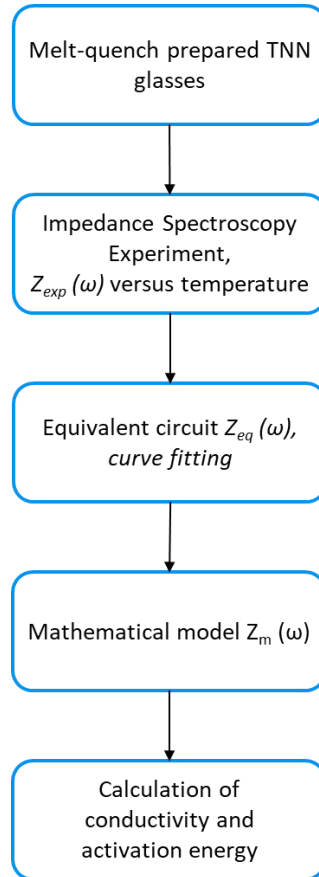
Figure 3-3 The general characterization procedure using impedance spectroscopy.

The Impedance spectra were collected by Xuanzhao Pan at the Friedrich-Schiller-Universität Jena. Yang Xia offered training and raised advises of measurements. The data processing was performed by Xuanzhao Pan.

3. 2. 9 Scanning electron microscope (SEM)

SEM (FEI Quanta 450 FEG environmental SEM) was applied to image the fresh cross-sections, the hydrolysed surfaces, and the exposed-heated surfaces of specimens. Both Everhart-Thornley Detector (ETD) and Backscattered Electron Detector (BSED) were used for the observation. The EDX detector (Oxford-Ultim-Max large area SDD EDX detector) was used to analyse the elemental ratio of specimens.

The fresh cross-sections were prepared by cleavage right before the SEM characterization to prevent the surface hydrolysis. The cleaved fresh cross-sections were immediately coated by 10 nm platinum layers to ensure effective surface conductivity for SEM imaging. The as-coated specimens were instantly placed into the SEM chamber followed by evacuation. During the entire procedure, the fresh cross-sections were only exposed to ambient atmosphere for approximately 5 mins in total. These fresh cross-sections are regarded to reflect the volume crystallization condition of the specimens.

To measure the thickness of a hydrolysed surface, the worst scenario of fully hydrolysed surface was prepared by wiping the surface with water-wet tissue. Only one wipe was applied on each surface to avoid over hydrolysis. The thickness of the hydrolysed surface was used to estimate the volume ratio of crystallized surface (detail in section 3. 3. 5).

The surface condition of specimens after impedance measurements is mimicked at below. The platinum-coated cleaved specimens were stored in a desiccator for approximately 1 month, which is similar to the condition of the specimens before the impedance measurement. The hydrolysis condition of cleaved surfaces is regarded as similar to that of the fine-polished surfaces. The exposed specimens were heated in an annealing furnace from room temperature to 50 ℃, 80 ℃,

110 ºC, 140 ºC and 170 ºC gradually with a ramp-up rate of 10 ºC/min and dwelled for 5 mins at each temperature, to simulate the thermal history of impedance measurement.

Ken Neubauer of Adelaide Microscopic performed the Pt coating on specimens. The SEM images were collected by Xuanzhao Pan.

3. 3 Measurement results and discussion

3. 3. 1 Glass forming

Selection of base composition and crucible

Na_2O plays a role as network modifier in TeO_2-Na_2O glass (TN), which decreases the glass transition temperature and strengthens the crystallization tendency [115]. A certain part of Na^+ introduced to the glass system is weakly linked to non-bridging oxygen, while the rest exists as mobile Na^+ ions (MNIs) [116]. Those MNIs act as charge carriers for conduction. Since the concentration of MNIs is associated with the total amount of Na^+ ions, a higher Na^+ ion concentration facilitates a higher conductivity. However, crystals are formed if excessive amount of sodium is added. The crystallization should be avoided or minimized to achieve transparent samples. Therefore, an experiment was performed to identify the maximum concentration of Na_2O in TeO_2-Na_2O glass system without crystallization.

As indicated by **Figure 3-4 a**, the specimen with 32% of Na_2O is transparent while that with 35% Na_2O shows obvious crystallization. XRD measurements confirm the amorphous structure of $68TeO_2$-$32Na_2O$ glass (**Figure 3-5**) and the crystallization of $65TeO_2$-$35Na_2O$ glass (**Figure 3-6 a**). The crystals in $65TeO_2$-$35Na_2O$ were identified as paratellurite and Na_2TeO_3 according to the peak assignments. According to these analyses, the maximum concentration without crystallization of Na_2O in TeO_2-Na_2O was defined to be 32 to 34 mol%, which agrees with the

result (i.e. 33 mol%) published in elsewhere [115]. Thus, $68TeO_2$-$32Na_2O$ (X-0) was selected as the base composition for the preparation of TN-Cl, TN-Br and TN-I glasses.

Figure 3-4 The digital photos of TNN glasses with different compositions prepared in ceramic or gold crucible, indicating the transparency and crystallization. a) $68TeO_2$-$32Na_2O$ and $65TeO_2$-$35Na_2O$ glasses prepared using ceramic or gold crucible. b) TN-Cl, TN-Br and TN-I glasses with different concentration of sodium-halide and prepared in different crucibles. The red frames highlight the specimens that start to show crystallization. Note, 1) the photos were taken in front of a black background and white light source shining

from above; 2) only a few photos of specimens prepared in gold crucible were presented, which are used to show the colouration caused by using gold crucible; 3) the lines shown on the I-19 (ceramic crucible) are the surface cracks; 4) the opaqueness of sample Cl-12 (gold crucible) is attributed to the hydrolyzation of the surface and a few crystallized spots in the centre of the sample.

The crucibles used for melting can impact the optical property of glasses including TeO_2-based glasses [117-122], because the corrosive TeO_2-based glass melts dissolve crucible material [120]. Therefore, different crucible materials (platinum, gold and ceramic) are compared to select the suitable crucible for preparation. When melting TeO_2-based glasses (e.g. TeO_2-PbCl [121], TeO_2-WO_3 [123] and TeO_2-ZnO-Na_2O [124]) in platinum (Pt) crucible, the dissolved platinum is existing in the form of Pt^{2+} or Pt^{4+}, i.e. Pt^0 in the crucible is transformed to Pt^{2+} and Pt^{4+} in the glasses, causing yellow colour. Melting TeO_2-based glasses (e.g. TeO_2-ZnO-Na_2O [125]) in gold (Au) crucible also causes the dissolution of crucible and introduces ionic Au to the glass system. The ionic Au does not shows absorption or scattering in the visible range (380 to 700 nm) [125], thus does not deteriorate the optical transparency. The TeO_2-based glass melt also dissolves the ceramic crucible (about 4 mol% of Al^{3+}, section B 2.6), but the Al^{3+} does not manifest absorption in the visible range (380 to 700 nm) [126]. Therefore, the Au and ceramic crucibles were selected as melting crucibles in this research. The X-0 glasses melted in ceramic crucible and in gold crucible are all colourless and transparent (**Figure 3-4 a**).

Identifying the glass forming regions of TN-Cl, TN-Br and TN-I glasses

TN-Cl, TN-Br and TN-I glasses were prepared via substituting one Na_2O of $68Te_2O$-$32Na_2O$ (X-0) by two NaX (X=Cl, Br and I), resulting in $68TeO_2$-$(32-x)Na_2O$-$x(NaX)_2$. The glass forming regions with no discernible crystals were defined according to the digital photos and XRD analysis.

76

Figure 3-4 b shows photos of TN-X glasses with various NaX concentration prepared in ceramic crucible or gold crucible.

The specimens prepared in a ceramic crucible are transparent and colourless, while those prepared in a gold crucible (Cl-10, Cl-12, Br-14, I-4) show brown colour (**Figure 3-4**). Since the halide ions act as reducing agents (ability to donate electrons: $I^- > Br^- > Cl^-$ [127]), the ionic Au in TN-X glasses are reduced to Au nanoparticles that cause the colouration of glasses. The colour is depending on the type and concentration of halide, i.e., a stronger reducing agent and higher concentration of halide cause a deeper colouration. Sample Br-14 prepared in a gold crucible shows deep brown colour, since Br^- is a strong reducing agent. Therefore, the TN-X glasses with 2x higher than 14 have not been prepared in gold crucible.

For the TN-Cl glass system, no crystallization is found in the sample prepared with the concentration of (NaCl)$_2$ below 11 (**Figure 3-4 b**). Crystals are observed in the specimen C-12, while specimen C-16 is highly crystallized. Therefore, the glass forming region of TN-Cl system is defined as $2x < 12$. For TN-Br and TN-I glass systems, no discernible crystal is observed in specimens with 2x below 22. When the concentration of NaX increasing to $2x = 22$, crystals are observed in specimens Br-22 and I-22. This means, the glass forming regions for the TN-Br and TN-I systems are all determined as $2x < 22$.
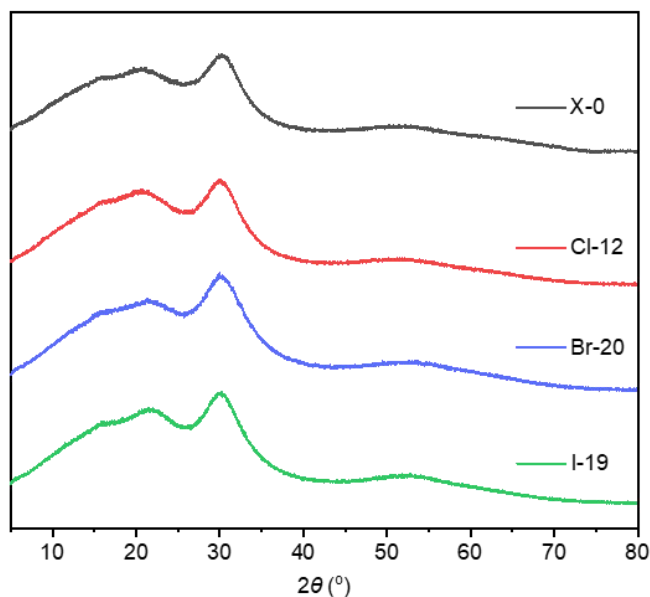
Figure 3-5 The powder-XRD spectra of X-0, Cl-10, Br-20 and I-19 glasses, whose compositions are at the edge of defined non-crystallized regions. The spectra show no crystalline pattern but just two broad humps at about 20° and 30°, which corresponds to the XRD of substrate and TNN glass, respectively.

No crystalline pattern is observed in the powder-XRD spectra of X-0, Cl-10, Br-20 and I-19 glasses (**Figure 3-5**), indicating they are XRD amorphous (crystal concentration < 4 vol% [128]). The broad hump at ~20° corresponds to the diffraction of the silicate glass substrate used as sample holder, since the identical broad hump is observed in the XRD spectrum of the empty substrate (**Figure S. 17**). The diffraction of amorphous TNN glass generates the narrow hump at about 30°, which has also been detected in other TeO_2-based glasses (e.g. TeO_2-ZnO-Na_2O [129, 130]). According to the above powder-XRD measurements, the TNN glasses with NaX concentration within the identified regions (i.e. $2x = 0$~10 for NaCl, 0~20 for NaBr, or 0~19 for NaI) are inferred to be amorphous.
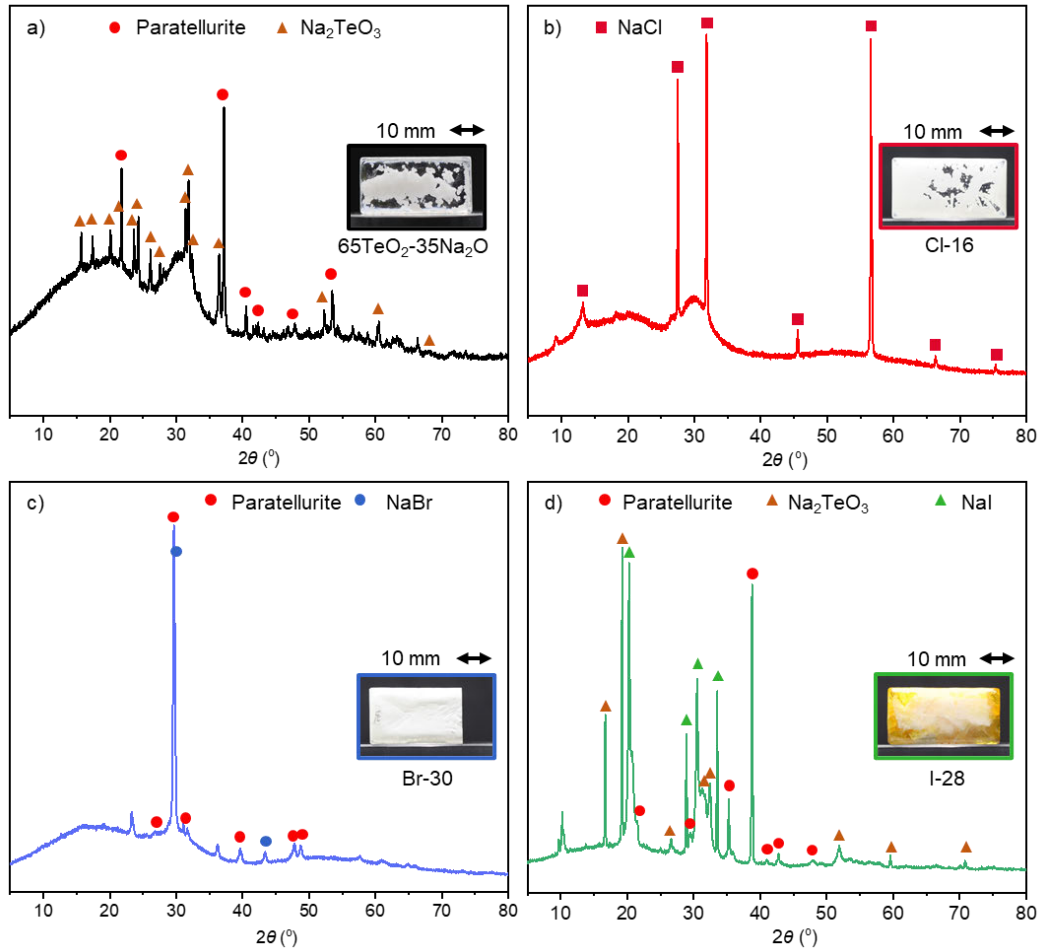
Figure 3-6 The bulk-XRD spectra of highly crystallized glasses, i.e. a) $65TeO_2$-$35Na_2O$, b) Cl-16, c) Br-30 and d) I-28, with peaks identification. The insert photos, which have also been presented in figure 3-4, indicate the appearances of specimens being measured.

The glass forming regions suggest that less NaCl can be introduced to TN-X glass system compared to NaBr and NaI. The cause of this phenomenon is not understood yet. As indicated by the XRD results (**Figure 3-6**), NaX, α-TeO_2 (paratellurite), and Na_2TeO_3 crystals appear in TN-X glasses. I hypothesize, the formation of NaX crystals is related to their solubility in TNN glasses, while the crystallization of α-TeO_2 and Na_2TeO_3 is due to the change of viscosity. NaX precipitates as crystals once their addition exceeding the solubility in TN-X glasses. The glass forming regions suggest that the solubilities of NaBr and NaI are higher than that of NaCl in TN-X glass system.

Since the NaX plays the role as glass modifier, the increase of NaX decreases the melting temperature and viscosity. A lower viscosity enhances the diffusion of atoms and enhances the crystallization tendency [131]. Therefore, the narrower glass forming region of TN-Cl (compared to TN-Br and TN-I) suggests the NaCl reduces viscosity to a higher degree than NaBr and NaI.

As 2x increases to 28~30, crystals are observed in the specimens Br-30 and I-28 (**Figure 3-4**). Since the glass around the top-fire-polished surface was not in contact with the mould, this glass region cooled slower, facilitating crystal formation in this region. (**Figure S. 18**). The XRD spectra of $65TeO_2$-$35Na_2O$, Cl-16, Br-30 and I-28 bulk glasses are shown in **Figure 3-6**, with **Table 3-5** summarizing the crystals formed in these glasses. Specifically, the crystals in $65TeO_2$-$35Na_2O$ are identified as paratellurite and Na_2TeO_3, while NaCl, NaBr and NaI crystals are precipitated in Cl-16, Br-30 and I-28 glasses, respectively, suggesting the additions of NaX are above the solubilities. Paratellurite crystals are formed in both Br-30 and I-28 glasses, while Na_2TeO_3 crystals are only detected in I-28 glass. The formation of different TeO_2-based crystal species is not understood, which remains to be further investigated. Since the NBOs interrupt the continued TeO_2 network, which subsequently suppresses the formation of TeO_2-based crystals, I hypothesize, the TeO_2-based crystal species are formed due to the insufficient amount of non-bridging oxygens as a result of the reduced amount of glass network modifier (e.g., Na_2O) addition [132].

Table 3-5 A summary of crystallized species in $65TeO_2$-$35Na_2O$, Cl-16, Br-30 and I-28. The delta "Δ" is referred to differences of measured specimens 2x compared to the corresponding maximum NaX concentrations of amorphous glasses.

	$65TeO_2$-$35Na_2O$	TN-16NaCl	TN-30NaBr	TN-28NaI
Crystal	Paratellurite Na_2TeO_3	NaCl	NaBr Paratellurite	NaI Paratellurite Na_2TeO_3

3. 3. 2 Optical extinction coefficients

The calculated extinction coefficients of TNN glasses are shown in **Figure 3-7**. Most of the TNN glasses manifest extinction coefficients < 0.005 cm^{-1} at 400 to 700 nm, which agrees with the transparent and colourless appearance (section 3. 3. 1). The extinction coefficients in the visible range show no correlation with the concentration of NaX. Some specimens exhibit extinction coefficients > 0.005 cm^{-1} in the visible range, which can be attributed to the formation of Au particles (for X-0 and Cl-12 prepared in gold crucible) or the red-shift of the cut-off wavelength (for I-17~22, below discussion).

The extinction coefficients increase at the low wavelength region (**Figure 3-7 a~c**). The cut-off wavelength of a glass is the lowest wavelength of light that can be transmitted through the glass, which means, the light with wavelength below the cut-off wavelength is mostly absorbed by the glass. In this thesis, the wavelength with extinction coefficient of 0.3 mm^{-1} is defined as the cut-off wavelength. **Figure 3-7 d** shows the cut-off wavelength plotted versus 2x of TNN glasses prepared in a ceramic crucible. The TN-Cl glasses have the same cut-off wavelength, and this cut-off wavelength is identical to that of X-0 glass. TN-Br glasses with concentration of NaBr higher than 2x = 12 show red-shift cut-off wavelength compared to those with lower NaBr concentration (**Figure 3-7 b and d**).

The cut-off wavelength of TN-I glasses is red-shift as the NaI concentration increases (**Figure 3-7 d**). This red shift of the cut-off wavelength agrees with the observation of yellow-orange colour of TN-I glasses (section 3. 3. 1, **Figure 3-4**). Since the cut-off wavelength is correlated to the bandgap (i.e. separation between valence and conduction bands) of a substance [133], the red shift of the UV edge implies that the bandgap of TN-I glass is decreased as the concentration of NaI increases.
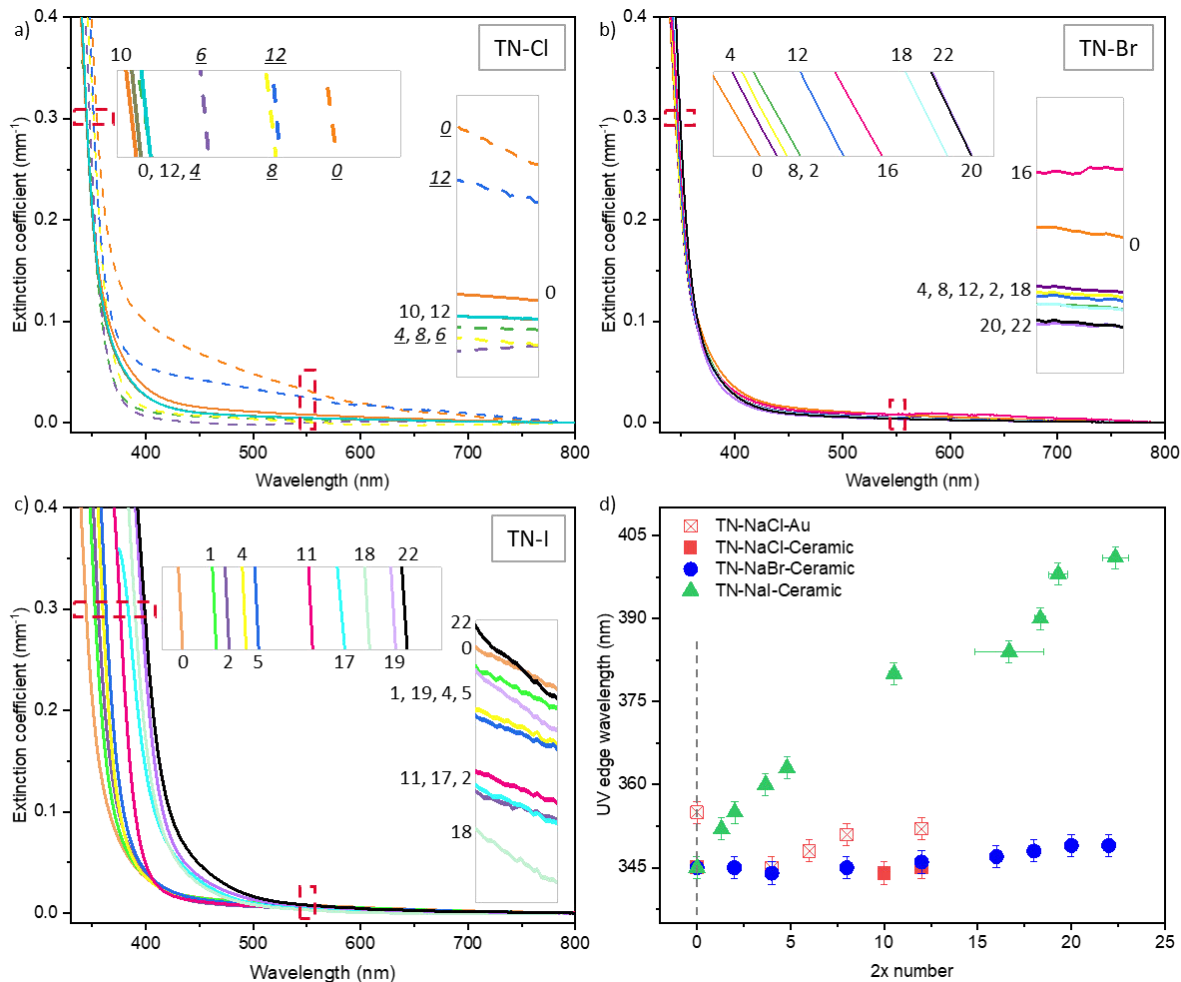
Figure 3-7 The extinction coefficients of a) TN-Cl, b) TN-Br and c) TN-I systems. d) The plot of cut-off wavelength against 2x of the TN-X glass systems. The insert graphs at a), b) and c) show the UV-Vis spectra at 0.29~0.31 mm^{-1} extinction coefficient (horizontal axes) and at 549~551 nm wavelength (vertical axes), respectively.

3. 3. 3 Glass-structure

3. 3. 3. 1 Schematic illustration of polyhedra in TeO$_2$-Na$_2$O-NaX glasses

The polyhedra in TeO$_2$-Na$_2$O-NaX glasses are schematically shown in **Figure 3-8**. Here, the elements are presented by circles with diameters proportional to the effective ionic diameters of corresponding elements [84]. The bonds are schematically indicated by lines with lengths proportional to the bond lengths in polyhedra (introduction 1. 1) [134-137].

82
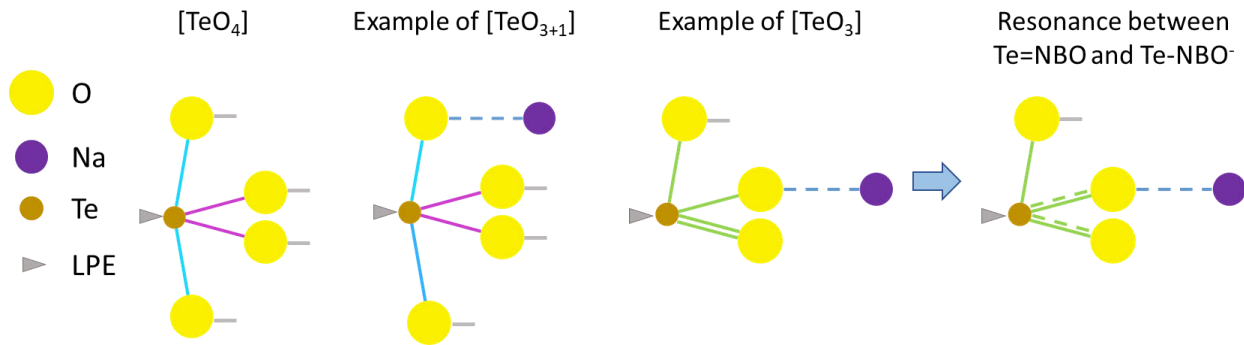
Figure 3-8 The schematic examples of tellurium-oxide polyhedra in TeO_2-Na_2O based glasses.

Tellurium and oxygen in TeO_2-based glasses exist as Te^{4+} with coordination number (CN) = 4, 3+1 or 3 and O^{2-} with CN = 2 [134], respectively. Thus, the diameters of Te and O ions in the TNN glasses are approximated as the effective ionic sizes of Te^{4+} (CN = 4) and O^{2-} (CN = 2). The TeO_2-based glasses network is constructed by $[TeO_4]$, $[TeO_{3+1}]$ and $[TeO_3]$ polyhedra. The structural characteristics of these polyhedra are summarized as [86]:

1) Oxygen participating in the TeO_2 glass network can be presented as bridging oxygen (BO) or non-bridging oxygen (NBO). BO is the oxygen that connects to two Te with forming a Te-BO-Te linkage, while NBO connects to one Te to form Te-NBO bond. The Te-NBO bond is defined to be single-bond NBO (denoted as Te-NBO⁻) or the terminal NBO (denoted as Te=NBO).

2) The $[TeO_4]$ is a one-sided trigonal bipyramid polyhedron with an LPE. It consists of two long Te-$_{ax}$O bonds (length ≈ 210 pm) in the axial direction, and two short Te-$_{eq}$O bonds (length ≈ 190 pm) in the equatorial direction [134].

3) The $[TeO_{3+1}]$ is a distorted trigonal bipyramid polyhedron with one axial bond being stretched. The three non-stretched bonds have length similar to those in $[TeO_4]$ polyhedron, while the length of the stretched axial bond is 240 pm.

4) The [TeO$_3$] trigonal pyramid polyhedron is formed when one axial bond of [TeO$_{3+1}$] is cleaved. There are two types of [TeO$_3$], isolated [TeO$_3$] and terminal [TeO$_3$] [138] (**Figure 3-8** shows an example of terminal [TeO$_3$]). The isolated [TeO$_3$] is not connected to any tellurium, which means being isolated from the network. The terminal [TeO$_3$] is connected to one tellurium, it is the terminal of the network. The isolated [TeO$_3$] has two single-bond NBO and one terminal NBO, while the terminal [TeO$_3$] has one single-bond NBO, one terminal NBO and one BO. The Te-NBO$^-$ and Te=NBO formed in [TeO$_3$] polyhedra are resonating, which means these NBOs are regarded as identical [86], thus the Te=NBO and Te-NBO$^-$ are equivalent with a length of 185 pm.

5) As mentioned in section 3. 1. 1, the Na$^+$ ions in the TNN glass system can weakly bond to the non-bridging oxygens or exist as mobile ions.

The nomenclature of polyhedra follows consistent rules. The symbols dash " - ", equal " = " and colon " : " illustrate the type of bonds between elements, specifically, " - " stands for the single bond between Te and O, while " = " denote the double bond between Te and O, the " : " is specifically referred to the weak bonding between -NBO$^-$ and Na$^+$ ion. Bridging oxygen is denoted as "-BO-", while the single-bond NBO and terminal NBO are respectively marked as "-NBO$^-$" and "=NBO". In some cases of the discussion, the non-bridging oxygen is generally referred to as "-NBO". Subscript numerals (i.e. 4, 3+1, 3) following O or Te are referred to the CN of tellurium. The direction of bond is depicted by subscript "ax" or "eq" as representing axial or equatorial, respectively. If no subscript added, the CN or bond direction is not specifically assigned. For instance, Te$_{3+1}$-$_{ax}$NBO:Na refers to the bond between tellurium (CN = 3+1) and single-bond NBO at axial direction, and this single-bond NBO is weakly linked to a Na$^+$ ion.

This schematic follows several principles:

1) The -NBO$^-$ only exist in [TeO$_{3+1}$] and [TeO$_3$] polyhedra.

2) The -NBO⁻ must link to one Na⁺ ion forming weak -NBO:Na bond.

2) -NBO⁻ occurs in axial and equatorial directions, the schematics only present a few examples.

4) [TeO$_3$] has one Te=NBO, and Te=NBO is only presented in [TeO$_3$] [139].

3. 3. 3. 2 Raman spectra of TeO₂-Na₂O glass: peak identification and interpretation

The Raman spectrum of X-0 glass is used as an example for the peak assignments. The impact of halides on the glass-structure is identified via the change of the tellurium-oxygen network. The peak identification and interpretation of TeO$_2$-Na$_2$O were adopted from the previous published literature (mainly from Takao Sekiya etc) [54, 86, 99, 100, 140-142].

The Raman spectrum of X-0 glass with 8 deconvoluted peaks is presented in **Figure 3-9**. The insert schematic diagram illustrates the examples of vibrations corresponding to the deconvoluted peaks. All peaks position assignments and structural characteristics are summarised in **Table 3-6**.

1) Peak A (at ~780 cm^{-1}) and peak B (at ~725 cm^{-1}) are attributed to the stretching vibrations of the Te and NBO (Te=NBO and Te-NBO⁻) in [TeO$_{3+1}$] and [TeO$_3$], respectively [86]. The frequencies of these stretching vibrations of Te and NBO do not depend on the coordination number of tellurium, but on the surroundings of the NBOs. Specifically, for the case of Peak A, the NBO has no interaction with the adjacent Te (of another polyhedron), while for peak B, the NBO interacts with adjacent Te, leading to a weakening of the Te-O vibration and hence a red shift of peak B compared to peak A. For the convenience of discussion, in some cases, the Te-NBO bond depicted by peak A is marked as Te-NBO$_A$, while that by peak B is noticed as Te-NBO$_B$.

2) Peak C at about 670 cm^{-1} is attributed to the asymmetric vibrations of Te-BO-Te linkages constructed by inequivalent bonds from the [TeO$_{3+1}$] and [TeO$_4$] polyhedra (e.g. Te$_{4-eq}$BO$_{ax}$-Te$_{3+1}$, Te$_{4-eq}$BO$_{ax}$-Te$_4$, or Te$_{4-ax}$BO$_{eq}$-Te$_{3+1}$) [86].

3) Peak D at ~600 cm^{-1} is assigned to the anti-symmetric stretching of Te-BO-Te linkage composed of TeO$_4$ polyhedra [86, 142].

4) Peak E at ~475 cm^{-1} reflects the symmetric stretching and bending vibrations of Te-BO-Te linkages consisting of vertex-sharing [TeO$_4$], [TeO$_{3+1}$] and [TeO$_3$] polyhedra [86]. The area of this peak is determined by the concentration of vertex-sharing polyhedra, thus it can be an indicator of the network continuity.

5) Peak F at ~275 cm^{-1} originates from the bending vibration of [TeO$_3$] polyhedra with NBOs [86]. E. I. Kamitsos et. al. investigated the far-infrared absorbance spectra of different glass systems (including TeO$_2$-based), and discovered that the peak at ~300 cm^{-1} is related to the motion of alkali ions (i.e., Li$^+$ and Na$^+$), therefore, they suggest the Raman peak at ~300 cm^{-1} is also related to the motion of Na$^+$ [143, 144]. However, due to the lack of information, the [TeO$_3$] polyhedra vibration and Na$^+$ motion cannot be resolved in this peak.

6) Peak G observed at ~130 cm^{-1} is generated by the intra-molecular asymmetric motion of tellurium-oxygen bonds [54, 141, 145, 146]. Due to the lack of interpretation on this peak, which overlaps with the well pronounced Boson peak [146], the discussion of peak G is not presented below.

7) The peak at ~40 cm^{-1} is referred to as Boson peak [147], which depicts the medium-range structure (i.e. several coordinating spheres [148]) of glass systems [100]. Hiroshi Shintani etc. performed a modelling study to correlate the Boson peak and the mechanical properties (shear modulus and fragility) of glass system [149]. The Boson peak position shift towards lower frequency (red-shift of wavelength) indicates a decrease of shear modulus and an increase of fragility. It is important to note that, the interpretation of the Boson peak is still under debate and remains to be progressed [149].
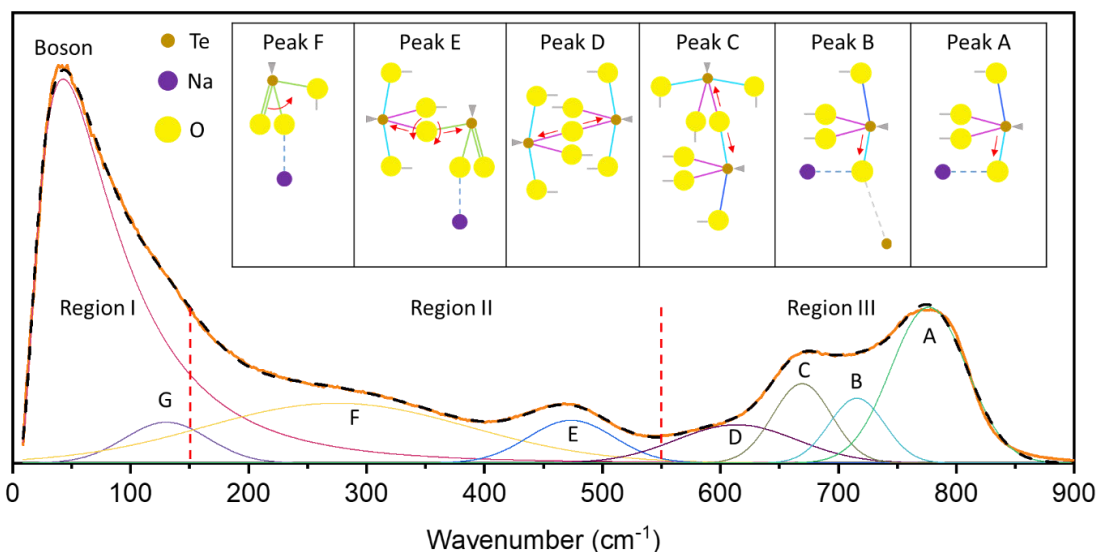
Figure 3-9 The deconvoluted Raman spectrum of X-0 glass. The sum of all deconvoluted peaks (black-dash curve) is highly overlapping with the original Raman spectra (orange curve), indicating the high reliability of the deconvolution method. The insert schematic shows examples of polyhedra vibrations constructing the corresponding Raman peaks, bending vibration is indicated by arc while straight line showing the stretching vibration. The red-dash lines indicate different regions of the Raman spectrum.

The Raman spectra of TNN glasses can be divided into 3 regions based on the corresponding vibrations. The first region at 0 to ~150 cm^{-1} is dominated by the Boson peak (**Figure 3-9** and **Table 3-6**), which indicates the medium-range structure of glasses. The second region from 150~550 cm^{-1} is mainly composed of peaks E and F, which represent the bending vibrations of bonds with NBOs or BOs, respectively. Peaks A-D appearing at the last region (550~900 cm^{-1}) correspond to the stretching vibrations of bonds with BOs or NBOs. In this research, the variations of peak positions and peak areas are discussed to uncover the change of structure. Generally (except for peak G), the peak position is related to the bond (or linkage) length and the peak area depicts the concentration of the corresponding bond (linkage).

Table 3-6 Summary of the peak assignments and their characteristics.

Peak	Position (cm^{-1})	Structural characteristic
A	~780	Stretching vibration of Te-NBO$_A$, where NBO$_A$ does not interact with the adjacent Te (of another polyhedron)
B	~725	Stretching vibration of Te-NBO$_B$, where NBO$_B$ interacts with the adjacent Te (of another polyhedron)
C	~670	Anti-symmetric vibrations of inequivalent Te-BO-Te linkages
D	~600	Anti-symmetric stretching of [TeO$_4$]
E	~475	Symmetric bending and stretching vibration of Te-BO-Te linkages of [TeO$_N$] (N=4, 3+1 and 3)
F	~275	bending vibration of Te-NBO in [TeO$_3$] polyhedra
G	~130	intra-molecular asymmetric motion of the tellurium-oxygen bonds
Boson	~40	Vibration of medium-range structure

3. 3. 3. 3 *The impact of crucible material on Raman spectra of TeO$_2$-Na$_2$O glass*

The Raman spectra of X-0 glasses prepared in different crucibles are shown in **Figure 3-10**. Approximately 4 mol% Al$_2$O$_3$ was introduced to the X-0-ceramic glass (**Figure S. 19**), while it was only about 10 ppm Au introduced to the X-0-Au glass [124]. Since only a low concentration of Au was introduced to X-0-Au glass, the effect of Au on the glass structure is negligible. Hence the difference of X-0-ceramic glass relative to X-0-Au glass indicates the impact of dissolved Al$_2$O$_3$ on the glass structure.

The area ratio of peak (A+B) / peak (C+D) of X-0-ceramic is higher than that of X-0-Au, which indicates a higher ratio of Te-NBO bond / Te-BO-Te linkage in X-0-ceramic (**Figure 3-10**, insert table). According to a previous research [150], the Tg of TeO$_2$-based glass firstly decrease (Al$_2$O$_3$ <5 mol%) then increase as the content of Al$_2$O$_3$ increases, the decrease of Tg suggests the increase of NBO. Therefore, the higher ratio of Te-NBO bond / Te-BO-Te linkage in X-0-ceramic suggests

that the Al_2O_3 dissolved in X-0 glass forms more NBOs. I hypothesize, the formation of NBOs is related to the coordination number of aluminium, which need to be investigated further.

The positions of peak C, D and E shift towards high frequency in X-0-ceramic compared to X-0-Au, which illustrates the decrease of the Te-BO bond length in X-0-ceramic. Compared to the X-0-Au glass, the X-0-ceramic glass has Al^{3+} ions (radius=51 pm) [84] as additional glass network modifier ions that are squeezed into the glass network, which shortens the Te-BO bond.

Compared to X-0-Au, the X-0-ceramic has a Boson peak shifted to a higher frequency, which suggests the Al_2O_3 (< 5 mol%) introduced to X-0 glass reduces the fragility of the specimen.

Inset table (left):

	Au	Ceramic
Te-NBO bond	0.170	0.182
Te-BO-Te linkage	0.109	0.110
Ratio	1.560	1.655

Right table:

Peak/crucible	position (error $\pm$ 1)
Peak E/Au	467
Peak E/ceramic	473
Peak D/Au	603
Peak D/ceramic	614
Peak C/Au	661
Peak C/ceramic	669
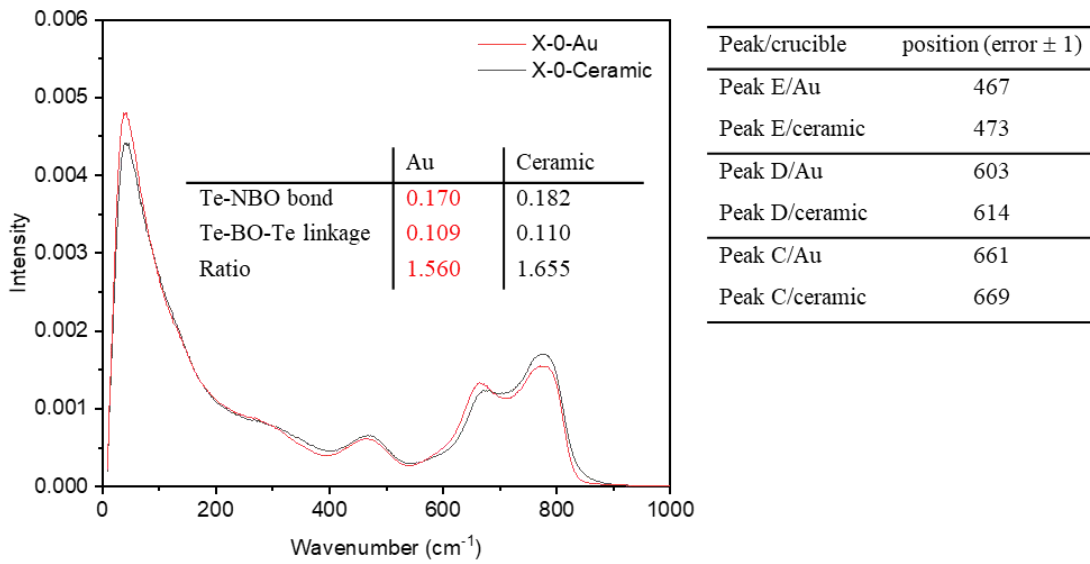
Figure 3-10 Left spectra shows the Raman spectra of X-0 glasses prepared in gold crucible (red curve) or ceramic crucible (black curve), with the insert table showing the ratio of Te-NBO bond over Te-BO-Te linkages. Right table shows the positions of peak C, D and E.

3. 3. 3. 4 Overview of the structural evolution caused by the changes of NaX

Raman spectra are divided into 3 regions. Compared to the second region (150~550 cm^{-1}), the first (0~150 cm^{-1}) and the third (550~900 cm^{-1}) regions exhibit more discernible variation as the concentration of NaX increases in 68TeO$_2$-(32-x/2)Na$_2$O-xNaX glasses (**Figure 3-11**). Adding NaI induces the most significant structural impact to the TNN system, followed by NaBr then NaCl.
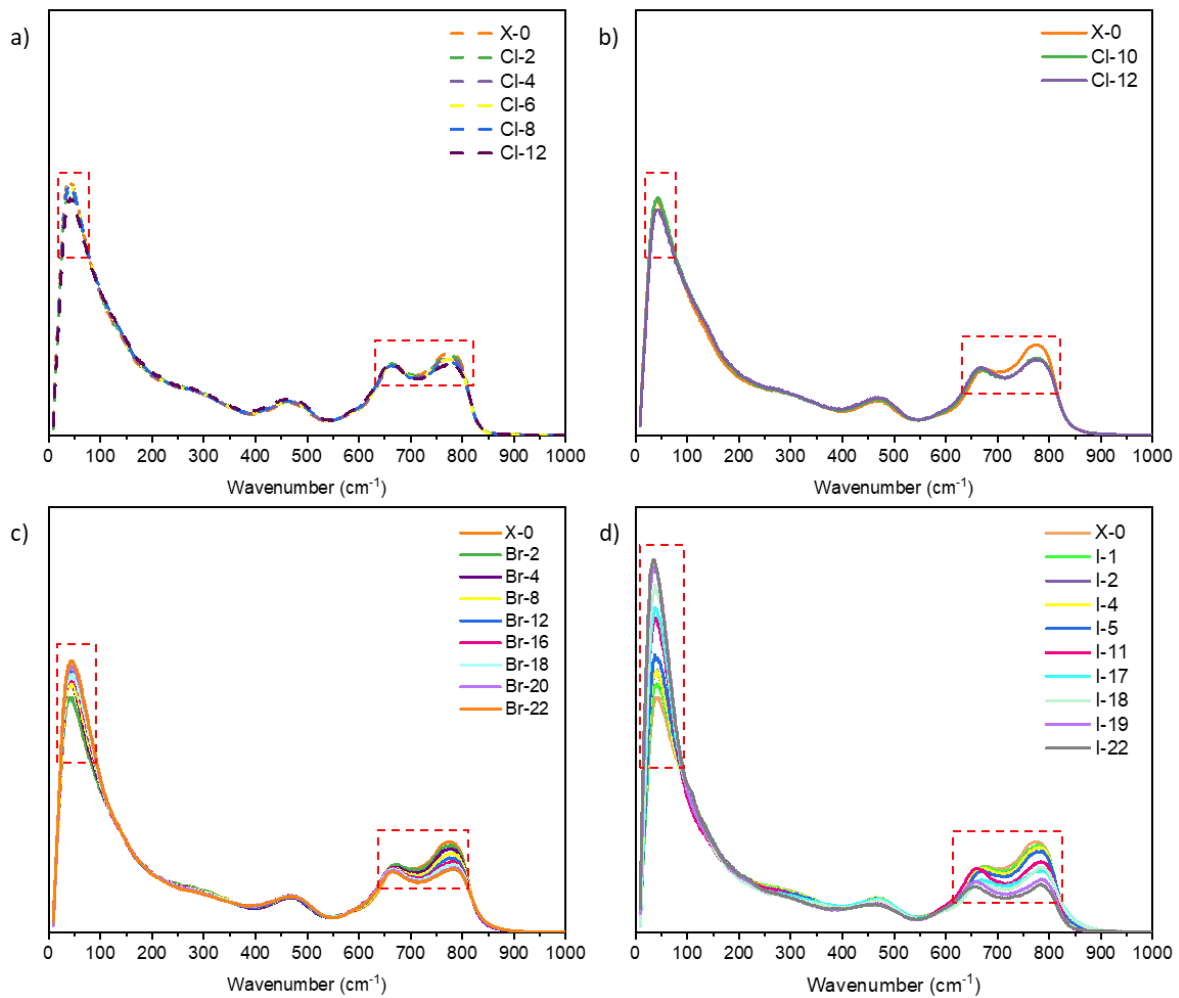
Figure 3-11 The Raman spectra of a) TN-Cl glasses prepared in gold crucible, b) TN-Cl glasses prepared in ceramic crucible, c) TN-Br glasses prepared in ceramic crucible, and d) TN-I glasses prepared in ceramic crucible. The red frames emphasize the regions which show discernible changes as the concentration of NaX increases.

Peak deconvolution (experimental section 3. 2. 6) is performed to correlate the Raman spectra with structural variation (more deconvolution examples presented in **Figure S. 13**). The detailed discussion on deconvoluted peaks is categorised into 3 parts, i.e., the vibration of tellurium with NBOs shown by peak A, B and F, the vibration of polyhedra with BOs depicted by peaks C, D and E, and fragility indicated by Boson peak.

.

3. 3. 3. 5 Impact of NaX on Te-NBO bonds

The Te-NBO bond-related peaks A, B and F are used to investigate the impact of NaX on the Te-NBO bonds. The NBO of the Te-NBO$_B$ bond (peak B) weakly interacts with the adjacent Te, while the NBO of the Te-NBO$_A$ (peak A) does not (section 3. 3. 3. 5), therefore, the Te-NBO$_B$ bond has a longer bond length and thus is located at lower frequency.

The peak B area remains constant while peak A area decreases as the concentration of NaX increases, suggesting the decrease of Te-NBO$_A$ bond (**Figure 3-12 a**). The peak A area reduction follows an order of TN-Cl < TN-Br < TN-I, whereby the TN-Cl shows only a minor decrease. As Na_2O is substituted by $(NaX)_2$, the concentration of NBO is decreased due to the reduction of Na_2O concentration. Ideally, for the glasses with the same concentration of Na_2O, the concentration of NBO should be reduced to the same extent. However, the TN-Cl has a higher concentration of NBO$_A$ than TN-Br and TN-I (with the same Na_2O concentration). As mentioned in the introduction (section 3. 1. 2. 2), the halides in TeO_2-Li_2O-LiCl glasses form Te-X bonds [76]. I hypothesize, the halides (Cl, Br, I) in TNN glasses also form Te-X bonds. The formation of Te-X bond is proposed to occur via the halide breaking the Te-BO-Te linkage, leading to the formation of Te-X and Te-NBO [77]:
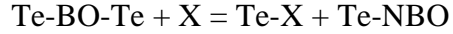
$$\text{Te-BO-Te} + X = \text{Te-X} + \text{Te-NBO} \qquad\qquad 3.33$$

The Te-NBOs formed via reaction 3.33 compensate the reduction of NBOs caused by the decrease of Na_2O concentration. Since the Te-X bond located at low frequency is not observed in the Raman spectrum of TeO_2-based glasses [151], more evidence of demonstrating the formation of Te-X (e.g., by X-ray photoelectron spectroscopy) is required to support this hypothesis, which can be a future study.

Furthermore, considering Na_2O is replaced by $(NaX)_2$, the concentration of introduced X is twice of the substituted O, which means, if all of the halides break Te-BO-Te and form Te-NBO, the amount of Te-NBO should increase. However, the amount of Te-NBO decreases as observed, which means only a part of the halides form Te-X bonds, the remaining halides are supposed to be in the interstitial sites as anions (halide ion Cl^-, Br^-, I^-). The order of NBO concentration (TN-Cl > TN-Br > TN-I) suggests the likelihood of forming Te-X follows the order of Cl > Br > I, which means the amount of Te-X bond follows Te-Cl > Te-Br > Te-I, therefore, the concentration of halide ion in the interstitial sites follows $I^- > Br^- > Cl^-$. According to electronegativities (EN), the Te-X bond strength follows Te-Cl > Te-Br > Te-I, which suggests a higher possibility of forming Te-Cl (for the same amount of X).
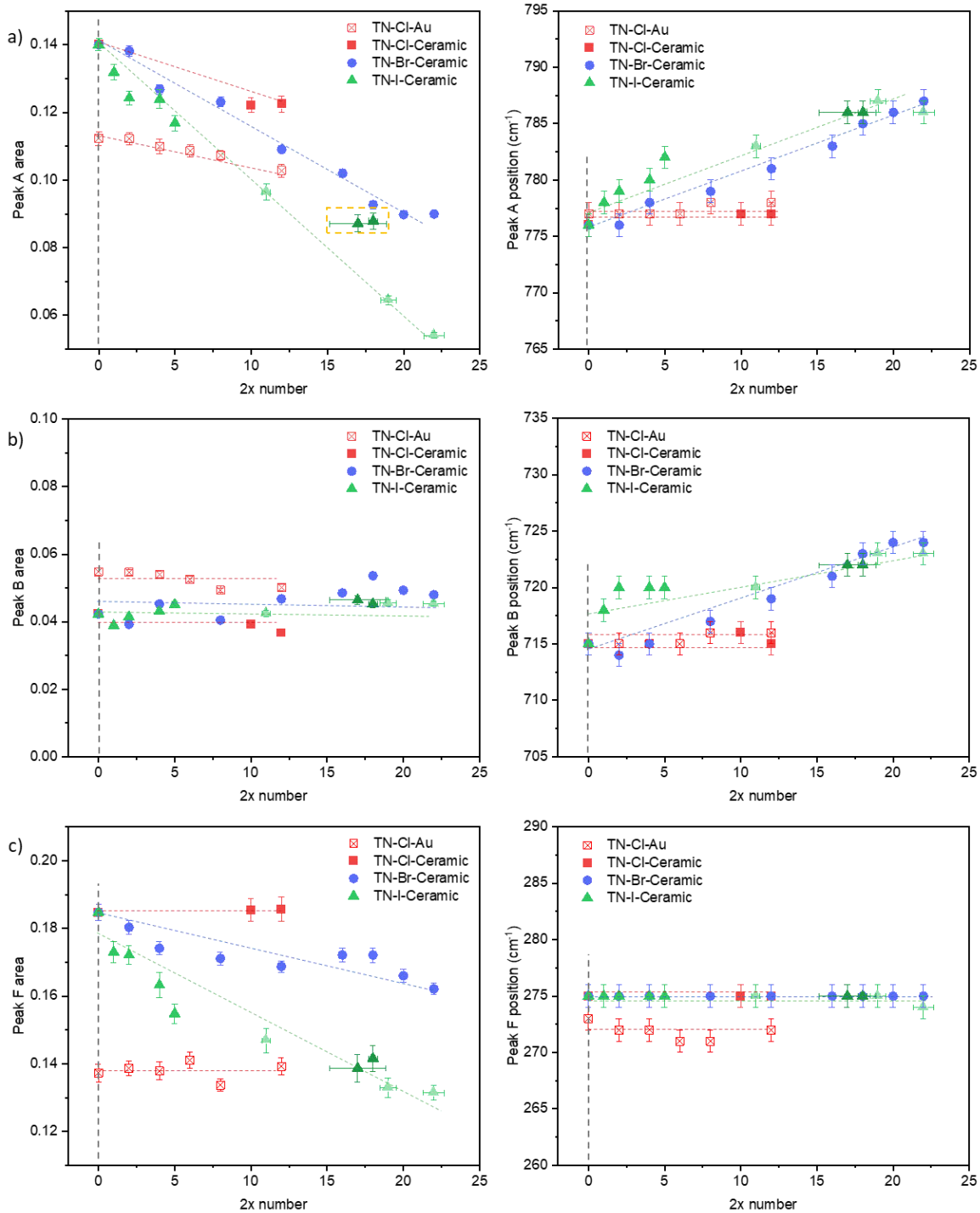
Figure 3-12 The peak positions and areas of a) peak A, b) peak B and c) peak F of TNN glasses, with dash-lines as guides for viewing. For comparison, the differences for y-axis are set to be 0.1~0.12 and 30 cm^{-1} for peak area and peak position, respectively. Note: light green colour highlights the TN-NaI glasses prepared at 550 °C, the deep green colour indicates those prepared using three-step melting method (section 3. 2. 1). The shaded box (in a) indicates the samples prepared using three-step method.

The peak B area remains unchanged (**Figure 3-12 b**), which indicates the amount of Te-NBO$_B$ bonds is independent of the NaX (or Na$_2$O) concentration. I hypothesize two possible reasons to explain this phenomenon:

1) As mentioned in section 3.3.3.2, the NBO of Te-NBO$_A$ has no interaction with the adjacent Te (of another polyhedron), while the NBO of Te-NBO$_B$ interacts with the adjacent Te. Due to this interaction, Te-NBO$_B$ is more stable (less likely to be broken) than Te-NBO$_A$. As the concentration of Na$_2$O is reduced, the amount of Te-NBO$_A$ bonds firstly decreases since Te-NBO$_A$ is less stable. In this study, the observation that the amount of Te-NBO$_B$ bonds of TNN glasses remains constant suggests that the Te-NBO$_B$ bond is not affected by a decrease of Na$_2$O. Considering only the amount of Te-NBO$_A$ bonds is reduced, the Te-NBO bonds formed by the halide breaking the Te-O-Te linkage (reaction 3.33) are more likely to be Te-NBO$_A$ bonds.

2) The concentrations of Te-NBO$_A$ and Te-NBO$_B$ are equally reduced with a reduction of Na$_2$O concentration. Different from the above hypothesis 1), in this hypothesis 2), the halide breaking the Te-O-Te linkage (reaction 3.33) tends to form more Te-NBO$_B$ than Te-NBO$_A$, thus the amount of Te-NBO$_B$ is not changed.

A further investigation is needed to reveal the mechanism of Te-NBO$_A$ and Te-NBO$_B$ reduction, e.g., comparing the changes of Te-NBO$_A$ and Te-NBO$_B$ concentrations of TN glasses with different Na$_2$O concentration.

The area of peak F of the TN-Br and TN-I glass systems decreases as the concentration of NaBr or NaI increases, suggesting the total amount of Te-NBO bonds decrease. As discussed above, such reduction is mainly attributed to the decrease of Te-NBO$_A$ bonds. In contrast, the peak F area of TN-Cl does not discernibly decrease, suggesting the peak F area is inert to the minor change

(here reduction) of Te-NBO$_A$ bonds. According to E.I. Kamitsos et.al. [143, 144], this peak also corresponds to the motion of Na$^+$ ions [144]. Since the concentration of Na$^+$ is constant in all TNN glasses, the motion of Na$^+$ ions in TNN glasses does not contribute to the variation of peak F areas. The positions of peaks A and B of TN-Br and TN-I are shifted to high frequency as the concentration of NaBr and NaI increases (**Figure 3-12 a, b**), which means the presence of Br and I causes the shortening of both Te-NBO$_A$ and Te-NBO$_B$ bonds. Irrespective whether a halide occurs as bound -X or ionic X$^-$, its larger size means it needs to be squeezed into the glass network, which results in the shortening of the Te-NBO bonds in TN-Br and TN-I. The positions of peak A and B of TN-Cl remain nearly constant as the concentration of NaCl increases, which means the presence of Cl in TNN glass system does not change the length of Te-NBO bond. Cl$^-$ does not shorten the Te-NBO bond because the Cl$^-$ ion (radius=180 pm [84]) has a smaller size than Br$^-$ (radius=196 pm [84]) and I$^-$ (radius=220 pm [84]).

The observation that peak F position remains constant suggests that the frequency of the bending vibration of Te-NBO bonds is independent of NaX concentration, which means the addition of NaX only affects the stretching vibration but not the bending vibration of Te-NBO.

Comparing the TN-Cl system prepared in gold or ceramic crucible (**Figure 3-12**), the TN-Cl-ceramic system has a higher concentration of Te-NBO$_A$, according to the comparison of peak A and peak F areas. This observation agrees with the discussion of X-0 glasses.

The peak A areas of samples I-17 and I-18 (prepared by three-step method) are slightly higher than the expected values (indicated by the green-dash line of **Figure 3-12 a**), the cause of this result is not clear, it might be due to i) less reduction of NBO caused by reduced Na$_2$O concentration and/or ii) more NBO formed via the halide breaking the Te-O-Te linkage (reaction 3.33).

3. 3. 3. 6 Impact of NaX on Te-BO-Te linkage

As Na_2O is substituted by NaX, the Te-BO-Te linkage is affected in two opposite ways, i) the amount of Te-BO-Te linkage increases due to the decrease of Na_2O concentration; ii) the amount of Te-BO-Te linkage reduces due to the reaction 3.33 (Te-BO-Te + X = Te-X + Te-NBO). These effects are discussed based on the analysis of the peaks C, D and E, which reflect the vibrations of Te-BO-Te linkages. The areas of peak C, D and E indicate the concentration of $[TeO_4]$ + $[TeO_{3+1}]$, $[TeO_4]$, and the network continuity, respectively, while the positions of those peaks indicate the length of the Te-BO bond in Te-BO-Te linkages of the corresponding polyhedra.

Figure 3-13 a and **b** show that the area of peak C slightly increases as the concentration of NaX increases (except for TN-I with $2x > 11$). In contrast, the area of peak D decreases with increasing NaX concentration. It means that the concentration of $[TeO_4]$ + $[TeO_{3+1}]$ polyhedra increases while the concentration of $[TeO_4]$ polyhedra decreases. This phenomenon suggests, the halides with large size induce pressure to the network, leading to a distortion of a portion of the $[TeO_4]$ polyhedra (adjacent to halides) into $[TeO_{3+1}]$ polyhedra. Since this effect depends on the size but not the form (bound or ionic) of halides, I suppose, both the halides in the form of Te-X bonds and interstitial X^- ions have the same effect on distorting $[TeO_4]$ polyhedra (similar to the effect of halide on the length of Te-NBO bond). The degree of $[TeO_4]$ polyhedra reduction follows the order of TN-Cl < TN-Br < TN-I, suggesting the halide with a larger size tends to distort more $[TeO_4]$ polyhedra. The area of peak E slightly increases as the concentration of NaX increases (except for I-19 and I-22), which suggests the network continuity is slightly enhanced (**Figure 3-13 c**). This enhancement indicates the increase of Te-BO-Te concentration caused by decreasing Na_2O exceeds the decrease of the Te-BO-Te concentration caused by reaction 3.33.
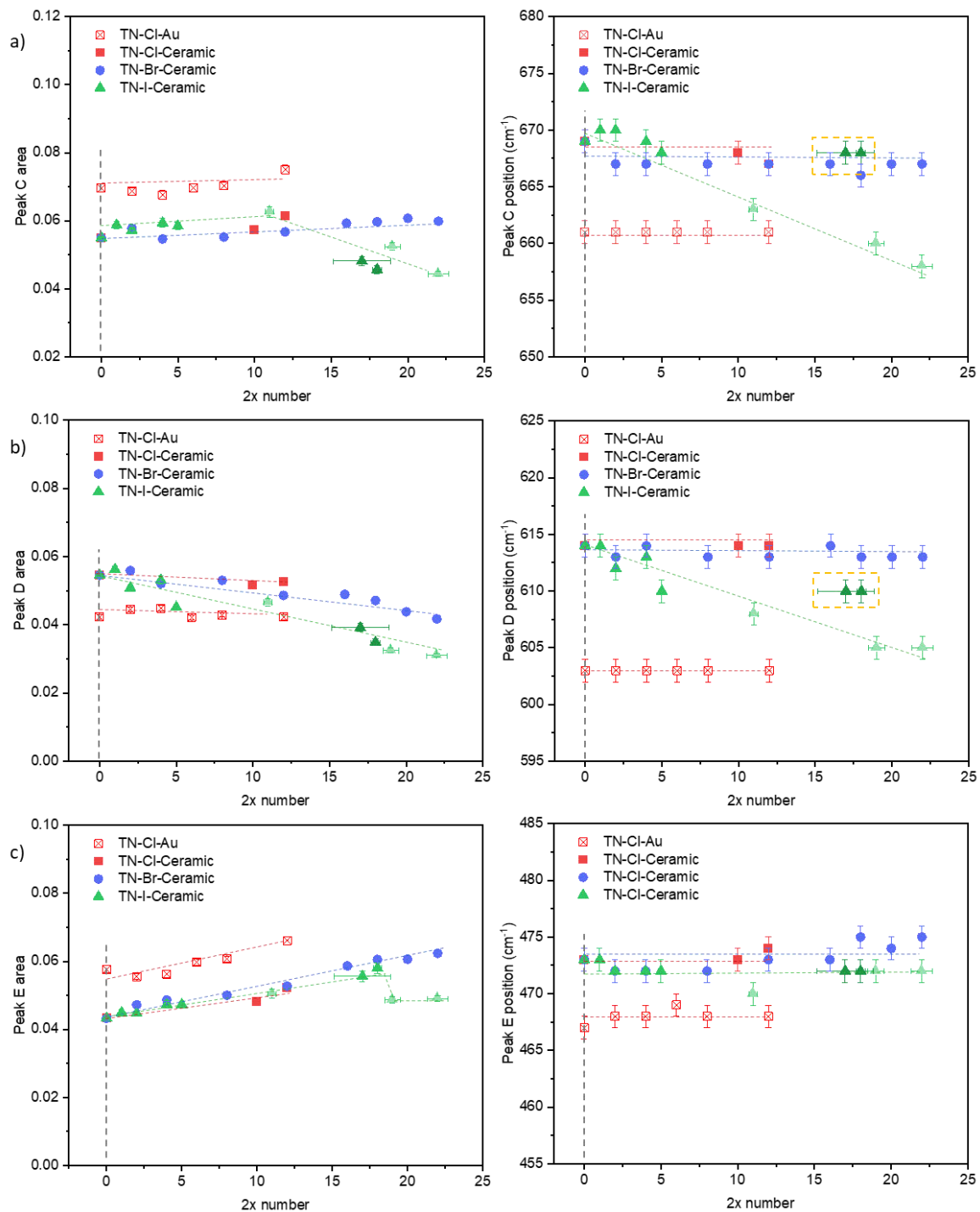
Figure 3-13 The peak positions and areas of a) peak C, b) peak D and c) peak E of TNN glasses, with dash-lines as guides for viewing. For comparison, the differences for y-axis are set to be 0.1 and 30 cm^{-1} for peak area and peak position, respectively. Note: light green colour highlights the TN-NaI glasses prepared at 550 °C, the deep green colour indicates those prepared using three-step melting method. The shaded box (in a) indicates the samples prepared using three-step method.

For the TN-I glasses, the concentration of $[TeO_4]$ + $[TeO_{3+1}]$ experiences a decline at $2x > 11$ and the network continuity deteriorates at $2x > 18$ (depicted by the peak areas of C and E, **Figure 3-13 a, c**). I propose, as the concentration of $(NaI)_2$ increases, the amount of I^- ions in the interstitial sites saturated, and the excess I^- ions break the Te-BO-Te linkages and result in the decrease of $[TeO_4]$ + $[TeO_{3+1}]$ concentration and network continuity.

The positions of peak C and D of TN-Cl and TN-Br systems are independent of the NaCl or NaBr concentration, while that of TN-I system is red shifted as the concentration of NaI increases (**Figure 3-13 a, b**). This observation suggests the Te-BO bond length of Te-BO-Te linkage is not affected by Br^- and Cl^- but increased by I^- ion, which indicates the continuous network being expanded by the large I^- ions (radius=220 pm [84]). The specimens that were prepared using the three-steps melting method (I-17 and I-18) are an exception of such effect, proposedly due to the localised inhomogeneity of the composition, which remains to be further investigated.

Comparing the TN-Cl glasses prepared in different crucibles (Au or ceramic), the TN-Cl-ceramic system shows a lower network continuity (peak E area). The total amount of Te-BO-Te linkages of TN-Cl-Au and TN-Cl-ceramic (Peak area C + D) is equal. The vibrational frequencies (peak positions C, D, E) of TN-Cl-ceramic system are higher than those of TN-Cl-Au system. These observations agree with the discussion on X-0 glasses.

3. 3. 3. 7 Investigation of the fragility via the Boson peak

The Boson peak shift to lower frequency (red-shift) indicates an increase of the fragility of a glass [149] (**Figure 3-14**). As the concentration of NaX increases, the position of the Boson peak remains constant in TN-Cl and TN-Br systems but red-shifts in TN-I system, suggesting the fragility of TN-Cl and TN-Br is not changed while that of TN-I glass is increased by the addition of NaX.

The TN-0 glass prepared in a ceramic crucible shows a Boson peak with higher frequency compared to that prepared in a gold crucible, which suggests a lower fragility of TN-0-Ceramic. K. B. Kavaklıoğlu et.al. and Dongmei Zhu et.al. discovered the relationship between glass transition temperature (Tg) and liquid fragility index, which are both correlated to the viscosity [89, 152]. As indicated by their report, a higher Tg indicates a lower fragility. The Tg values of TNN glasses were measured and are presented in **figure S.14**. The specimens prepared in a ceramic crucible have higher Tg than those prepared in a gold crucible, which agrees with the hypothesis that the observation of a Boson peak with higher frequency indicates lower fragility. More experimental data and measurements are required to correlate the variation of glass properties (e.g., Tg and fragility) to the Boson peak of TNN glasses, which can be a future study.
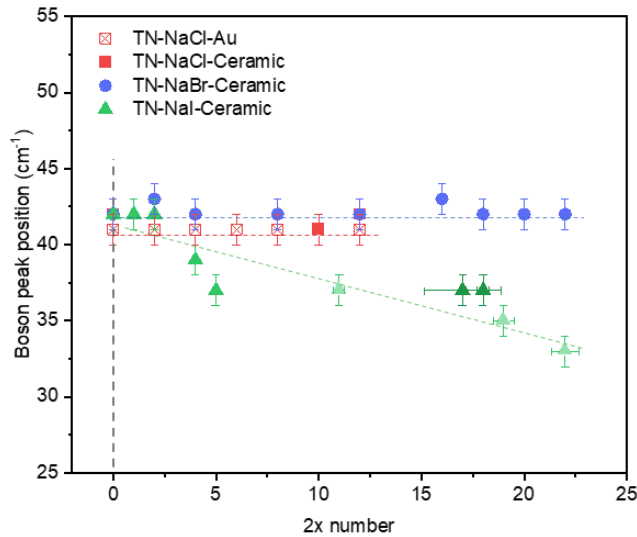
Figure 3-14 The plots of Boson peak positions of TN-NaCl, TN-NaBr and TN-NaI glass systems, with dot-lines as guides for viewing. Note: light green colour highlights the TN-NaI glasses prepared at 550 °C, the deep green colour indicates those prepared using three-step melting method.

3. 3. 4 Densities, molar mass, molar volume, and free volume

The densities of TNN glasses (except for I-11, I-19 and I-22) decrease with increasing NaX concentration (**Figure 3-15**). The specimens I-11, I-19 and I-22 (melted at 550 ℃) show higher densities than the other TN-I glasses (**Figure 3-15** light green colour). Since specimens I-11, I-19 and I-22 are not in line with the other TN-I glasses, they are excluded in the discussion presented below.
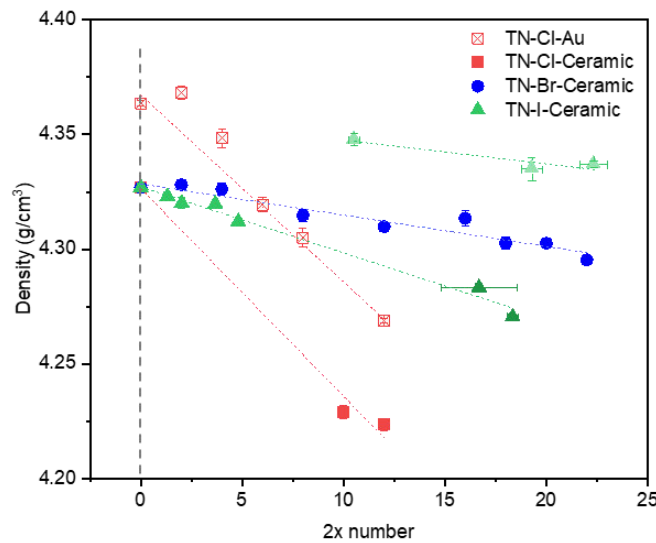
Figure 3-15 The densities of TN-Cl, TN-Br and TN-I. The coloured lines illustrate the linearly decreasing densities with an increase of halide concentration. Note: the light green colour highlights the TN-I glasses prepared at 550 ℃, the deep green colour indicates those prepared using three-step melting method.

The TN-Cl system shows a higher decline of densities compared to the TN-Br and TN-I systems. To uncover the cause of density variation, the molar mass (M) and molar volumes (V) were calculated. M and V increase as the concentration of NaX increases (**Figure 3-16**). Since $\rho = M/V$, M and V have opposite impact on the density. M increases with the increase of halide concentration and halide molar mass. The increase of V indicates the network is expanded by the NaX, because the halide ions have larger sizes than O^{2-} ion. When the slopes of M and V are plotted against the

atomic mass and ionic size, respectively, a linear relationship is observed (**Figure 3-16**), which

indicates the variation of *M* and *V* is determined by the atomic mass and ionic size.
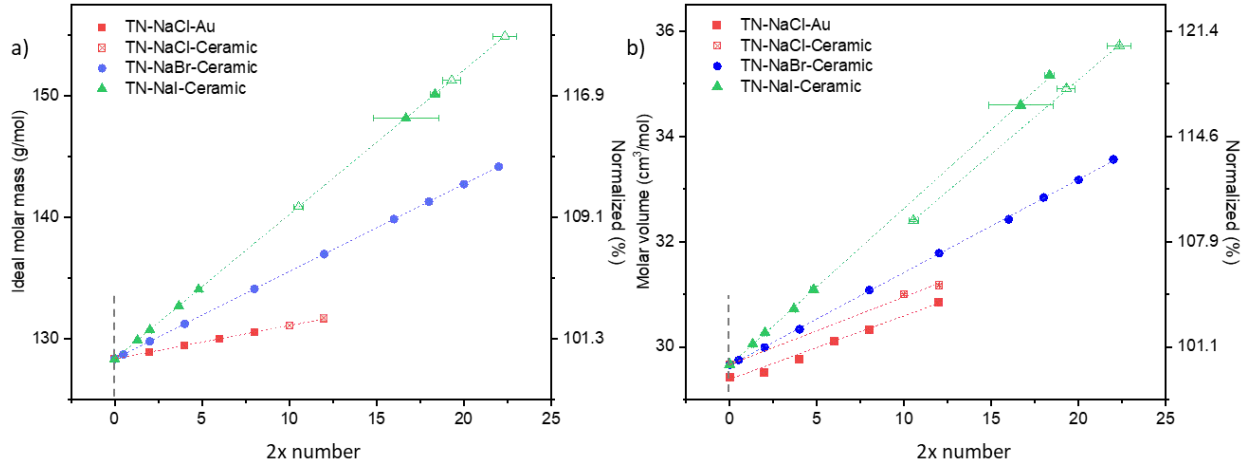
Figure 3-16 The a) molar mass and b) molar volume of TN-Cl, TN-Br and TN-I. The y-axis of left side
shows original data, while that of right side indicates the percentage of variation compared to the data of
X-0 glass.

The increase of *M* causes an increase of density, while the increase of *V* decreases the density.

Since the *M* and *V* increase up to 2.6% and 6% for TN-Cl, 12.3% and 13.1% for TN-Br, 17% and

18.5% for TN-I, respectively, the decrease of density is due to the increase of *V* overwhelming the

increase of *M*. Compared to the TN-Cl, the TN-Br and TN-I show a smaller difference between *M*

and *V*, thus exhibit less decrease of the densities with an increase of halide concentration.
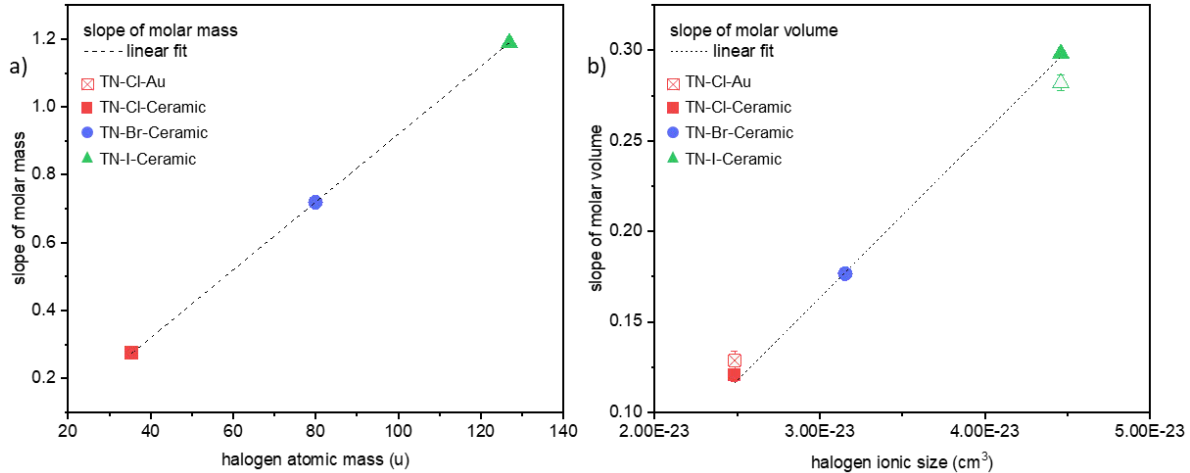
Figure 3-17 The plot of maximum variations (of molar mass or molar volume) against the parameters (atomic mass or ionic size) of halides (Cl, Br and I). The dot line shows linear fits of data points, whose R-square are all above 0.997. a) Plot of maximum molar masses change VS atomic mass. b) Plot of maximum variation of molar volume vs ionic sizes.

To unravel the effect of halides on the glass-structure, the free volume (V_{free}) was calculated using the density, V and composition. As the concentration of NaX increases, the V_{free} of all the three systems TN-Cl, TN-Br and TN-I increases linearly with the concentration of NaX (**Figure 3-18**). The slopes of the V_{free} follow the order of TN-Cl < TN-Br < TN-I. Comparing **Figure 3-18 a** with **Figure 3-18 b**, the plot of V_{free} appears like that of V, suggesting as expected the V_{free} is proportional to the V. Additionally, the plot of the V_{free}-slopes against the sizes of Cl⁻, Br⁻ and I⁻ ions follows a linear relationship (**Figure 3-18 b**), supporting the conclusion that the ionic size to a large extent determines the V_{free}.
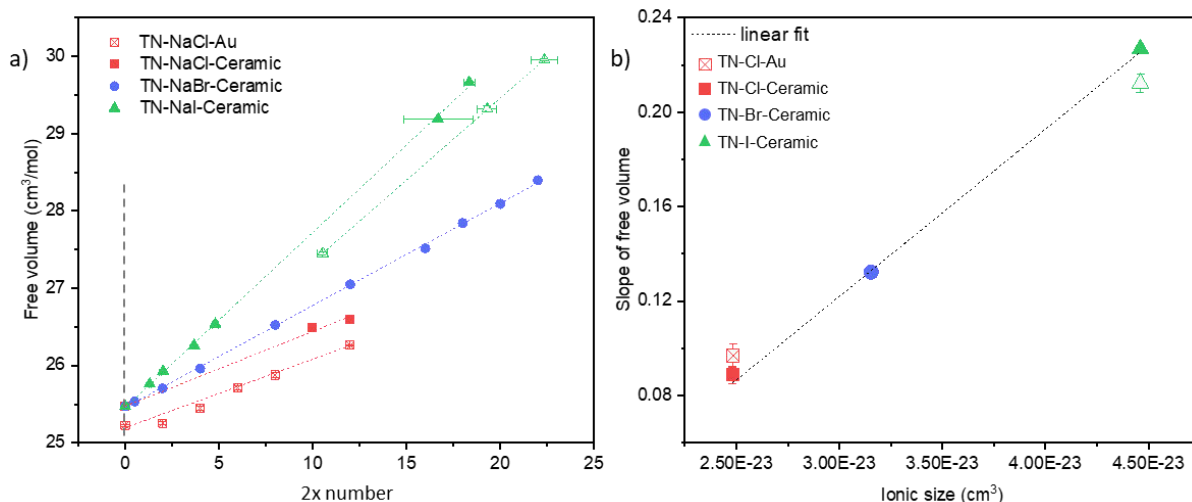
Figure 3-18 a) The free volume of TN-Cl, TN-Br and TN-I glasses. Dot-lines show the linear fitting of the data points. b) the fitting slopes (of a) are plotted against the ionic sizes of Cl⁻, Br⁻ and I⁻, along with a linear fitting to show their relationship.

Table 3-7 Summary of the variation of density, molar mass (M), molar volume (V) and free volume (V_{free}) of TN-Cl, TN-Br and TN-I glasses. The "-" suggests declining and "+" means rising, as the concentration of NaX increases. The numbers of "-" and "+" suggest the degree of declining or rising.

System	Density	M	V	V_{free}
TN-NaCl	- - -	+	+	+
TN-NaBr	- -	++	++	++
TN-NaI	- -	+++	+ + +	+++

In summary (**Table 3-7**), as the Na_2O is substituted by $(NaX)_2$ to form $68TeO_2$-$(32$-$x)Na_2O$-$x(NaX)_2$ glasses,

1) as the concentration of NaX (X=Cl, Br and I) increases, both the M and V increase proportionally to the atomic mass and ionic size of the halide, respectively.

2) the increase of M and/or the decrease of V causes the increase of V_{free}.

3) the increase of V overwhelming the increase of M, therefore, results in the decrease of the densities.

3. 3. 5 Volume and surface crystallization

The ratio of crystals (volume and surface) is an important parameter for the impedance measurements (below section 3. 3. 6). The volume crystal ratio was calculated based on the SEM images of the fresh cross-sections, while the ratio of the surface crystal volume over the glass volume was estimated from an SEM image of a hydrolysed surface.

The fresh cross-sections were created by cleavage which gives access to the inside of specimen for SEM measurement. The SEM images of all specimens show clean surfaces with a small number of particles (**Figure 3-19**), which are recognized as volume crystals. According to a further analysis using the software ImageJ [153], the particles occupy an area of 1.08% ± 0.59% of the total area (**Figure S. 20**). Therefore, the volume crystal fraction for all specimens is approximated as 1%. This crystal fraction is below the resolution of XRD (4 vol%), thus no crystal was detected in XRD.
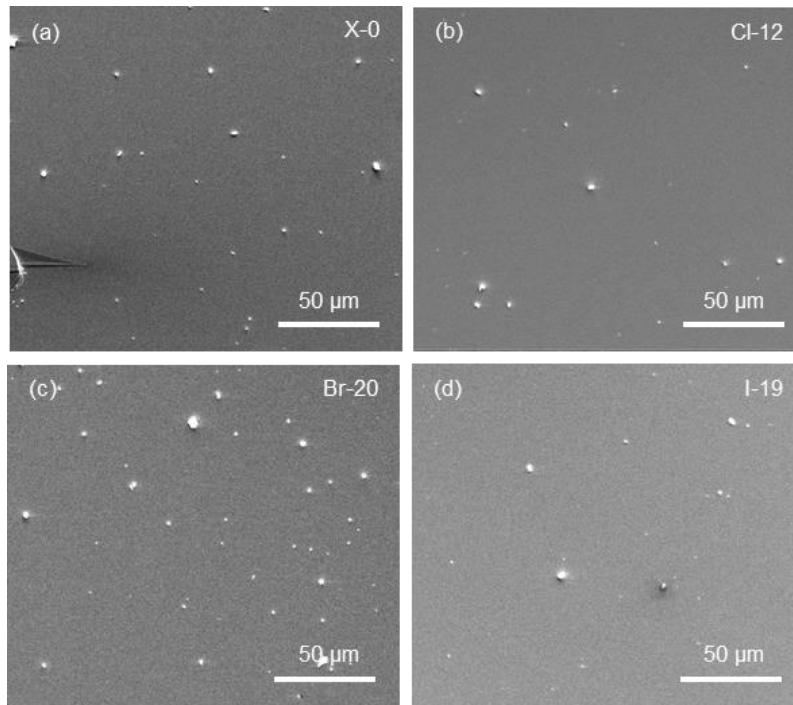
Figure 3-19 The SEM images of fresh cross-section of (a) X-0, (b) Cl-10, (c) Br-20 and (d) I-19 glasses.
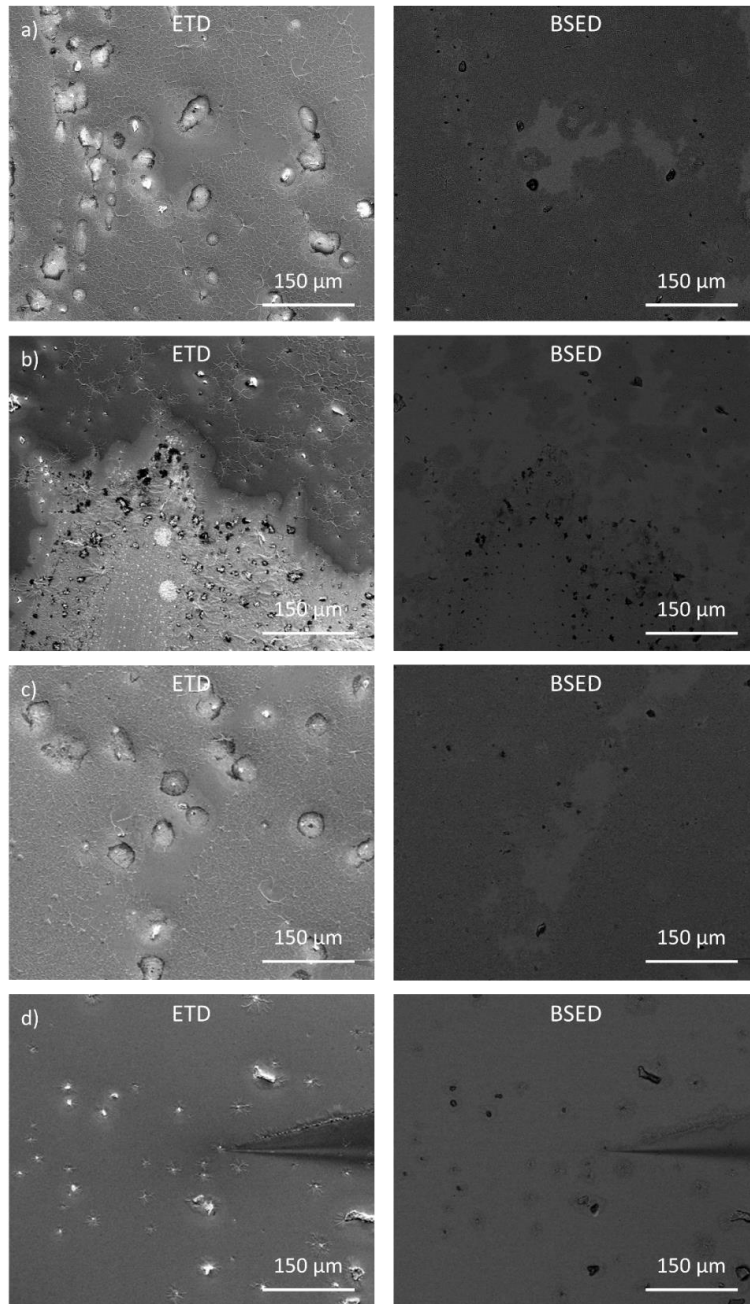
Figure 3-20 The SEM images of the exposed-heated surface of (a) X-0, (b) Cl-10, (c) Br-20 and (d) I-19 glasses. The left row shows images obtained using ETD mode while BSED mode for the right row.

During the IS measurement, the specimens were exposed to open air and heated (**section 3.2.8**), therefore, to simulate the surface crystallization after IS measurement, a set of specimens for SEM

measurement was exposed and heat-treated (exposed-heated specimens). Compared to the fresh cross-section, the exposed-heated surfaces show a high amount of crystals (**Figure 3-20**), which are formed due to hydrolysis. It is noticed, these crystals appear to be isolated islands unevenly dispersed on the surface. Irregular cycles around the crystals indicate that the surrounding areas of crystals in these specimens are affected by the formation of crystals. Under the BSED mode (**Figure 3-20**), these crystals are comparatively darker than the glass region, suggesting a lower mass of the crystals. According to the elemental analysis using EDX (**Figure S. 21**), such lower mass is attributed to the crystals showing a higher concentration of sodium compared to the glass region.
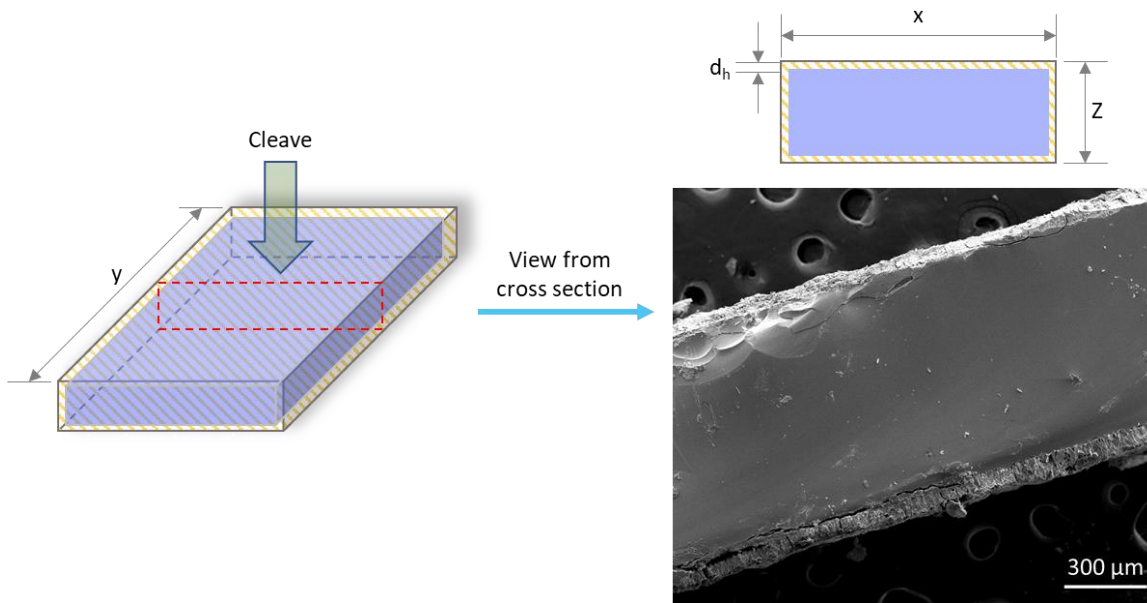
Figure 3-21 The two surfaces of X-0 were attacked by water to mimic the worst scenario of hydrolysation. The hydrolysed surface layer thickness (20 positions measured): $d_h = 67 \pm 15$ µm.

The surface crystal layer thickness is required for the IS analysis, however, since the surface crystals appear to be isolated islands, it is difficult to estimate the surface crystal thickness relied

on exposed-heated specimens. To bypass this issue, the worst scenario of surface crystallization (i.e., X-0 glass with fully hydrolysed surface) is used to estimate the surface crystal thickness (**Figure 3-21**), which is found to be about 67 ± 15 µm. Thus, the hydrolysed surface for all specimens is approximated to be 67 ± 15 µm. As indicated by the schematic diagram, the volume ratio of the surface crystal volume to the whole glass volume can be expressed as:

$$x_{surface} = \frac{(x - d_h) * (y - d_h) * (z - d_h)}{x * y * z} \qquad 3.34$$

where the x, y, z are the width, length and thickness of specimens. The dimensional parameters of four specimens are used for the estimation of the $X_{surface}$ (**Table S. 6**), which is about $12\% \pm 5\%$. Considering this value is obtained from the worst scenario, the $X_{surface}$ for all specimens is estimated to be the lower boundary of $12\% \pm 5\%$, which is 7%.

3. 3. 6 Electrical properties

The electrical properties of TNN glasses were measured and analysed using impedance spectroscopy (IS). A series of complex Z^{*} acquired from IS represents the frequency-dependent conducting process of TNN glasses [110]. To analyse the IS spectra, an *equivalent circuit* is firstly proposed to fit the experimental data and accordingly obtain the electrical parameters (i.e., resistance and capacitance). A *mathematical model* is subsequently developed based on the TNN glass-structure. For convenience, several terminologies that are used in this section are defined prior to further discussion.

   1) Element: it is referred to the smallest unit in a circuit, e.g., resistor (*R*) and capacitor (*C*).

   2) Component: two elements (e.g., *R* and *C*) aligned in parallel construct a component, e.g., *R* in parallel with *C*, marked as *R/C*.

3) Circuit: a set of components connected to positive and negative anodes is referred to as a circuit, e.g, two *R/C* components connected in series form a circuit marked as *-R/C-R/C-*. For the case of having one component connected to anodes, it is still noticed as circuit (i.e., marked as *-R/C-*).

4) Phase: the TNN glass system is composed of glass, volume crystals and surface crystals. Here, the glass is denoted as glass phase, while the crystals (volume and surface) and the boundary (e.g., boundary between glass and crystals) are generally referred to as impurity phase.

3. 3. 6. 1 Selection of equivalent circuit

Parallel -R/C- circuit

An ideal conduction process of a single phase homogenous material can be plausibly modelled by a circuit consisting of a resistor and a capacitor in parallel [154], i.e., *-R/C-* (**Figure 3-23**). Since $Z_R = R$ and $Z_c = \frac{1}{j\omega C}$, the complex impedance of *-R/C-* circuit is given by

$$\frac{1}{Z^*_{R/C}} = \frac{1}{Z_R} + \frac{1}{Z_C} = \frac{1}{R} + j\omega C \qquad 3.35$$

where *j* is the imaginary unit and ω is the angular frequency. Thus, the complex impedance of *-R/C-* is derived as:

$$Z^*_{R/C} = Z' + jZ'' = \frac{R}{1 + j\omega RC} = \frac{R}{1 + (\omega RC)^2} - j\frac{\omega R^2 C}{1 + (\omega RC)^2} \qquad 3.36$$

where the real (*Z'*) and imaginary (*Z''*) parts of the complex impedance are expressed as ($\tau = RC$ is the relaxation time of *-R/C-* circuit):

$$Z' = \frac{R}{1 + (\omega\tau)^2} \qquad\qquad 3.37$$

$$Z'' = -\frac{\omega\tau R}{1 + (\omega\tau)^2} \qquad\qquad 3.38$$

Figure 3-22 shows the plot of real part vs imaginary part of the complex impedance, this plot is referred to as Nyquist plot. The Nyquist plot of an -R/C- circuit is an ideal semicircle as evidenced below: combining equation 3.38 and 3.37,

$$Z'^2 + Z''^2 = \frac{R^2 + (\omega\tau R)^2}{[1 + (\omega\tau)^2]^2} = \frac{R^2[(1 + (\omega\tau)^2]}{[1 + (\omega\tau)^2]^2} = \frac{R^2}{1 + (\omega\tau)^2} = R * Z' \qquad\qquad 3.39$$

the above equation 3.39 can be simplified as:

$$Z'^2 - R * Z' + Z''^2 = 0. \qquad\qquad 3.40$$

Then expressed in the form of circular equation as:

$$(Z' - \frac{R}{2})^2 + Z''^2 = \left(\frac{R}{2}\right)^2. \qquad\qquad 3.41$$

Thus, it is a circle with a diameter of R and a centre at (R/2, 0).
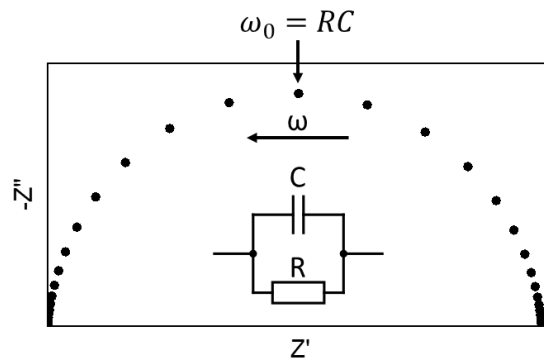
Figure 3-22 The Nyquist plot of the impedance spectrum of an ideal -R/C- circuit. An inset diagram shows the -R/C- circuit. The arrows indicate the direction of frequency. The peak frequency $\omega_0 = 2\pi f_0 = RC$ is indicated [107].

109

The vertex of a Nyquist plot is given by $\omega_0 RC = 1$, where $RC = \tau$ is the relaxation time constant and ω_0 is the eigen-angular-frequency of the -R/C- circuit. The -R/C- circuit can be applied for modelling the impedance spectra of bulk dielectric material characterized by a single time constant τ, e.g., an ideally homogenous glass.

-R$_1$/C$_1$-R$_2$/C$_2$- and -R$_1$/CPE$_1$-R$_2$/C$_2$- circuits

The Nyquist plot of the collected impedance data appears to be a non-ideal semicircle (**Figure 3-24**), which reflects the responses of the two phases (i.e., glass phase and impurity phase). Therefore, the consideration of equivalent circuit with two components is necessary. Since the impurity phase is mainly constituted of a thin crystalline layer on the surface of TNN glass (section 3. 3. 5), equivalent circuit of two components (representing two ideally homogenous phases) aligned in-series is selected, i.e., -R$_1$/C$_1$-R$_2$/C$_2$- (**Figure 3-23**). The complex impedance is expressed as:

$$Z^*_{eq} = Z^*_1 + Z^*_2. \tag{3.42}$$

The Z^*_1 and Z^*_2 are referred to the impedances of each R/C component of the -R$_1$/C$_1$-R$_2$/C$_2$- circuit. The total impedance of can be expressed in terms of real and imaginary parts as:

$$Z^*_{eq} = (Z'_1 + Z'_2) + j(Z''_1 + Z''_2). \tag{3.43}$$

For each R/C component, the complex impedance can be expressed as the equation 3.41 above. Thus, the overall expression for the -R$_1$/C$_1$-R$_2$/C$_2$- equivalent circuit is given as:

$$Z^*_{eq} = \left[\frac{R_1}{1 + (\omega\tau_1)^2} + \frac{R_2}{1 + (\omega\tau_2)^2}\right] - j\left[\frac{\omega\tau_1 R_1}{1 + (\omega\tau_1)^2} + \frac{\omega\tau_2 R_2}{1 + (\omega\tau_2)^2}\right]. \tag{3.44}$$

110
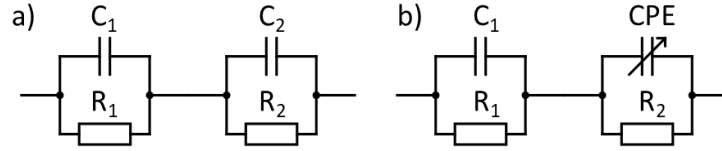
Figure 3-23 a) Schematic diagram of -R_1/C_1-R_2/C_2- circuit. b) Schematic diagram of -R_1/CPE-R_2/C_2-.

In practice, the glass phase is not ideally homogeneous, which means its conduction process cannot be represented by an ideal -R/C- circuit, instead, an empirical constant-phase-element (*CPE*) replacing the *C* of -R/C- circuit (denoted as R/CPE) is applied to represent the conducting response of glass phase [154]. Since $Z_{CPE} = \frac{1}{Q(j\omega)^\alpha}$, the complex impedance for R/CPE can be expressed as:

$$\frac{1}{Z^*_{R/CPE}} = \frac{1}{Z_R} + \frac{1}{Z_{CPE}} \tag{3.45}$$

$$Z^*_{R/CPE} = Z' + jZ'' = \frac{R(1 + \tau\omega^\alpha C_\alpha)}{1 + \tau^2\omega^{2\alpha} + 2\tau\omega^\alpha C_\alpha} - j\frac{R\tau\omega^\alpha S_\alpha}{1 + \tau^2\omega^{2\alpha} + 2\tau\omega^\alpha C_\alpha} \tag{3.46}$$

where $\tau = RQ$, Q is the capacitance of CPE. $C_\alpha = cos\frac{\pi\alpha}{2}$ and $S_\alpha = sin\frac{\pi\alpha}{2}$, α is a constant ($0 \leq \alpha \leq 1$) for each sample. A slightly submerged semicircle is obtained from the complex impedance plot of R/CPE component.

Thus, the overall expression for -R_1/CPE-R_2/C_2- equivalent circuit is given as:

$$Z^*_{eq} = \left[\frac{R_1(1 + \tau_1\omega^\alpha C_\alpha)}{1 + \tau_1^2\omega^{2\alpha} + 2\tau_1\omega^\alpha C_\alpha} + \frac{R_2}{1 + (\omega\tau_2)^2}\right] - j\left[\frac{R_1\tau_1\omega^\alpha S_\alpha}{1 + \tau_1^2\omega^{2\alpha} + 2\tau_1\omega^\alpha C_\alpha} + \frac{\omega\tau_2 R_2}{1 + (\omega\tau_2)^2}\right] \tag{3.47}$$

where the R_1/CPE represents the conduction process of the glass phase and the R_2/C_2 reflects the conduction process of the impurity phase. This mathematical expression is applied to fit the Nyquist plot of impedance data, via fitting the values of R_1, Q and α for *CPE*, R_2, and C_2 using the

software ZsimpWin (demo-version), the resistances and capacitances of the $-R_1/CPE-R_2/C_2-$ circuit can be obtained.

Figure 3-24 shows an example of Nyquist plot and the fitting of X-0 (**Figure S. 16**) at different temperatures (i.e. 170 °C, 140 °C, 110 °C and 80 °C). The frequency in Nyquist plot increases from right to left. The Nyquist plots of measured impedances appear to be distorted semicircles for all temperatures. At 80 °C, only 3/4 semicircle is showed in the Nyquist plot, the missing part contains the response above the measurement frequency. The data points are densely located on low and high frequency regions, those closely locating data points overly affect the fitting, therefore, several data points at those regions have been removed for the fitting procedure. The fitted data points (**Figure 3-24**, green spots) are mostly overlapping with the collected data points (**Figure 3-24**, black spots), which indicates a high fitting reliability.

Via fitting the collected data using the model of $-R_1/CPE-R_2/C_2-$ circuit (equation 3.49), the electrical parameters (R_1, Q and α , R_2, C_2) are obtained. Subsequently, the impedances of each component of $-R_1/CPE-R_2/C_2-$ circuit (i.e. Z_1' and Z_1'', Z_2' and Z_2'') are calculated according to the equation 3.47. The Nyquist plots of those two components are found to be one big semicircle (**Figure 3-24**, red spots) with a small semicircle (**Figure 3-24**, blue spots). The large one is assigned to be the impedance of R/CPE corresponding to the glass phase that occupies the main volume fraction. The small one is assigned to be the response of the impurity phase, which is about 7% of the volume fraction (section 3. 3. 5).
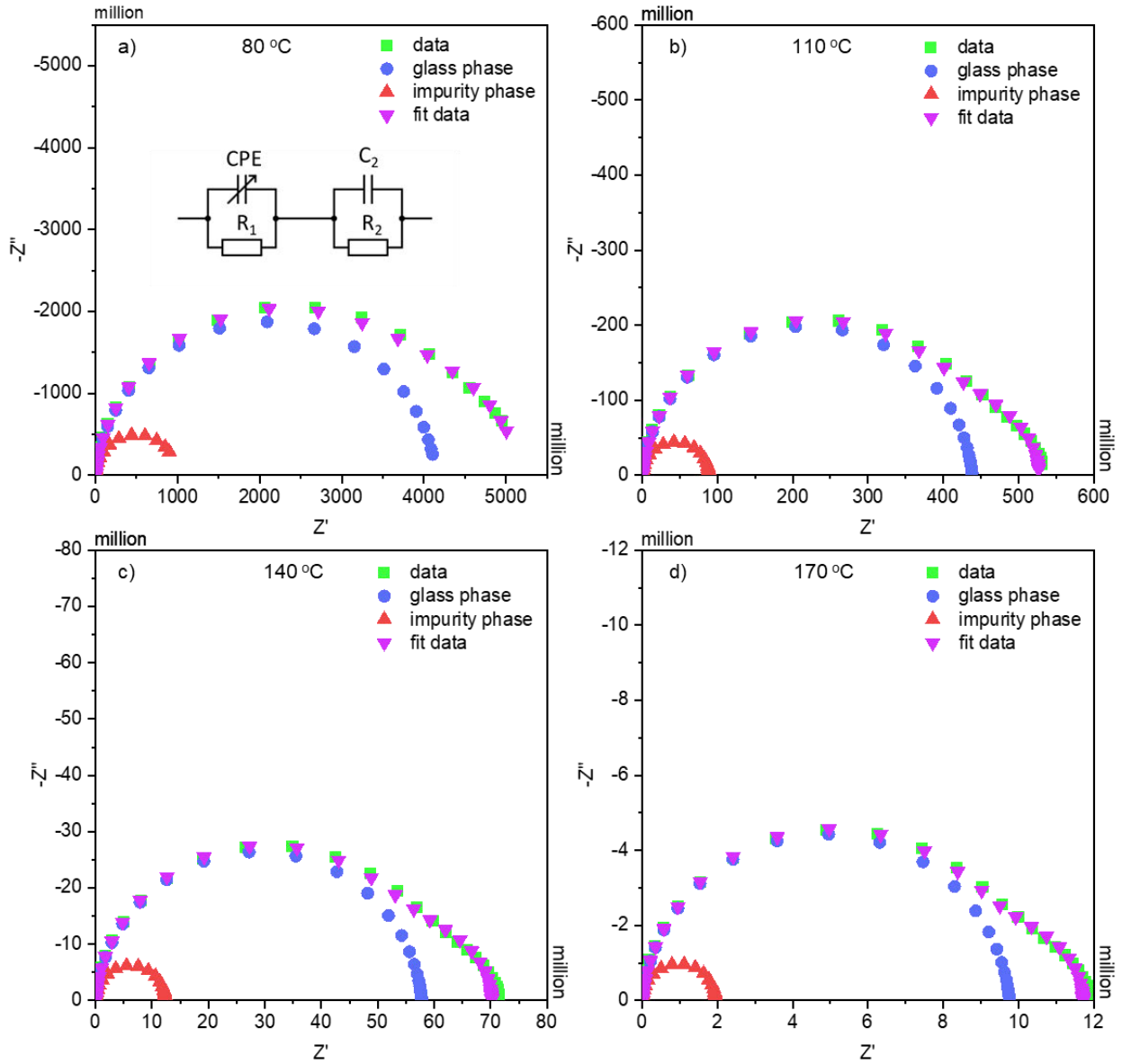
Figure 3-24 The Nyquist plots of the experimentally collected impedance data of X-0 and the fitted data obtained from -R_1/CPE-R_2/C_2- circuit, at different temperature a) 170 °C, b) 140 °C, c) 110 °C and d) 80 °C, respectively. The experimental data are closely overlapping with the fitted data, which indicates a high reliability of the fitting results. An insert diagram in a) shows the diagram of the equivalent circuit -R_1/CPE-R_2/C_2-.

3. 3. 6. 2 Mathematical model for material conductivity - Combination of two phases

The electrical parameters (R_1, Q and α, R_2, C_2) obtained from the fitting with an equivalent circuit are used to calculate the conductivity of TNN glasses. As discussed above (section 3. 3. 5), the surface crystals are the major contribution to the impurity phase, therefore, the TNN glasses presented in this research are plausibly modelled as two phases layering in series (layering-model, **Figure 3-25**) [155, 156].
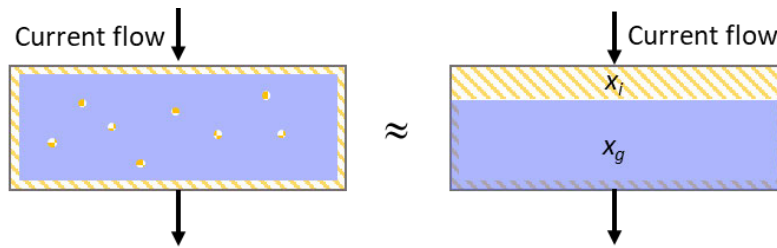
Figure 3-25 Schematic diagram for the layering-model, indicating the specimen with glass phase and impurity phase is proximately expressed by the layer model. x_g and x_i are the volume ratios of the layers, which correspond to the volume of glass phase and the volume of impurity phase.

Wiener analysed the laminar mixtures of two phases and developed an equation to correlate the impedance of each phase (Z_g and Z_i) with the total impedance (Z_m) for ionic conductive material, as [155-157]:

$$Z_m^* = Z_g^* x_g + Z_i^* x_i \qquad\qquad 3.48$$

where the subscripts m, g and i stand for measured, glass, and impurity phase, respectively. The x_g and x_i are the volume ration of glass phase and impurity phase. Since $Z_{eq}^* = Z_1^* + Z_2^*$, the equivalent circuit equation can be correlated to the mathematical model equation as $Z_{eq}^* = Z_m^*$, thus:

$$Z_1^* + Z_2^* = Z_g^* x_g + Z_i^* x_i. \tag{3.49}$$

Since Z_1^* and Z_2^* correspond to the measured impedance of glass phase and impurity phase, respectively, the complex Z_g^* is expressed as:

$$Z_g^* = Z_g' + jZ_g^" = \frac{Z_1' + jZ_1^"}{x_g}. \tag{3.50}$$

Since

$$\varepsilon = \frac{1}{j\omega c_c} * \frac{1}{Z} \tag{3.51}$$

where the $C_c = \varepsilon_0 \frac{A}{L}$ is the capacitance of empty cell, ε_0 is the permittivity of free space. And

$$\varepsilon^* = \varepsilon' + j\varepsilon^" \tag{3.52}$$

Combining equation 3.51 and 3.52, the ε' and $\varepsilon^"$ are expressed as,

$$\varepsilon' = \frac{-Z^"}{\omega C_c (Z'^2 + Z^{"2})} \tag{3.53}$$

$$\varepsilon^" = \frac{-Z'}{\omega C_c (Z'^2 + Z^{"2})}. \tag{3.54}$$

The frequency dependent conductivity is showed as [155]

$$\sigma_\omega = \omega \varepsilon_0 \varepsilon^". \tag{3.55}$$

Combining equations 3. 54 and 3. 55, the conductivity of glass phase $\sigma_{\omega(g)}$ is expressed in terms of impedance, as

$$\sigma_{\omega(g)} = \frac{-Z_g' L}{A(Z_g'^2 + Z_g^{"2})}. \tag{3.56}$$

Via substituting the equation 3.50 to equation 3.56, the $\sigma_{\omega(g)}$ is expressed by Z_1' and $Z_1^"$ as:

$$\sigma_{\omega(g)} = \frac{Z_1' L x_g}{A(Z_1'^2 + Z_1''^2)}.$$

3.57

Furthermore, the $\sigma_{\omega g}$ can be correlated to DC conductivity as [155]

$$\sigma_{\omega(g)} = \sigma_{DC(g)} + B\omega^m$$

3.58

where B and m are constants. The $\sigma_{\omega(g)}$ is plotted against the *log-frequency* (**Figure 3-26**). At low frequency region ($f < 100$ Hz), the conductivity tends to be constant, while at high frequency region ($f > 10^4$ Hz), the conductivity depends on the frequency. Because the contribution of the factor $B\omega^m$ to the $\sigma_{\omega(g)}$ is much lower than that of $\sigma_{DC(g)}$, at low frequency region, $\sigma_{\omega(g)} \approx \sigma_{DC(g)}$ (**Figure 3-26 b**).
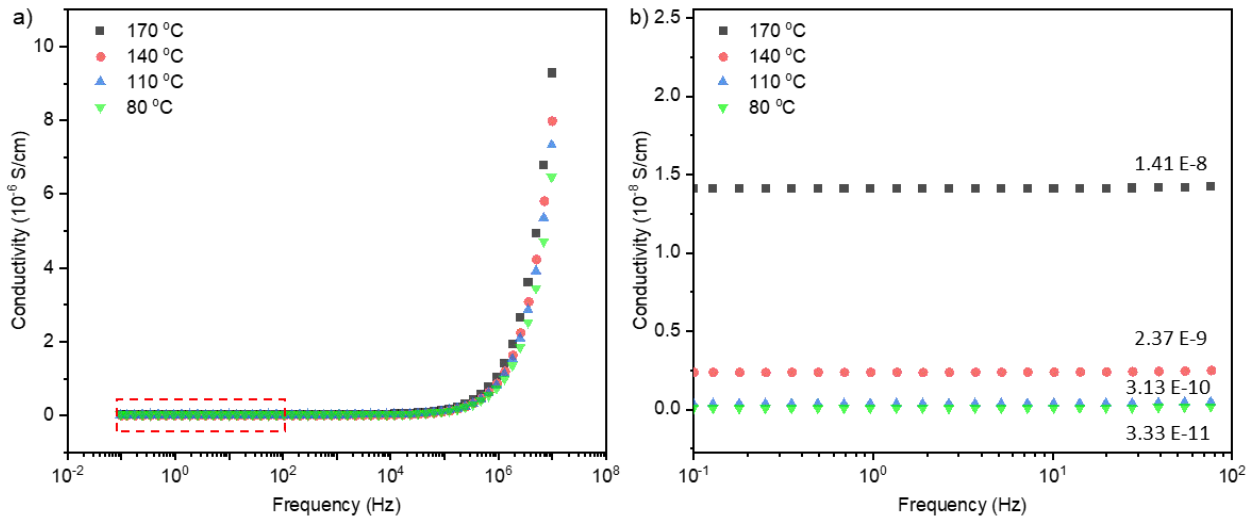
Figure 3-26 a) The frequency dependent conductivity of X-0 glass phase at different temperatures, with a red frame indicating the conductivity at low frequency. b) The zoom-in of the conductivity at low frequency region of a), the numbers show the as-obtained DC conductivity of the specimen at the corresponding temperature.

3. 3. 6. 3 Calculation of activation energy

The temperature dependence of the DC conductivity of TNN glasses matches well with an exponential function (**Figure 3-27**), which indicates the temperature and DC conductivity follow the Arrhenius law. Thus, the activation energy for DC conduction can be calculated based on the Arrhenius equation as [88, 158]

$$\sigma_{DC(g)} = A_0 \exp\left(-\frac{E_\sigma}{k_B T}\right). \tag{3.59}$$

In this equation, $E\sigma$ is the activation energy of conduction, A_0 is a constant, k_B is the Boltzmann constant ($k_B = 8.617333262145 \times 10^{-5}$ eV/K), and T is the temperature (in Kelvin).

Equation 3.59 can be transformed to a *log*-based equation as:

$$\log(\sigma_{DC(g)}) = \log(A_0) + \log\left[\exp\left(-\frac{E_\sigma}{kT}\right)\right] = \log(A_0) - \frac{E_\sigma}{2.3 * k} * \frac{1}{T}. \tag{3.60}$$

This equation shows the form of a linear equation ($y=-ax+b$), the slope a can be expressed as:

$$a = \frac{E_\sigma}{2.3 * k}. \tag{3.61}$$

This slope can be obtained via plotting the $\log(\sigma_{DC(g)})$ vs $1/T$ (**Figure 3-27 b**), accordingly, the E_σ can be calculated as:

$$E_\sigma = a * 2.3 * k. \tag{3.62}$$
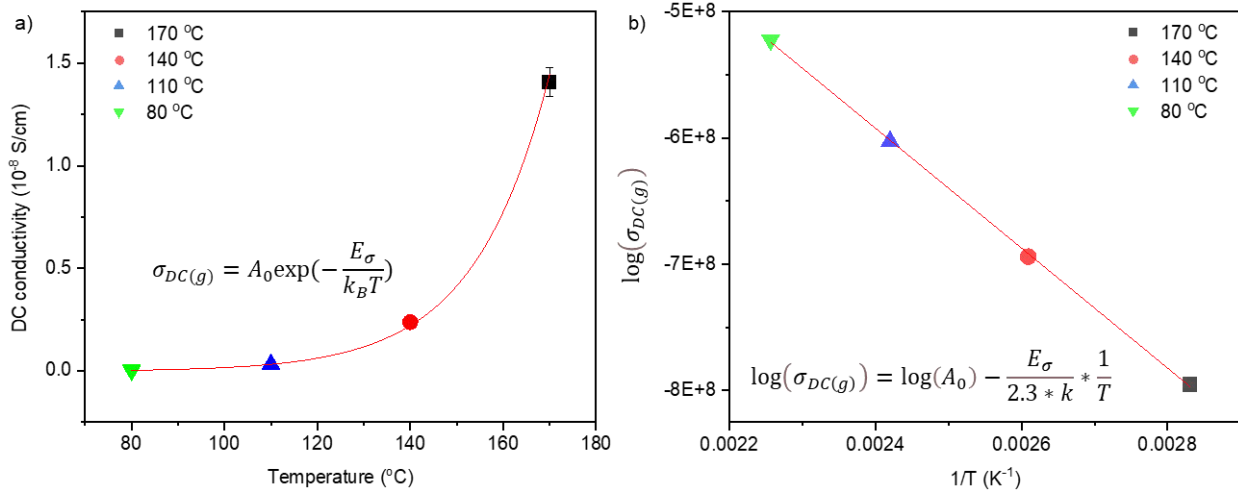
Figure 3-27 The plots of a) DC conductivity vs temperature of X-0 and b) $\log(\sigma_{DC(g)})$ VS *1/T*, along with red lines showing the fitting of data points by an exponential function and a linear function, respectively. The insert equations indicate the functions that data points follow.

3. 3. 6. 4 Conductivity and activation energy

The DC conductivity (**Figure 3-28**) and activation energy (**Figure 3-29**) of TNN glasses are calculated according to the *equivalent model* and *mathematical model* presented above. The DC conductivity of the TN-Cl remains nearly constant (variation < 0.1 magnitude) as the concentration of NaCl increases. Additionally, the activation energy shows a minor increment up to a maximum extent of 0.025 eV (Cl-12 versus X-0), which can also be regarded as unchanged. The conductivities of TN-Cl-Au and TN-Cl-ceramic are identical within the measurement uncertainty, but TN-Cl-ceramic glasses exhibit lower activation energy.

The TN-Br glasses with 2x < 16 have DC conductivity and activation energy close to those of TN-Cl glasses, and no significant variation of these parameters are observed. When the concentration

of NaBr increases above $2x > 16$, the DC conductivity appears to be slightly increased along with

a decrease of activation energy.
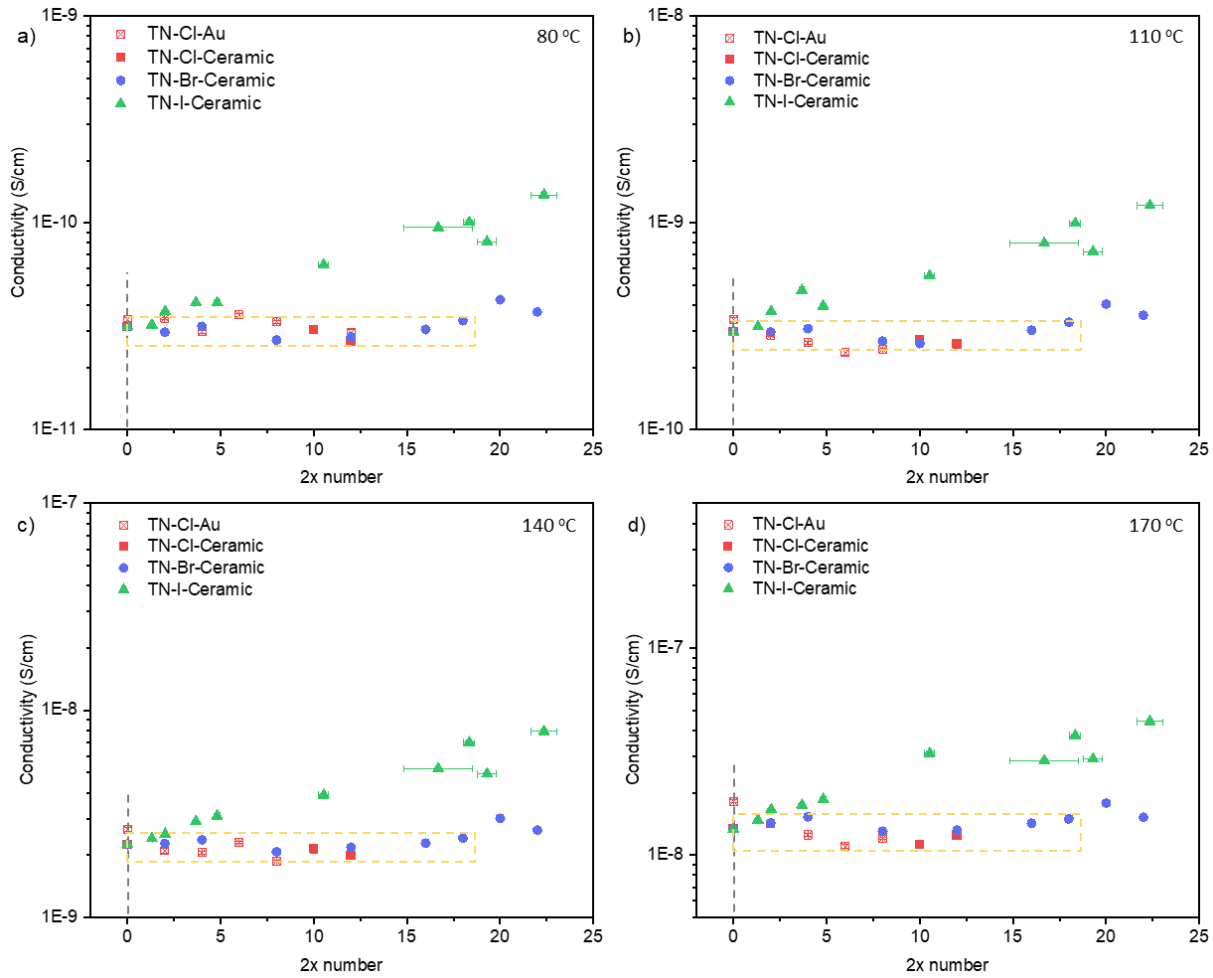
Figure 3-28 The DC conductivity (S/cm) of TNN glasses at a) 80 °C, b) 110 °C, c) 140 °C and d) 170 °C. The scale of y-axis is set to be 2 magnitudes for comparison and illustrating the enhancement of conductivity by raising NaX concentration. Error bars have been presented, however are not pronounced in diagrams since they are relatively small in this y-axis scale. The horizontal-shaded boxes indicate the values of conductivity that are regarded as roughly constant within the uncertainty.

The DC conductivity of TN-I glasses increases up to a maximum of 8 times as the concentration of NaI increases from $2x = 4$ to $2x = 22$. The conductivity of all TN-I glasses is higher than that of TN-Cl glasses. Furthermore, the TN-I glass with low NaI concentration (I-4) has a conductivity close to the TN-Br glass with high NaBr concentration (Br-20). The activation energy of specimens with $2x < 10$ remain constant, while those of samples with $2x > 10$ tend to decrease. Compared to the other samples (of TN-Cl, TN-Br and TN-I), the specimens I-17, I-18, I-19 and I-22 have discernibly lower activation energy (**Figure 3-29**). The explanation of the impact of halide on conductivity and activation energy will be provided in the below section.
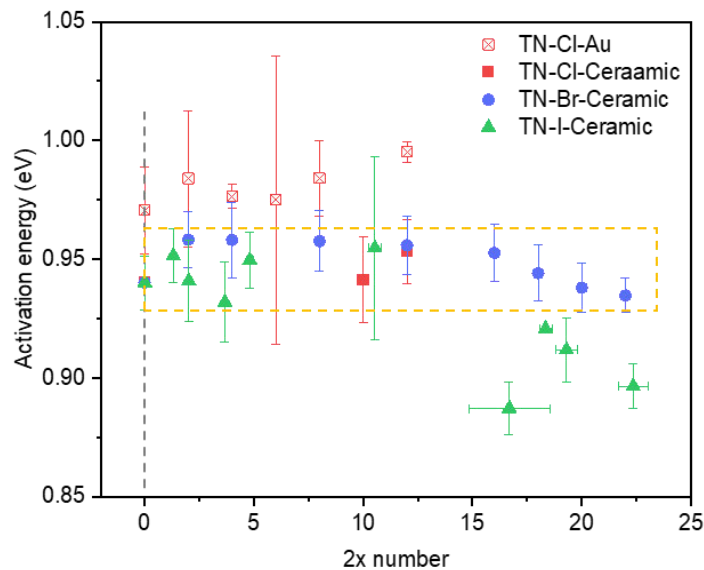
Figure 3-29 Plot of activation energy versus the 2x number of TNN system. The activation energy follows an order of TN-Cl > TN-Br > TN-I. The horizontal-shaded box indicates the values of activation energy that are regarded as roughly constant.

3. 3. 7 Correlating Raman spectra, free volume and conductivity

As mentioned in the literature review (section 3. 1. 1), the ionic conductivity (measured as DC conductivity) of a TNN glass is determined by the mobility and the concentration of MNIs. Specifically, a higher concentration and a higher mobility of MNIs benefit the conduction. In this research, the mobility of MNIs is evaluated by the free volume. The concentration of MNIs is not obtained directly, instead, is inferred from the measurement results (NBO concentration, free volume, DC conductivity).

As the discussion of the Raman spectra revealed (section 3. 3. 3), the introduced halides form Te-X bonds or exist as X^- ions in the interstitial sites. Specifically, the formation of Te-X is accompanied with the formation of Te-NBO, which compensates the reduction of Te-NBO caused by the decrease Na_2O concentration. Therefore, a lower NBO concentration means less Te-X bonds formed and more X^- ions. The DC conductivity depends on the concentration of MNI during IS measurement, which is determined by the concentration of X^- and $-NBO^-$ and the bonding energy between Na^+ and anions.

As the concentration of NaCl or NaBr increases, the free volume of TN-Cl and TN-Br glasses increase (**Table 3-8**), which benefits the enhancement of conductivity. However, the conductivity of TN-Cl and TN-Br glasses mostly (except for Br-20 and Br-22) remain constant, indicating the improvement of conductivity by the increase of the free volume is traded-off, most likely, by the decrease of MNI concentration. The increase of X^- ion concentration (indicated by the reduction of NBO concentration) also suggests the decrease of MNI concentration. The combination of increasing free volume and decreasing MNI concentration results in the nearly unchanged conductivity of TN-Cl and TN-Br glasses.

For the TN-I glasses, both the DC conductivity and free volume increase as the concentration of NaI increases. Compared to adding NaCl and NaBr, adding a small amount of NaI already results in the increase of conductivity, such as the conductivity of I-4 $\approx$ Br-20 (the highest conductivity of TN-Br glasses). And compared to the increase in conductivity, the increase of free volume is less significantly, e.g., the free volumes of I-4 $\approx$ Br-8. Therefore, in addition to increasing the free volume, the concentration of MNI is supposed to increase to achieve such obvious enhancement of conductivity. The MNI concentration increases during IS measurement is attributed to the low bonding energy between Na^+ and I^- ions.

Table 3-8 Summary of the variation of parameters that are related to the glass-structure and properties, including NBO concentration, free volume (V_{free}), DC conductivity (σ_{DC}), the amount of Te-X bond, X^- ion concentration (X^-), and mobile Na^+ concentration. The symbols plus (" + ") means increased, minus (" - ") means decreased, equal (" = ") means unchanged as the concentration of NaX increases. The numbers of symbols suggest the degree of corresponding variation. The "+" of σ_{DC} of TN-Br refers to the specimens Br-20 and Br-22 exhibit increase of conductivity compared to the other TN-Br glasses. The "mobile Na (IS)" refers to the mobile Na^+ concentration during IS measurement, where increasing the temperature (> room temperature) and external electric field applied.

	Measured			Inferred		
	NBO	V_{free}	σ_{DC}	Te-X	X^-	Mobile Na^+ (IS)
TN-Cl	-	+	=	+ + +	+	-
TN-Br	- -	+ +	= (+)	+ +	++	- -
TN-I	- - -	+ + +	+	+	+ + +	+ +

The conductivity of TNN glasses is not changed by the addition of NaCl or NaBr but increased to a maximum of about 5 times by adding NaI with 2x = 17. In comparison, the conductivity of $65B_2O_3$-$(35-x)Na_2O$-$xNaBr$ glasses increases about 4 times with x from 0 to 4, which means adding halides to TeO_2-based glass system causes a lower enhancement of the conductivity. It is

worth to note that, the halides in TeO_2-based glasses form Te-X bonds and exist as X^-, while all halides in B_2O_3-based glasses exist as X^-. Considering the formation of Te-X bonds is accompanied with forming Te-NBO bonds, more Te-X formed means larger amount of Te-NBO. Additionally, the energy to break the binding of Na^+ linked to NBO^- is higher than that to X^-, therefore, with the same concentration of halides, more Te-X formed means a higher energy is required to create MNIs, which results in lower enhancement of conductivity.

3. 4 Summary

In this report, I have elucidated the impacts of halide (NaCl, NaBr, NaI) on the properties of $68TeO_2$-$(32-x)Na_2O$-$x(NaX)_2$ glasses. The TN-Cl, TN-Br and TN-I glasses are inspected to be crystal-free and measured to be XRD amorphous when $2x < 12$, $2x < 22$, $2x < 22$, respectively, which indicates the glass forming regions. Within these glass forming regions, most of the TNN specimens (except for I-17~22) appear highly transparent in the visible range (400~700 nm).

As shown by the study of the Raman spectra, with the same molar concentration of NaX, the amount of Te-NBO bond follows the order TN-Cl > TN-Br > TN-I, while the concentration of Te-BO-Te linkage follows the order TN-Cl < TN-Br < TN-I. The amount of Te-NBO measured is affected in two aspects: i) the decrease of Te-NBO with decreasing Na_2O concentration, ii) and the increase of Te-NBO caused by the reaction X + Te-BO-Te = Te-X + T-NBO. The amount of Te-NBO following the order TN-Cl > TN-Br > TN-I suggests more Te-NBO bonds formed in TN-Cl than in the other glasses, which compensates the decrease of NBO caused by reducing the Na_2O concentration. The length of the Te-NBO bond decreases while that of the Te-BO bond increases. This is attributed to the halides inducing compulsive force to their adjacent Te-NBO bonds, which shortens the length of Te-NBO bonds but expand the overall network.

The density of the TNN glasses decreases as the concentration of NaX increases. According to the analysis of molar mass and molar volume, the decrease of the density is attributed to the increase of molar volume overwhelming the increase of molar mass. The free volume calculated from the molar volume and composition indicates expansion of the glass network by the large halide ions, which agrees with the observation of increased Te-BO bond length.

The *equivalent circuit $R_1/CPE-R_2/C_2$* and the *mathematical model* (layering-model) were applied to obtain the conductivity and activation energy of TNN glasses. The conductivity and activation energy of TN-Cl and TN-Br glasses appear to be independent of the NaX concentration, except for Br-20 and Br-22, whose conductivity slightly increases. The conductivity and activation energy of TN-I glasses increase as the concentration of NaX increases from 2x =4 to 22.

For TN-Cl and TN-Br glasses, the free volume increases but the conductivity remains constant, which indicates the decrease of mobile Na^+ ion concentration compensates the increase of the free volume. For the TN-I glasses, the conductivity is significantly enhanced by the addition of NaI. According to the comparison of conductivity and free volume of TN-Br and TN-I glasses, I hypothesize that the enhancement of the conductivity of TN-I glasses is not only attributed to the increase of free volume that increases the mobility of mobile ion, but also the increase of mobile Na^+ ion concentration.

Chapter 4 - Implications and Prospects

TZN transparent glass film

The TZN glass film with transparency approaching the theoretical limitation has been achieved based on the studies of chemistry mechanism of *NHSG* process. Based on the achievements of this research, I propose future research in two ways (mechanism and application);

1) Mechanism aspect: the transparency of a TZN glass film is determined by the *xerogel* structure which is affected by the heating-temperature, aging-time and atmosphere. The theory of structural evolution of the different steps of the *sol-gel* process was mainly developed based on the TG-DSC results. The quantification of the structural evolution of the *sol-gel* processes remains to be studied, e.g., measure the viscosity and particle (e.g., cluster or nanoparticle) size distribution using rheometer and dynamic light-scattering analysers, respectively, and correlate them with the preparation protocols. The optical properties, e.g., refractive index and dielectric constant, also remain to be measured. These proposed studies allow the adjustment of film properties based on the application, e.g., knowing the relationship between preparation protocol and particle size distribution allows controlling the degree of polymerisation.

2) Application aspect: the high refractive index and high transparency TZN glass film can be incorporated with fluorescent nanoparticles for optical application (e.g., LED light).

TNN ionic conductive glass

This research suggests that the halides are incorporated into the TeO_2-Na_2O glass in two ways: forming Te-X bonds and being located at interstitial sites as X^- ions, which was inferred based on changing of NBO and BO contents as measured by Raman spectroscopy. Since the Te-X bonds in TNN glasses cannot be directly measured by Raman spectroscopy, other spectroscopic technique (e.g., X-ray photoelectron spectroscopy) is required to directly observe the Te-X bond, which

allows the confirmation of forming Te-X bonds and the quantification of the proportion of Te-X bonds relative to X^- ions.

The Boson peak of TN-I glasses is shifted to lower frequency with increasing NaI concentration, while those of TN-Cl and TN-Br glasses remain constant as NaX concentration increases. The red-shift of the Boson peak suggests the fragility of TNN glasses increases as the NaI concentration increases. Considering the conductivity of TN-Cl and TN-Br is also independent of NaX concentration while that of TN-I increases with increasing NaI concentration, there might be a relationship between fragility and the conductivity of TNN glass system. I propose the fragility and conductivity are connected via the concentration or mobility of mobile Na^+ ions. This relationship can be a mechanistic understanding of the fragility and conductivity of glasses, which is worthy of a further study.

Supplementary

List of figures for supplementary

Supplementary for TZN *sol-gel* transparent film part

A1. Methods of synthesizing inorganic films

Inorganic thin films can be prepared using physical or chemical techniques [159]. The physical deposition, which is referred to the techniques using physical processes for thin film preparation, includes evaporation techniques (e.g. vacuum thermal evaporation [160] and electron beam evaporation [161]) and sputtering techniques (e.g. direct current sputtering [162] and radio frequency sputtering [163]). The chemical deposition techniques including chemical vapor deposition [164, 165], chemical bath deposition [166] and *sol-gel* method are the thin films preparation techniques that involve chemical reactions.

Although the thin films produced via physical techniques show excellent quality (e.g. high homogeneity), most of the physical techniques require expensive equipment and a large amount of target-materials [159]. In contrast, the chemical techniques provide the opportunity of synthesizing high quality inorganic thin films with a low cost. Among the most common chemical methods of preparing thin films, the *sol-gel* method has been widely applied due to the simplicity, compositional flexibility and capability of combining it with different nano-materials [167-169]. For example, the high index inorganic films (i.e. Al_2O_3, TiO_2, ZrO_2, TeO_2) as introduced above can all be synthesized via *sol-gel* method.

Commonly, the *sol-gel* method is referred to the hydrolytic *sol-gel* (HSG) method, which synthesizes inorganic thin films via the hydrolysis of metal-alkoxides, e.g. SiO_2 thin film prepared

from the hydrolysis of tetraethyl orthosilicate (TEOS) [170, 171]. The hydroxyl group offered by H_2O

is attached to the metal atom via the hydrolytic reaction (equation S1. 1) [171].

$$M(OR)_4 + H_2O \rightarrow HO\text{-}M(OR)_3 + ROH \qquad \text{S1. 1}$$

The reaction rate of hydrolysis is depended on the amount of water, the type of metal-alkoxide and

the catalyst. It may result in a full completion of hydrolysis (i.e. all OR groups are replaced by

OH), or stop as the metal is partially hydrolysed (e.g. $M(OR)_{4\text{-}n}(OH)_n$). Then the polymerization

occurs as the hydrolysed molecules are linked together via the condensation reaction (e.g. equation

S1. 2 and S1. 3).

$$(OR)_3M\text{-}OH + HO\text{-}M(OR)_3 \rightarrow (OR)_3M\text{-}O\text{-}M(OR)_3 + H_2O \qquad \text{S1. 2}$$

$$(OR)_3M\text{ -}OR + HO\text{-}M(OR)_3 \rightarrow (OR)_3M\text{-}O\text{-}M(OR)_3 + ROH \qquad \text{S1. 3}$$
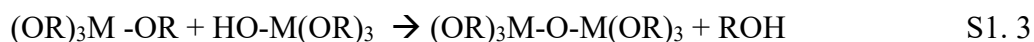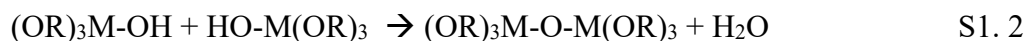
The polymerization reaction can be controlled via adjusting the amount of H_2O and the type of

catalyst, which allows the fabrication of inorganic materials with various morphologies (e.g.

particle, film and bulk).

A2. Supplementary figures for TZN glass thin film
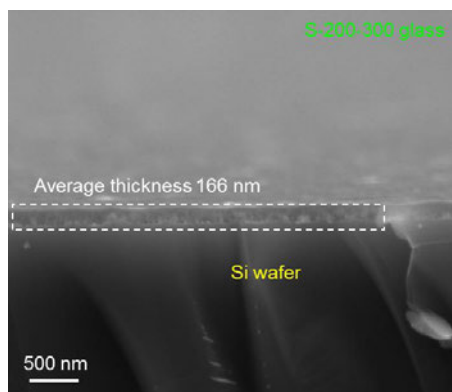
Figure S. 1 SEM images characterizing the cross-section of a coated film showing its average thickness is about 166 nm (S-200-300).
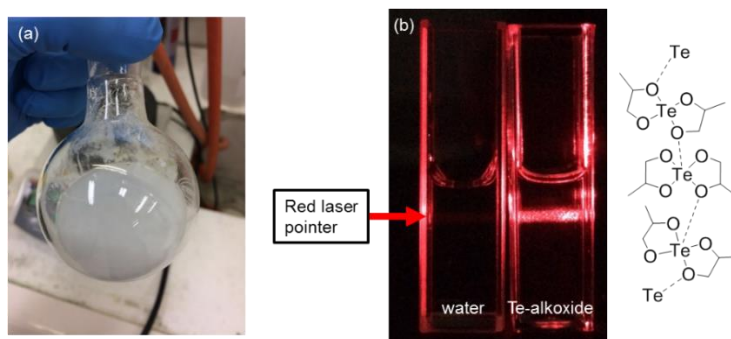
Figure S. 2 (a) At the stage of preparing Te-alkoxide, the resultant suspension mixture shows the sediment of white powder with interspersed black particles (metallic-Te). (b) The Te-alkoxide molecules linked via weak intermolecular bond (Te⋯O), showing light scattering under a red laser pointer. The reference water does not appear to show such scattering effect.
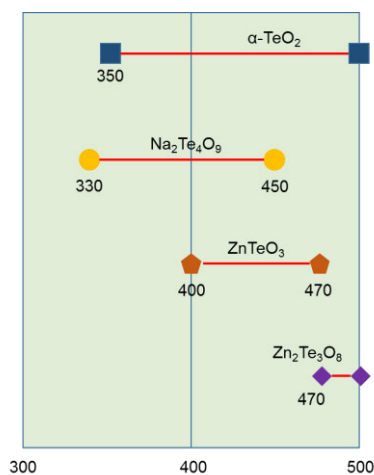
Figure S. 3 Schematic diagram illustrating the evolution of crystallizations (e.g., α-TeO_2, $Na_2Te_4O_9$, $ZnTeO_3$ and $Zn_2Te_3O_8$ crystals) in TeO_2-based samples from 300 to 500 ^{o}C. The data was summarized from references [52-54] and the experimental observation in this work. Note that $Na_2Te_4O_9$ crystal does not appear in our TZN film samples.

Polymerization reactions

As discussed in Section 3.3.2 and 3.3.3 of the main text, the *xerogel* network is formed via both addition and condensation polymerization.

- Schematics illustrating processes of addition polymerization, corresponding to discussion in section 3.3.2, are given below.
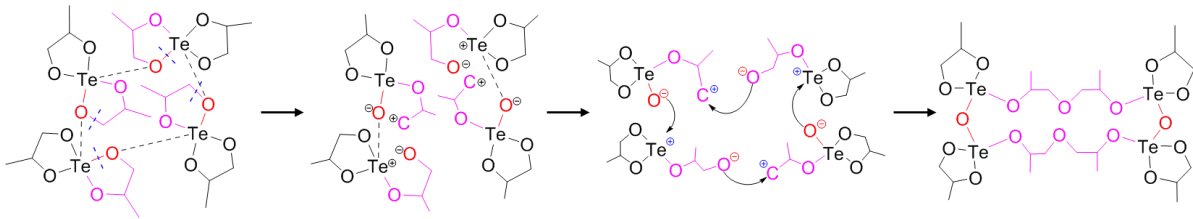
- Schematics illustrating processes of condensation polymerization, corresponding to discussion in section 3.3.2, are given below.

132
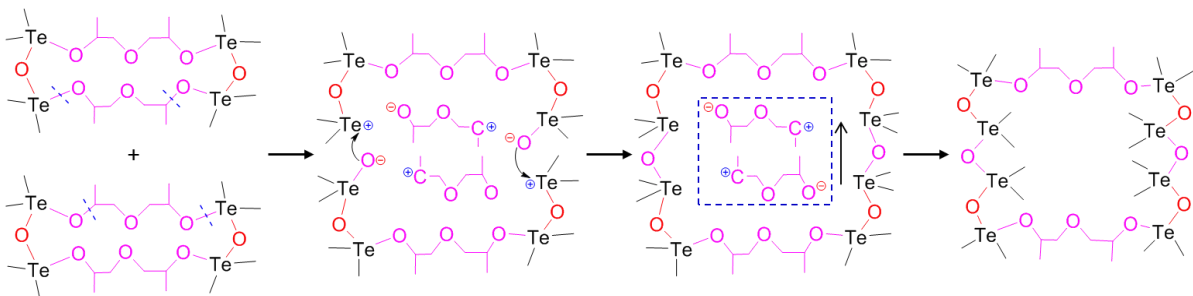
Calculation of the weight ratios of the different types of TeO₄ polyhedra in various *xerogels*

Table S. 1 summarizes the thermal analysis results (TG-DTG-DSC) of TZN *xerogels*, which were prepared using different aging time (F: 9 days, S: 30-60 days; M: 90 days; L: for 300 days) and different *sol* heating temperature (80, 130 and 150 ºC).

sample	region	temp range	DTG peak	DSC peak	Loss *wt%*	Normalized loss *wt%*	comment
Te-alkoxide	I	30-100	none	100 endo	1		no residual solvent/water
F-80	I	30-100	none	105 endo	4		residual solvent/water evaporation
M-80	I	30-100	none		3		residual solvent/water evaporation
L-80	I	30-100	none		1		no residual solvent/water
S-130	I	30-100	none	100 endo	3		residual solvent/water evaporation
F-150	I	30-100	none		0		no residual solvent/water
Te-alkoxide	II	100-250	245	245 endo	97	98	'P' polyhedra evaporation
F-80 *FTIR:*	II	100-250 *160-210*	218	219 endo	74	77	'P' polyhedra evaporation 'Aa' polyhedra decomposition
M-80	II	100-250	193	193 endo	20	21	'Aa' polyhedra decomposition
L-80	II	100-250	205	205 endo	10	10	'Aa' polyhedra decomposition
S-130	II	100-250	170	170 endo	23	24	'Aa' polyhedra decomposition
F-150	II	100-250		238 endo	1	1	'Aa' polyhedra decomposition
Te-alkoxide	III	none			0	0	no combustion
F-80	III	none			0	0	no combustion
M-80	III	250-300	268	273 exo	6	6	'Ao' polyhedral combustion
L-80	III	250-300	262	267 exo	8	8	'Ao' polyhedra combustion
S-130	III	250-300	286	286 exo	4	4	'Ao' polyhedral combustion
F-150 *FTIR:*	III	250-300 *220-300*	268	269 exo	8	8	'Ao' polyhedra combustion
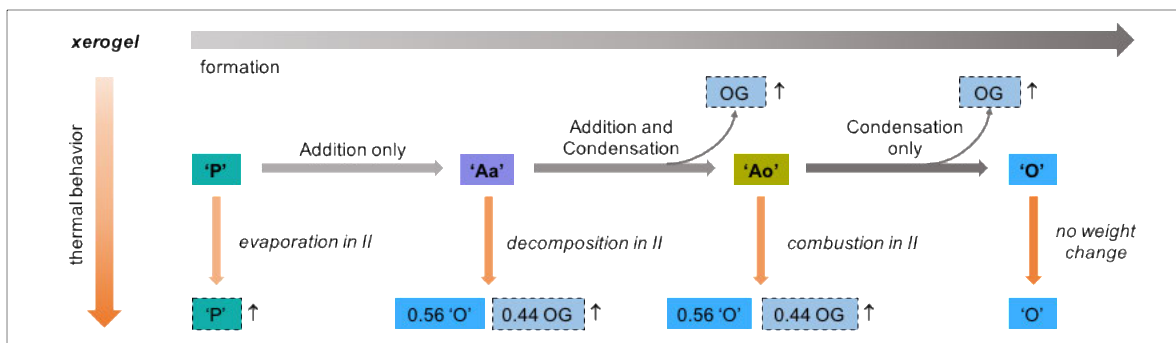
Figure S. 4 Silver-grey arrow indicating the evolution of [TeO$_4$] polyhedra of *xerogels* from 'P' polyhedron till 'O' polyhedron, in accompany with the release of OGs when condensation takes place. Orange-yellow arrow showing the respective thermal behaviour of the *xerogels* constituting various [TeO$_4$] polyhedra under different heating temperatures.

Weight loss data normalization (TG):

As shown in the TG-DTG-DSC curves in the main text (section 3.3.1), the weight losses (*wt*%) can be classified into three temperature regions (depicted by the Roman numerals: I, II, III) according to the different DTG peaks: evaporation of residual solvent in region I; evaporation of P polyhedra and decomposition of Aa polyhedra in region II; combustion of Ao polyhedra in region III.

To determine the weight ratios of the different polyhedra ('P', 'Aa', 'Ao', 'O'), the weight losses measured via TG analysis for region II (L_{II}) and III (L_{III}) are normalized to the total weight (W_{II+III}) in these regions given by $W_{II+III} = L_{II}+L_{III}+R_{III}$, where R_{III} is the weight remains at 300 ºC, i.e. $R_{III}=100-L_I-L_{II}-L_{II}$I. Accordingly, the normalized weight losses and weight remains in percentage are given by $Y/W_{II+III}\times100\%$, where Y is L_{II}, L_{III} or R_{III}. The normalized values are presented as "normalized loss *wt*%" column in Table S. 1.

Thermal behaviour of polyhedra:

The liberation of all OGs from the molar composition of 80Te-alkoxide–10Zn-acetate–20Na-acetate leads to the 80TeO$_2$–10ZnO–10Na$_2$O TZN glass, with a theoretical weight loss of 44% and weight remains of 56%. The detailed calculation is given as below:

The molar mass (g/mol):

Te-alkoxide	Zn-acetate	Na-acetate	TeO$_2$	ZnO	Na$_2$O
278	183	82	162	81	80

Thus the theoretical weight remain portion is:

$$R = 0.8 * \frac{162}{278} + 0.1 * \frac{81}{183} + 0.1 * \frac{80}{2 * 82} = 0.56 = 56\%$$

Thus the weight loss is L=44%.

According to the mass conservation law, the weight of the respective polyhedra (i = 'P', 'Aa', 'Ao', 'O') before the thermal analysis (X_i) is equivalent to the sum of the weight loss (L_i) and weight remains (R_i), i.e. $X_i = L_i + R_i$ measured after thermal analysis. According to the above calculation of weight loss fraction if all OGs are liberated, the ratio of weight loss (L, due to OGs liberation) to weight remains (R) is defined as L/R = 44/56.

As discussed in section 3.3.3, each polyhedron shows different thermal behaviour:

- 'P' polyhedra: They are evaporated with no weight remains, i.e. $X_p = L_p$.

- 'Aa' polyhedra: They have a high conformation mobility, and OGs are liberated from the alkoxy bridges via decomposition in region II, with L_{Aa}/R_{Aa}=44/56.

- 'Ao' polyhedra: Due to the low conformation mobility, OGs are liberated from the alkoxy bridges via combustion in region III, with L_{Ao}/R_{Ao}=44/56.

- 'O' polyhedra: The absence of alkoxy bridges in 'O' polyhedral make them show zero weight loss, i.e. $X_O=R_O$.

Accordingly, a set of equations can be built to calculate the respective weight ratios of the polyhedra:

'P': $X_P = L_P$, $R_P=0$,

'Aa': $X_{Aa} = 0.44\,X_{Aa} + 0.56\,X_{Aa}$, $L_{Aa}=0.44\,X_{Aa}$, $R_{Aa}=0.56\,X_{Aa}$

'Ao': $X_{Ao} = 0.44\,X_{Ao} + 0.56\,X_{Ao}$, $L_{Ao}=0.44\,X_{Ao}$, $R_{Ao}=0.56\,X_{Ao}$

'O': $X_O = R_O$, $L_O=0$

Thermal behaviours of xerogels composed of various polyhedra:

The DTG and DSC behaviour of the F-80 *xerogel* is highly similar to that of Te-alkoxide crystals (Fig. 4 and Fig. S5). Specifically, an endothermic DSC dip at ~105 $^{\circ}$C without DTG peak and an endothermic DSC dip with pronounced DTG peak at ~220 °C in region II have similar position and shape to the respective melting and evaporation peaks of Te-alkoxide crystals (Figure. S5). Furthermore, no weight loss is observed in region III. The total weight loss of 74% over 100-300 $^{\circ}$C is larger than the theoretical weight loss of 44%. The similarity to Te-alkoxide precursor crystals and the exceptionally large weight loss indicate the presence of Te-alkoxide precursor molecules (i.e. 'P' polyhedra) in F-80 *xerogel*. The presence of weight remains at 300 $^{\circ}$C indicates that the F-80 *xerogel* sample contains other polyhedra than 'P' polyhedra. According to the absence of the combustion DTG peak of region III, F-80 does not contain any 'Ao' polyhedra and hence no 'O' polyhedra. Thus, the weight remains can only be caused by the decomposition of the alkoxy bridges of 'Aa' polyhedra in region II. This allows calculation of the weight ratio of 'Aa' polyhedra from the weight remains. As the weight loss in region II is due to both the evaporation of 'P' polyhedra and the liberation of OGs from 'Aa' polyhedra alkoxy bridge, the weight ratio of 'P'

polyhedra is calculated from the region II weight loss and the weight ratio of 'Aa' polyhedra (calculated from the weight remains).

In contrast to F-80, the total weight loss in region II and III of the other *xerogel* samples (M/L-80, S-130, F-150) (Figure. 4b-e) is smaller than the theoretical weight loss of 44%. This suggests that these *xerogels* do not contain precursor molecules (i.e. no 'P' polyhedra) and their OGs have been partially liberated during the longer *sol*-aging time or higher *sol*-heating temperature via condensation reaction, leading to 'Ao' and 'O' polyhedra. The presence of 'Ao' polyhedra agrees with the observation of a combustion DTG peak for all these samples, while the presence of 'Aa' polyhedra is indicated by the decomposition DTG peak. The weight ratios of the 'Aa' and 'Ao' polyhedra is calculated from the measured weight loss in regions II and III corresponding to the liberation of OGs from 'Aa' and 'Ao' polyhedra, respectively. The weight ratio of the 'O' polyhedra is then calculated from the measured weight remains taking into account the weight remains of 'Aa' and 'Ao' polyhedra calculated from their weight ratios.

Based on the above discussion on thermal behaviours of different *xerogels*, we established the equations for the weight ratios of the 4 types of polyhedra in different *xerogels* as follow:

Xerogel	Polyhedra	Equations
F-80	'P'; 'Aa'	$L_{II} = X_P + 0.44\ X_{Aa}$
		$R_{III} = 0.56\ X_{Aa}$
		$R_{III} = 100 - L_{II} - L_{III}$
M-80		$L_{II} = 0.44\ X_{Aa}$
S-130		$L_{III} = 0.44\ X_{Ao}$
L-80	'Aa', 'Ao', 'O'	$R_{III} = 0.56\ X_{Aa} + 0.56\ X_{Ao} + 1\ X_O$
F-150		$R_{III} = 100 - L_{II} - L_{III}$

These equations can be readily solved to derive the values of X_{Aa}, X_{Ao} and X_O of different *xerogels* (as given in Table S2), according to the measured weight loss (Table S1 normalized loss *wt*% column) in region II (L_{II}) and region III (L_{III}):

Table S. 2 The calculated weight ratios of the 'P', 'Aa', 'Ao' and 'O 'polyhedra in different *xerogel*s.

Sample code	'P' polyhedra (%)	'Aa' polyhedra (%)	'Ao' polyhedra (%)	'O' polyhedra (%)
F-80	59	41		
S-130		54	9	37
M-80		47	14	39
L-80		23	18	59
F-150		2	18	80
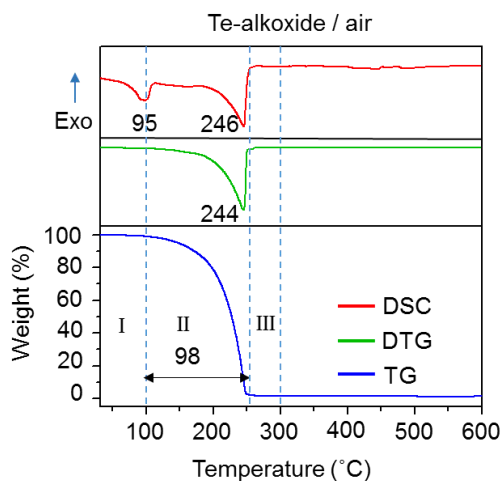
Figure S. 5 TG-DTG-DSC analysis of as-prepared Te-alkoxide molecules from room temperature to 600 ºC with a rate of 10 ºC/min under air flow of 3 L/min. Note that the numerical values of DTG and DSC curve indicate the dip temperatures in the regions of I and II. The 95 in DSC corresponds to the melting temperature of Te-alkoxide, while the 246 in DSC and 244 in DTG indicate the evaporation of Te-alkoxide. The number of 98 above the horizontal arrows at the bottom TG curve panel represent *wt*% loss in regions II.
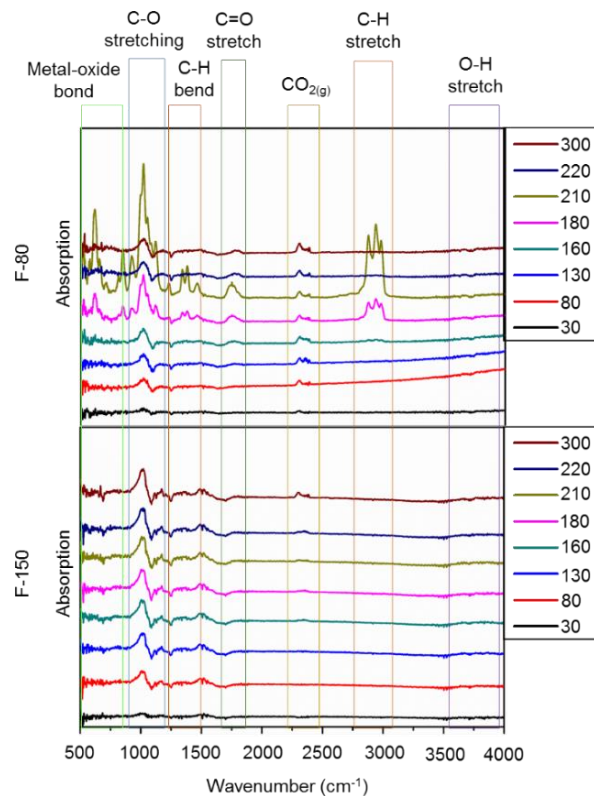
Figure S. 6 Vapor-FTIR spectroscopic analysis of F-80 and F-150 *xerogels* samples. By heating these samples from 30 to 300 °C in air, the variations of the discharged compounds with different bonds in the vapor were monitored, as indicated by the different colour frames.
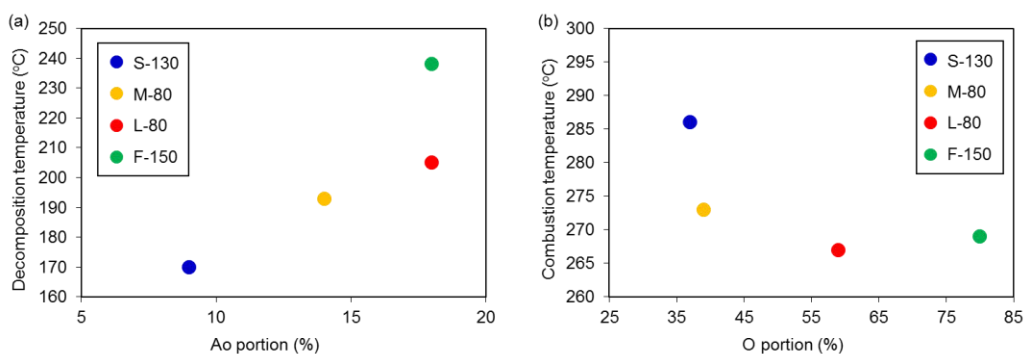
Figure S. 7 The variations of decomposition and combustion temperatures as a function of the portions of (a) 'Ao' polyhedra and (b) 'O' polyhedra in different *xerogels* samples, respectively. The different color dots indicate various *xerogels*: blue for S-130, yellow for M-80, red for L-80 and organe for F-150. The trend clearly suggests that, in (a), larger portion of 'Ao' polyhedra results in increased decomposition temperature due to the enhanced network around polyhedra, and in (b), increased portion of 'O' polyhedra requires lower combustion temperature due to less organic groups.

139

Theoretical transmission of 75TeO$_2$-15ZnO-10Na$_2$O thin film on coverslip

To determine the theoretical transmission of 75TeO$_2$-15ZnO-10Na$_2$O coating on coverslip, the Fresnel reflection at multiple interfaces and the UV-edge absorbance of coverslip were considered. The refractive index n of coverslip (i.e. D 263^{TM} T glass) was simulated according to Sellmeier equation [172]:

$$n^2 = A + B_1\left(\frac{\lambda^2}{\lambda^2 - C_1}\right) + B_2\left(\frac{\lambda^2}{\lambda^2 - C_2}\right) + B_3\left(\frac{\lambda^2}{\lambda^2 - C_3}\right)$$

where A, B$_1$, B$_2$, B$_3$, C$_1$, C$_2$ and C$_3$ are A=1, B$_1$=1.23795755, B$_2$=0.0466469, B$_3$=2.4670056, C$_1$=0.0086308, C$_2$=0.0469075, C$_3$=264.1463 and λ is the wavelength.

The simulated refractive index data of the 75TeO$_2$-15ZnO-10Na$_2$O was adopted from Zhao's *et. al.* [21].

The reflection R can be calculated via:

$$R = (\frac{n_1 - n_2}{n^1 + n^2})^2$$

Thus, the reflection of air/TZN glass interface is:

$$R_1 = \left(\frac{n_g - n_a}{n_g + n_a}\right)^2$$

The reflection of TZN/coverslip interface is:

$$R_2 = \left(\frac{n_g - n_c}{n_g + n_c}\right)^2$$

The reflection of coverslip/air interface is:

$$R_3 = \left(\frac{n_c - n_a}{n_c + n_a}\right)^2$$

where, n_g, n_a, and n_c is the refractive index of TZN glass, air and coverslip, respectively.

The transmission due to the Fresnel reflection taking placing at multiple interfaces is expressed by:

$$T_F = (1 - R_1) * (1 - R_2) * (1 - R_3)$$

The corresponding absorbance caused by this Fresnel reflection is written as:

$$Abs_F = -log_{10}(T_F)$$

For an uncoated blank coverslip, its absorbance is given as:

$$Abs_C = -log_{10}(T_C)$$

where $T_C = (1 - R_3)^2$, equivalent to the twice Fresnel reflection at air-coverslip interface.

In addition to Fresnel reflection, the coverslip has a UV-edge absorbance, given by:

$$Abs_{C(edge)} = Abs_C - Abs_{C(mes)}$$

where $Abs_{C(mes)}$ is the measured Absorbance of coverslip used.

Taking into account the combined contribution by Fresnel reflection of the coated film and the intrinsic absorbance of the coverslip, the theoretical absorbance of $75TeO_2$-$15ZnO$-$10Na_2O$ thin film on coverslip can be calculated as:

$$Abs_{TZN\ on\ coverslip} = Abs_{C(edge)} + Abs_F$$

As such, the theoretical transmission (%), converted from the theoretical absorbance above, can be written as:

$$T_{TZN\ on\ coverslip} = 10^{2 - Abs_{TZN\ on\ coverslip}}$$

Supplementary for TNN ionic conductive bulk glass part

B1. Introduction of background knowledge

B1.1. Transparent-semiconductive materials

The development of novel optical-electrical devices, such as transparent solar panels [35], touch screens [36] and bio-probes for optogenetics [37], has been considered as the solution to some practical challenges. Robust solid transparent conductive materials (STCMs) is the primary building block of the novel optical-electrical devices [34]. The STCMs developed previously can be categorised based on their conduction dynamic, i.e. ionic conduction or electronic conduction, specifically, including transparent conductive glasses (TCGs) [63, 173-175] that are based on ionic conduction, and transparent conductive oxides (TCOs) [176-178], conductors-embedded insulators (CEIs) [36, 179-182] and transparent conductive polymers (TCPs) [183, 184], which are all based on electronic conduction. The electronic conductive transparent materials have been extensively investigated and applied, e.g. the Tin-doped In_2O_3 (ITO) thin film has been widely used on the touch screens of electronic devices. Although the conductivity of those electronic conductive materials is promising, their relatively low transparencies become the critical obstacle for the applications which require mm-scale (e.g. bulk/fibrous material) transparency, i.e. they are only transparent in nm- or µm-scale, which just allows them to be used in the form of coating or thin film.

B1.2. Electronic conductive mechanisms and its correlation to transparency

Electronic conduction is referred to the movement of the electrons by the applied of external electric field [185-187]. According to the bandgap theory (**Figure S. 8**), materials can be categorised as conductor, semi-conductor and insulator according to their conductivity and bandgaps. The

conduction and valence bands of a conductor (e.g. metal) overlap, which enables the electrons being promoted freely from the valence band to the conduction band and resulting in a high conductivity of $> 10^5$ S/m. When the valence band and conduction band are slightly separated (i.e. bandgap < 4 eV), extra energy, which depends on the bandgap value, is required to excite the electrons from valence band to conduction band, and for those semi-conductive materials, the conductivity is 10^{-6} S/m to 10^5 S/m. In an insulator, the valence band and conduction are further separated (i.e. bandgap > 4 eV) [188], thus a higher amount of extra energy is required to excite the electrons from valence band to conduction band, consequently results in the low conductivity of $< 10^{-6}$ S/m.

The Drude model is used to explain the conductivity of materials by discussing the movement of electrons in materials. According to the Drude model, the relationship between current density **J** and the electric field **E** can be expressed as [176]:

$$\boldsymbol{J} = e^2 \tau \left(\frac{n}{m^*}\right) \boldsymbol{E}.$$

And the factor $e^2\tau(n/m^*)$ is referred to as Drude Direct Current (DC) conductivity σ_0. i.e.

$$\sigma_0 = e^2\tau(n/m^*)$$

where e is the elemental charge, n is the free carrier concentration, τ is the permitted scattering time, which is referred to the mean time of travel of electrons before they are scattered by atoms or other electrons, and m^* is the effective carrier mass, which is referred to the total mass of electrons that are correlated with each other. As indicated, the conductivity is dominated by τ, n and m^*.

According to the bandgap theory and Drude model, to achieve a high electronic conduction the material should have:

  1) a small bandgap with the Fermi level crossing the conduction band.

2) a long scattering time (τ), which means free electrons have a longer traveling distance; higher order of crystallization is in favour of a longer scattering time.

3) a high carrier concentration.

4) a lower effective carrier mass, i.e. less correlation between electrons.
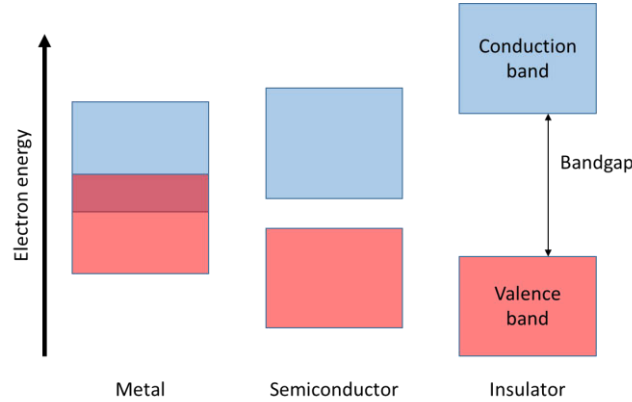
Figure S. 8 Schematic diagram of bandgap structures of metal, semiconductor and insulator.

Besides a high conductivity, high transparency is also a target of this project. The transparency is affected by 1) absorption [189]; 2) light scattering, e.g. by particles and defects [190]; and 3) light reflected at interfaces, i.e. Fresnel reflection [191]. In an ideal non-nanoscale bulk material (without dopant, impurity and defect), the absorption originates from the *bandgap*, and the *typical plasma oscillations* (for metals and semiconductors) [192].

Only the light with the energy lower than the bandgap of a material can propagate through it. Therefore, to be fully transparent in visible range (i.e. 400 nm to 700 nm), the bandgap should be larger than 3.1 eV (i.e. the energy corresponding to the 400 nm light) [176]. As been mentioned above, the bandgap also determines the electronic conductivity, which should be at least lower than 4.0 eV to be semi-conductive. Thus, the bandgap of STCMs should be between 3.1 eV to 4.0 eV, where a lower bandgap corresponds to a higher conductivity but lower transparency.

The plasma oscillation of conducting and semiconducting materials refers to the rapid oscillating motion of conduction electrons around the atoms. The dielectric function is given to express the plasma oscillation of electrons [193, 194]. When the incident light is within ultraviolet to visible ranges, the dielectric function is:

$$\varepsilon(\omega) = \varepsilon_L \left(1 - \frac{\omega_p^2}{\omega^2} \right).$$

And in the equilibrium position, the complex refractive index is [195]:

$$N(\omega)' = \sqrt{\varepsilon(\omega)} = n(\omega)' + ik(\omega).$$

The *plasma frequency* can be expressed as:

$$\omega_p^2 = \frac{4\pi n e^2}{\varepsilon_L m^*}.$$

And the reflectivity:

$$R = \frac{(1 - n')^2 + k^2}{(1 + n')^2 + k^2}$$

where ε_L is the dielectric constant (refers to the charges of electrons that bound to equilibrium positions), ω_p is the plasma frequency, n' is the refractive index, k is the extinction coefficient, n is the mobile carrier concentration, and m^* is the effective carrier mass. Accordingly, when the incident light with a frequency $\omega > \omega_p$, then $\varepsilon > 0$, hence, $k(\omega) = 0$. When $\omega < \omega_p$, then $\varepsilon < 0$, and consequently, $n'(\omega) = 0$, i.e. exhibits total reflection (reflectivity $R = 1$). Thus, in equilibrium condition, the conductive materials are only transparent to visible light with frequencies that are higher than the plasma frequency ($\omega > \omega_p$).

To be transparent in the visible range (400 to 700 nm), the conductive materials should have a plasma frequency ≤ 1.7 eV (e.g. ITO, $\omega_p \approx 1.0$ eV). As indicated, when the electronic conductivity is increased via the increase of n/m^* (the ratio of mobile carriers), the plasma frequency will

increase simultaneously, and consequently, the reflectivity increases. Accordingly, the transparency and electronic conductivity cannot be increased simultaneously via enhancing the carrier concentration. In addition, the transparency and electronic conductivity are also contradictory in terms of bandgap, i.e. a larger bandgap is benefit to transparency but is harmful to the electronic conductivity. Therefore, it is a trade-off between electronic conductivity and transparency, the aim of achieving thick transparent conductor based electronic conduction becomes challenging.

B1.3. Models of glass ionic conduction

Among the ionic conductive materials, the ionic conductive glass [63, 173-175] has been found to be a promising candidate for transparent ionic conductor due to its outstanding physical properties, e.g. the relatively higher transparency (compared to solid-state electrolyte) and the relatively higher thermal resistivity (compared to ionic conductive polymer). The structure of non-metallic inorganic glasses is commonly described by the Zachariasen's network hypothesis, where the backbone of the glass is constructed by the interconnected (corner-sharing) metal-oxide polyhedra (i.e. glass former), and a secondary cation species (i.e. glass modifier) which disrupts the covalently linking glass network and introduces free mobile ions [6, 175]. Depending on the different types of glass modifiers being introduced, the cluster model and diffusion pathway model are commonly proposed to explain the dynamic mechanism of ionic conduction in glass systems.

1) The cluster model [196, 197] is proposed based on the assumption that, the metal salt introduced to the glass system have a structure similar to its crystal structure within micro-domain (e.g. size ~ 10 angstrom). Thus, the conduction dynamic of those metal salt dopants is similar to that of their crystalline phase. This model is particularly used to explain the high ionic conductivity of AgI

doped glass systems, where the AgI is proposed to remain in crystalline α-AgI cluster, i.e. one of the best ionic conductors.

2) In the diffusion pathway model [198], the ionic conduction takes place within the connected conduction pathway. Those internal pathways were assumed to be formed by the anions of the dopant salt and/or the glass network. Ideally, the doping salt is proposed to expand the network, which leads to an increase in the conduction pathways.

Besides those two models, other models (e.g. the electrolyte model [199] and random site model [200]) are also proposed to explain the ionic conduction in glass systems. Even if those models are distinctly different in the details (e.g. the effects of dopant salt in conduction), they all established share the same structural assumption, where the glass is homogeneous down to a micro-scale of few angstrom. The ionic conduction is accomplished via the hopping of mobile ions through the available sites of the immobile disordered structure. Based on such common assumption, the ionic conductivity of glasses can benefit from [175]:

1) having mobile ions (mostly cations), which are normally introduced by the metal-oxide modifiers or metal salt dopants.

2) containing anions with high polarizability (i.e. the tendency of being distorted), e.g. Cl^-, Br^- and I^-, and cations with a strong polarization power (i.e. the ability to distort anion), e.g. Li^+ and Na^+.

3) having multiple glass formers [72, 201] and only one mobile ions donor [202]. This condition has been experimentally demonstrated but the mechanisms of those phenomena are not well understood yet.

B1.4. Typical ionic conductive glasses

According to the review of Lothar Wondraczek et al. (2020) [38], some typical ionic glasses are the most prominent superionic conductors, e.g. halide glasses (e.g. ZnCl glass system), borate glasses (e.g. $NaCl-Na_2O-B_2O_3$), phosphate glasses (e.g. $AgI-Ag_2O-P_2O_5$) and some glass-forming sulfides (e.g. $Ag_2S-GeS-GeS_2$), where the large amount of dopants such as silver, lithium, copper or sodium ions are acting as charge carriers [203, 204]. In this section, the AgI-based conductive glasses [205] and Li+ or Na+ ionic conductive glasses [206] will be introduced.

As explained by the cluster model, the α-AgI clusters conduct electric in AgI-based glass system. The α-AgI crystal [205], which is stable above 147 °C, has 42 available sites in its crystalline structure for the motions of Ag^+ ions. As the AgI being incorporated with some glass matrices (e.g. phosphate), the α-AgI can be stabilized at room temperature as nano-cluster [207]. According to the explanation of diffusion pathway model, the coexistence of two types of anion (i.e. iodide and oxide) reduces the potential energy, thus increase the conductivity [208]. The weak coordination between Ag^+ and I^- ions further ensures the mobility of Ag^+ ions in glass networks, which results in a theoretical superionic conduction of 1 S/cm. In 2017, Rioux et al. reported the synthesis of $AgI-AgPO_3-WO_3$ and investigated its optical and electrical properties [209]. Typically, at room temperature, a 5mm thick glass displays a conductivity of about 10^{-2} S/cm (45 mol% AgI) and has a transmission of about 60% at 550 nm to 700 nm (cut-off wavelength at about 500 nm), which gives the material colour. The colouration is explained as, the I^- ions introduced by AgI react with WO_3, consequently, result in coloured species (W_xI_y).

In addition to the superionic glass containing AgI, the Li^+ and Na^+ ions have also been introduced as charge carriers in glass or glass-ceramic conducting materials due to the relatively small sizes of Li^+ and Na^+ ions, which allows a high mobility in glass networks. The strong polarization power

of Li^+ and Na^+ ions further enhance their performance as charge carriers. The conductivity of glass or glass ceramic containing Li^+ or Na^+ ions reach the level of 10^{-3} S/cm at room temperature [63, 210, 211]. The Li^+ or Na^+ ions are introduced as oxide or sulfide components (e.g. Li_2O, Na_2O or Li_2S), which commonly play a role as a network modifier in glass systems, i.e. the Li^+ or Na^+ ions do not form the glass network but locate in the free space of the glass matrix. A recent paper investigated the dynamics of Li^+ ion conduction (Li_2S–Ga_2Se_3–$GeSe_2$ glass system) based on the diffusion pathway model [63], wherein the concept of "successful hop" is raised to describe the diffusion of ions with sufficient energy to overcome the percolation barrier so that the ions can move through a long distance. Such "successful hop" was related to the distances between Li sites, specifically, as the concentration of Li components increased, the required energy for a "successful hop" is decreased. However, when the concentration of Li compounds reaches a certain level, a static percolation path will form, after which the increase of Li components concentration no longer significantly improves conductivity. It suggests that finding the optimized concentration of Li component is important for designing a Li^+ ion conductive glass system. Based on my knowledge, the sulphide glasses normally exhibit yellow to red colour [212], therefore, this research is focused on the oxide glass system considering the aim of high transparency.

B2. Appendix figures for TNN bulk glass project

B2.1. Experimental section

Figure S. 9 The photos of TN-I glass in crucible right removed from the melting oven, showing the evaporation of purple gas.

Table S. 3 EPMA setup for analysis of glass

Element and Line	Diffracting Crystal (Sp#)	Background type/fit	kV /nA / spot size(μm)	Peak Count Time	Bkgd Count Times		# bkgd points acquired (Lo/Hi)	Standards*		Overlapping element and order	Average DL (99% CI) on sample (ppm)
					Lo	Hi		Primary Standard	Interference Standards		
Te La	LPET (3)	MAN	15/20/20	20	-	-	MAN	553			240
Na Ka	TAP (4)	MAN	15/20/20	20	-	-	MAN	1338			220
I La	LPET (5)	MAN	15/20/20	20	-	-	MAN	509	560	Te Lb (I)	250

Table S. 4 Standard information.

Reference #	Mineral composition	Natural/Synthetic	Manufacturer
509	Thallium Bromide/Iodide	Synthetic	Astimex
513	Celestine	Synthetic	Astimex
547	Zirconia	Synthetic	Astimex
553	Antimony Telluride	Synthetic	Astimex
557	Rhodonite	Natural	Astimex
558	Wollastonite	Natural	P&H and Associates
559	Rutile	Synthetic	P&H and Associates
560	Silver Telluride	Synthetic	P&H and Associates
564	Sphalerite	Synthetic	P&H and Associates
575	Corundum	Synthetic	P&H and Associates
576	Periclase	Synthetic	P&H and Associates
578	Specularite	Synthetic	P&H and Associates
587	Tellurium metal	Synthetic	Astimex
735	Albite (Amelia)	Natural	C.M. Taylor
736	Apatite (Wilbeforce)	Natural	C.M. Taylor
1338	NMNH 117218-1 Corning glass B	Synthetic	Smithsonian
1600	MgF2	Synthetic	In-house (Laser optic)

Table S. 5 The collected EPMA raw data.

	Te (wt%)	Na (wt%)	I (wt%)
	66.01	10.46	
	65.35	10.63	
	64.99	11.12	
	63.94	13.90	
X-0	62.31	14.11	
	63.41	14.34	
	64.33	14.04	
	64.91	14.28	
	64.42	14.27	
	64.36	12.48	

	63.03	10.56	1.25
	62.57	9.96	1.21
	63.21	11.08	1.24
	63.63	10.90	1.23
I-1	63.76	10.77	1.32
	64.24	11.42	1.28
	63.70	11.45	1.19
	63.10	11.55	1.23
	62.93	10.57	1.17
	64.01	10.94	1.27
	63.97	11.35	1.84
	63.76	12.03	1.93
	64.08	12.51	1.92
	63.27	11.32	2.03
I-2	64.31	12.76	1.92
	63.43	10.86	1.87
	63.76	11.33	1.83
	64.33	12.08	1.77
	63.12	10.50	1.82
	63.66	12.40	1.85
	60.79	8.99	3.20
	59.65	9.39	3.13
	61.44	9.34	3.21
	61.20	9.51	3.16
I-4	60.18	8.93	3.18
	62.07	10.24	3.23
	62.49	11.18	3.21
	62.65	9.89	3.18
	63.11	11.11	3.38
	63.04	11.39	3.38
	61.22	9.24	3.91
I-5	63.42	9.74	4.47
	62.33	10.06	4.36

	62.56	9.62	4.40
	62.26	10.00	4.43
	62.74	10.38	4.47
	61.88	9.57	4.31
	62.49	9.85	4.38
	62.88	10.15	4.50
	62.17	10.12	4.07
I-11	59.28	9.28	8.62
	61.05	8.80	9.04
	60.43	8.99	9.08
	60.68	8.64	8.97
	59.45	8.62	8.82
	61.49	10.37	8.93
	60.34	9.51	8.76
	60.02	8.73	8.89
	59.93	8.83	8.92
	60.41	8.75	9.07
I-17	56.75	8.70	10.42
	55.04	7.85	11.70
	55.17	7.76	12.60
	55.75	7.41	12.86
	54.78	7.75	13.09
	56.33	6.71	11.07
	56.24	8.78	13.09
	54.70	8.96	14.75
	54.68	8.29	14.67
	55.34	8.61	15.29
I-18	54.76	9.07	14.78

	54.55	9.97	14.56
	54.86	9.52	14.88
	55.31	10.12	14.84
	54.28	8.68	14.25
	54.78	9.34	14.52
	54.99	8.88	14.51
	55.03	9.12	14.71
	54.92	9.65	14.92
	54.51	8.99	14.89
	57.00	9.16	14.82
	56.20	8.36	15.14
	56.83	8.23	15.02
	56.57	8.56	15.16
I-19	56.76	8.31	15.46
	56.32	8.28	15.46
	56.40	8.33	15.57
	56.74	7.79	15.53
	56.38	7.99	15.30
	55.95	7.85	15.40

Converting the wt% of elements to mol% of molecules.

For the specimens having NaI, the wt% of Na is contributed from Na_2O and NaI. The ratio of NaI is calculated using:

$$NaI_{mol} = \frac{I_{wt\%}}{M_I}$$

The M_I is the molar mass of iodine. The ratio of TeO_2 can be calculated according to:

$$TeO_{2\ mol} = \frac{Te_{wt\%}}{M_{Te}}$$

The M_{Te} is the molar mass of tellurium. The mol% of Na occupied by Na_2O can be obtained from:

$$Na_{mol}(Na_2O) = \frac{Na_{wt\%}}{M_{Na}} - \frac{I_{wt\%}}{M_I}$$

Then the ratio of Na_2O is obtained from:

$$Na_2O_{mol} = \frac{Na_{mol}(Na_2O)}{2}$$

Via normalizing the ratio of TeO_2, Na_2O and NaI to 100, the mol% of them can be acquired.

B2.2. UV-vis analysis
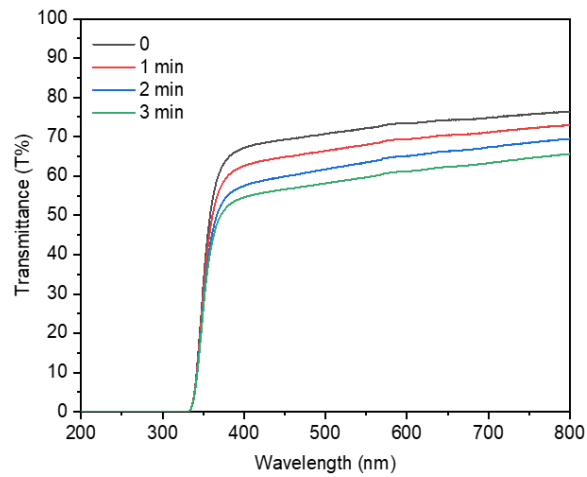
Figure S. 10 The transmittance spectra of a Cl-12-Au glass (right after polishing) measured continuously within 3 mins.
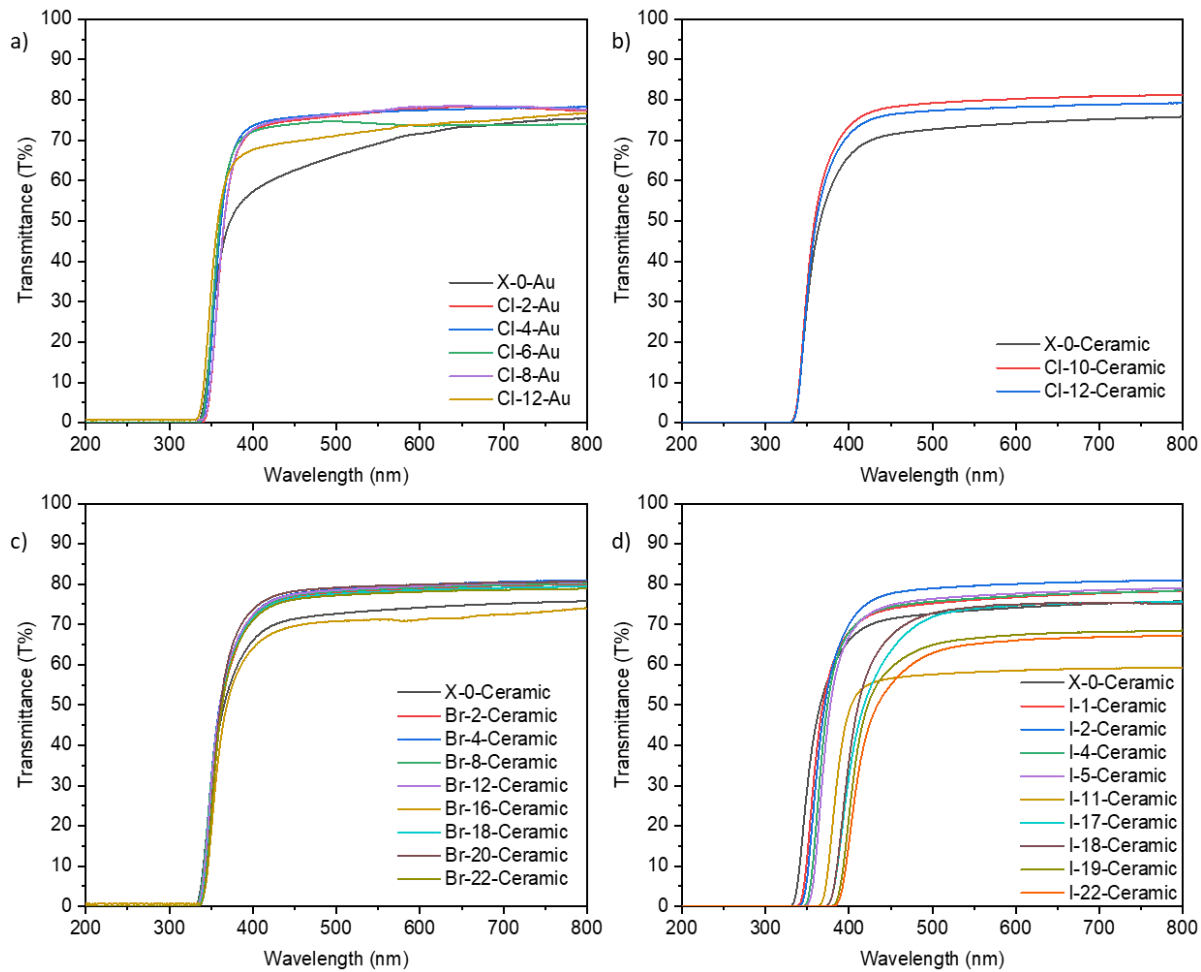
Figure S. 11 Raw data of transmission spectra.
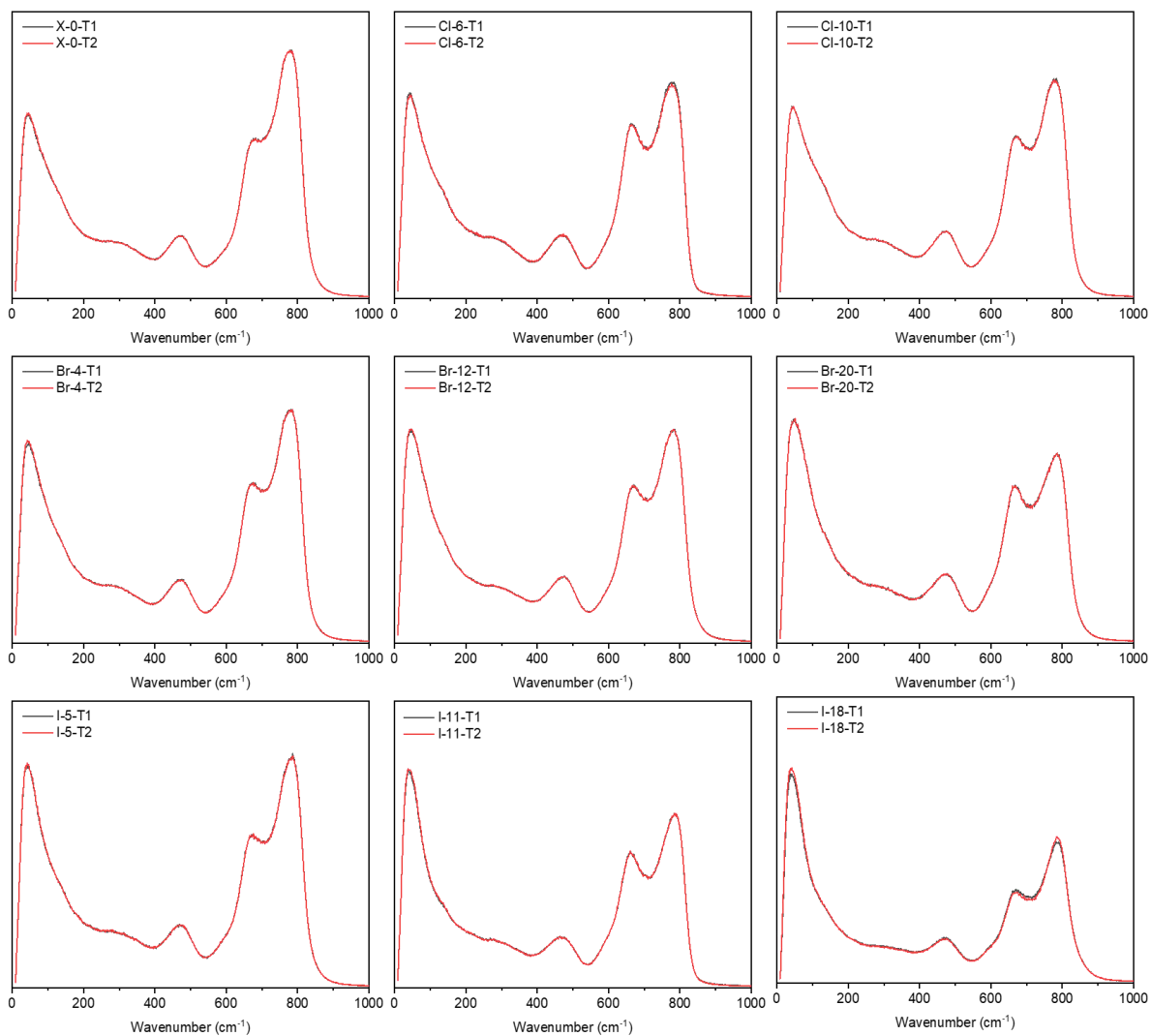
Figure S. 12 Several Raman spectra examples of two tests collected from two spots. The highly overlapping of two spectra suggests the consistency of the surface in respect to the Raman analysis.
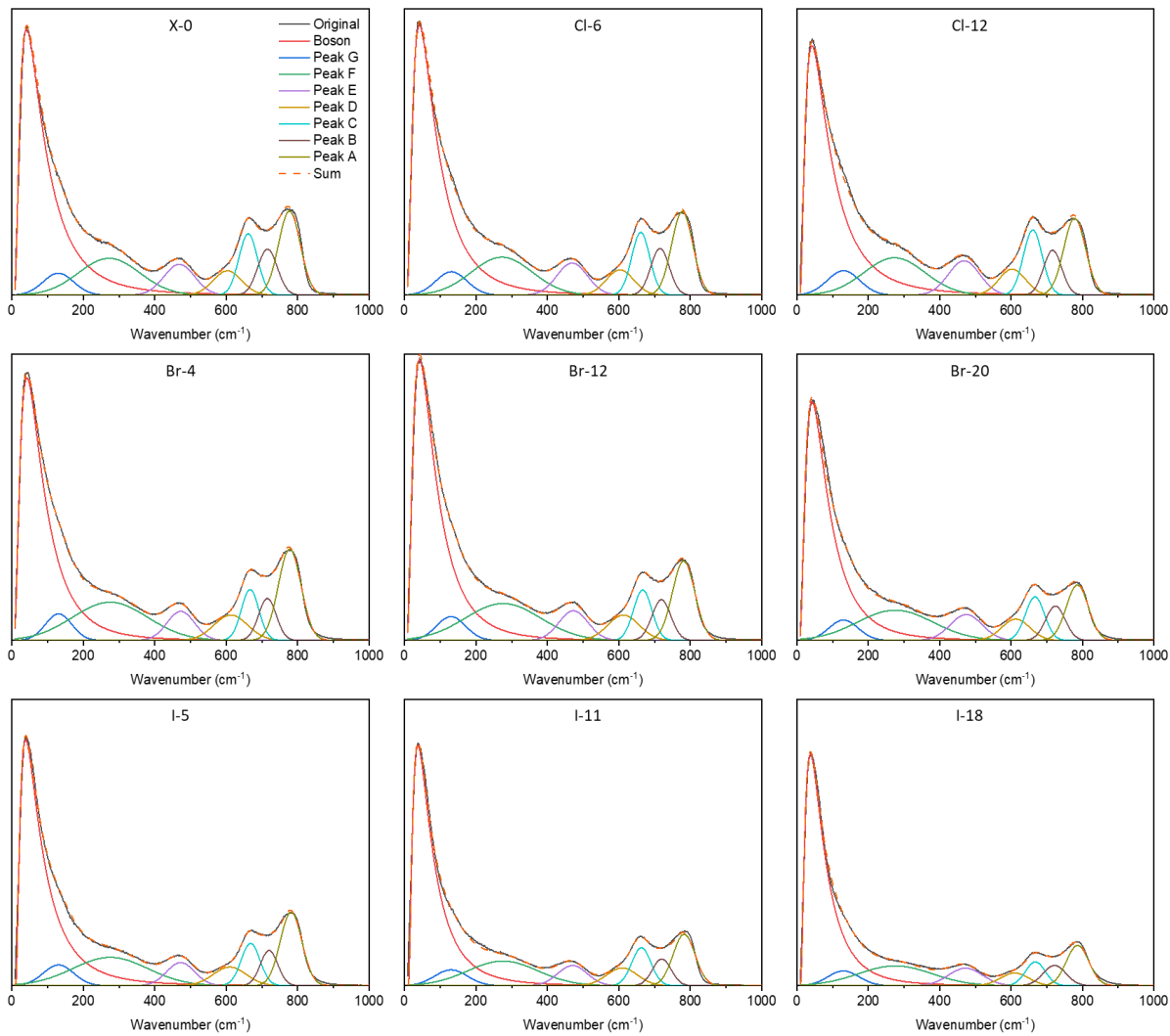
Figure S. 13 Several examples of deconvoluted Raman spectra, indicating the reliability of the deconvolution.
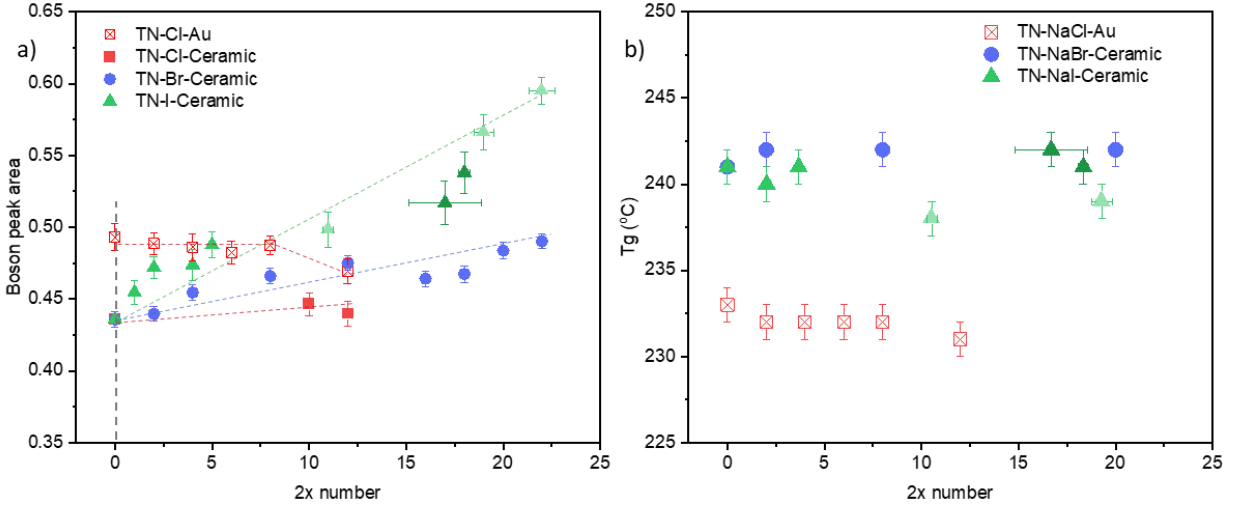
Figure S. 14 The plots of Boson peak areas of TN-NaCl, TN-NaBr and TN-NaI glass systems, with dot-lines as guides for viewing. Note: light green colour highlights the TN-NaI glasses prepared at 550 °C, the deep green colour indicates those prepared using three-step melting method.

B2.4. Impedance spectroscopy

Voltage signals with different frequencies are applied to obtain the response impedance spectrum of the sample. At each frequency, an alternating monochromatic voltage signal $v(t)=V_msin(\omega t)$ (V_m=1 V) is applied to the sample cell with one frequency ($\omega = f/2\pi$), then the response steady current $i(t)=I_msin(\omega t+\theta)$ is collected. Due to the dielectric behaviours of the specimen under the applied electric field, a phase difference will be observed between the spectra of $v(t)$ and $i(t)$, which appears as θ in the function of $i(t)$ [109, 110]. Accordingly, the value of the real (Z') and imaginary (Z'') parts of the impedance at each applied frequency can be determined by the values of V_m, I_m and θ (the mathematical details presented below). Then via varying the frequencies of applied voltage signal, a series of Z' and Z" data corresponding to each frequency can be obtained, thus a complex impedance spectrum covering the desired frequency range can be generated.
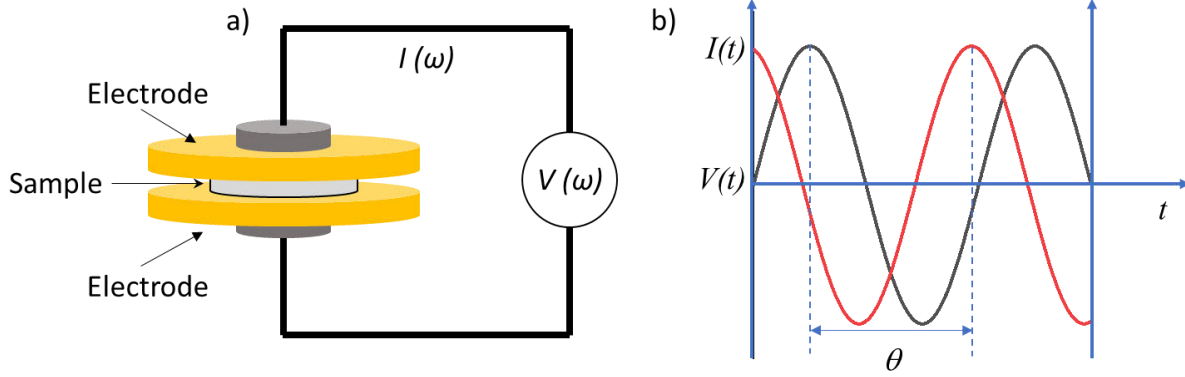
Figure S. 15 a) Schematic diagram of the parallel plate measurement method. b) example of voltage and current plotted VS time [213].

According to the Euler relation $\exp(j\theta) = \cos(\theta) + j\sin(\theta)$, the sinusoidal functions *v(t)* and *i(t)* can be expressed in time-domain representation as:

$$v(t) = V_m \sin(\omega t) = V_m e^{j\omega t}$$

$$i(t) = I_m \sin(\omega t + \theta) = I_m e^{j(\omega t + \theta)}$$

The complex impedance *Z** can be calculated according to Ohm's law [214]:

$$Z^* = \frac{v(t)}{i(t)} = \frac{V_m}{I_m} * e^{-j\theta}$$

Splitting the complex impedance *Z** to its real and imaginary parts yields:

$$Z^* = Z' + jZ''$$

Thus, accordingly, the complex-plane representation of impedance is given by:

$$|Z| = \frac{V_m}{I_m} = \sqrt{Z'^2 + Z''^2}$$

$$Z' = |Z| \cos(\theta) = \frac{V_m}{I_m} \cos(\theta)$$

$$Z' = |Z| \cos(\theta) = \frac{V_m}{I_m} \cos(\theta)$$

$$Z'' = -|Z| \sin(\theta) = -\frac{V_m}{I_m} \sin(\theta)$$

$$tan\theta = \frac{-Z''}{Z'}$$

$|Z|$ is the magnitude of impedance, and Z' and Z'' are the real and imaginary parts of impedance, respectively. At each frequency, the values of Z' and Z'' will be collected. Thus, at the whole range of applied frequency points, the complete $Z'(\omega)$ and $Z''(\omega)$ spectra can be generated. It is important to note that, Z'' is expressed differently between different communities, i.e., it is a negative quantity in physics but positive quantity in engineering.
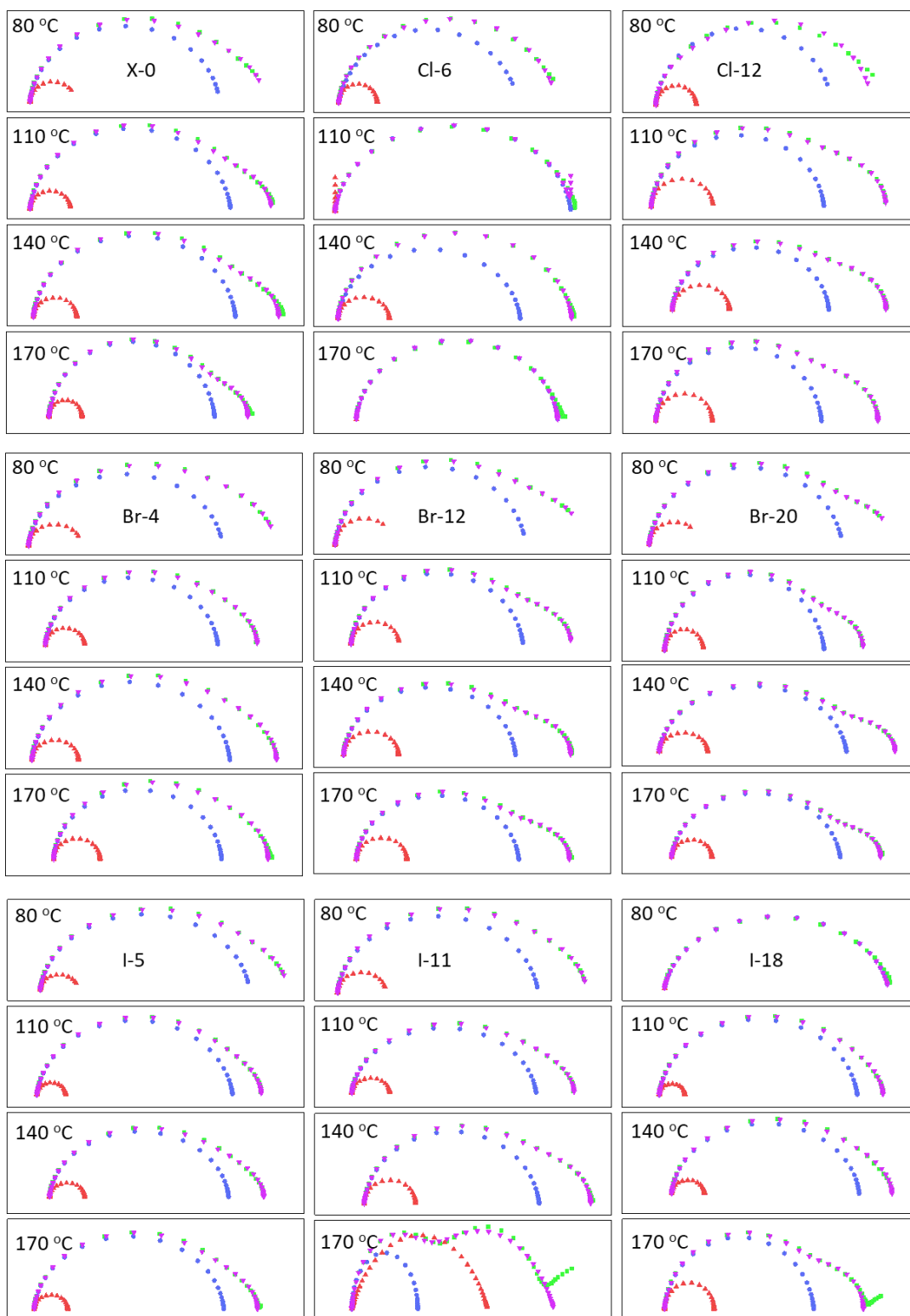
Figure S. 16 Several examples of the fitted impedance spectra at different temperatures. The high overlap of the collected spectra and the fitted results show the high reliability of the fitting.

B2.5. XRD
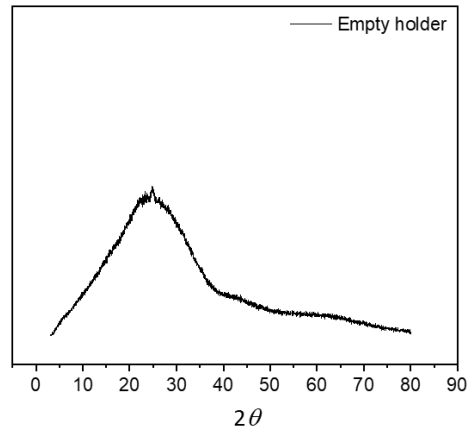
Figure S. 17 The XRD spectrum of empty glass holder. The hump at ~25° is corresponding to the amorphous XRD spectrum of the empty glass holder.

Figure S. 18 Cross-section of the I-28, showing the crystals formed on the top-fire-polished surface.

B2.6 SEM and EDX
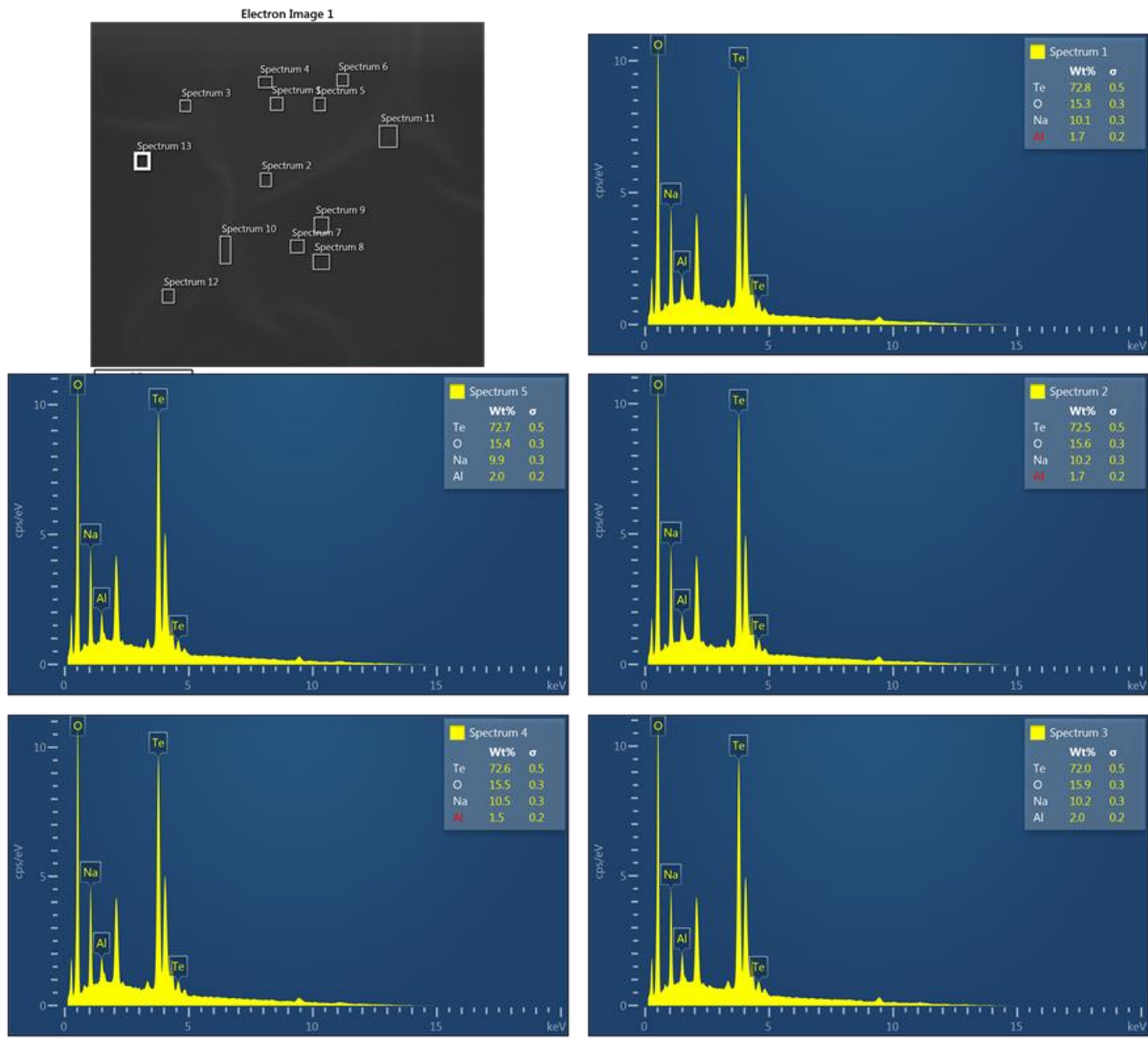
Figure S. 19 The EDX measurements of X-0-ceramic specimen, showing the concentration (wt%) of elements. Accordingly, the concentration of Al is calculated to be 4 mol%.
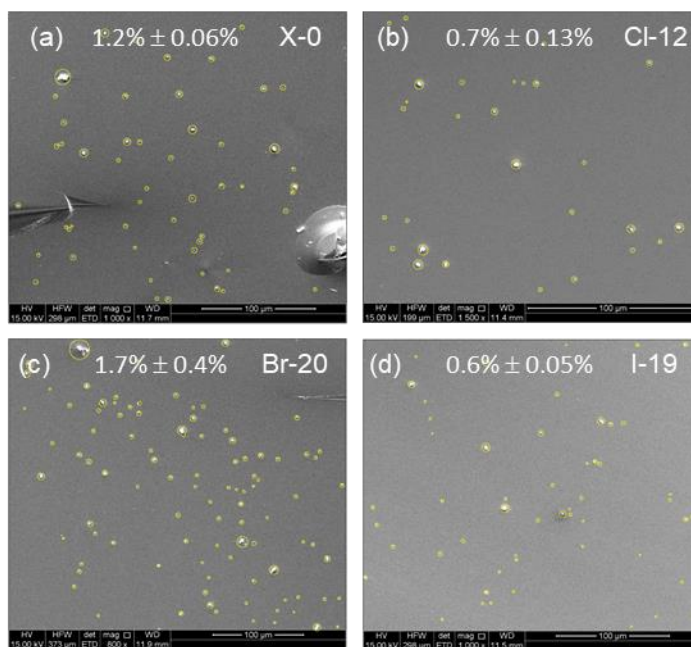
Figure S. 20 Data processing using ImageJ to measure the area density of volume crystal.
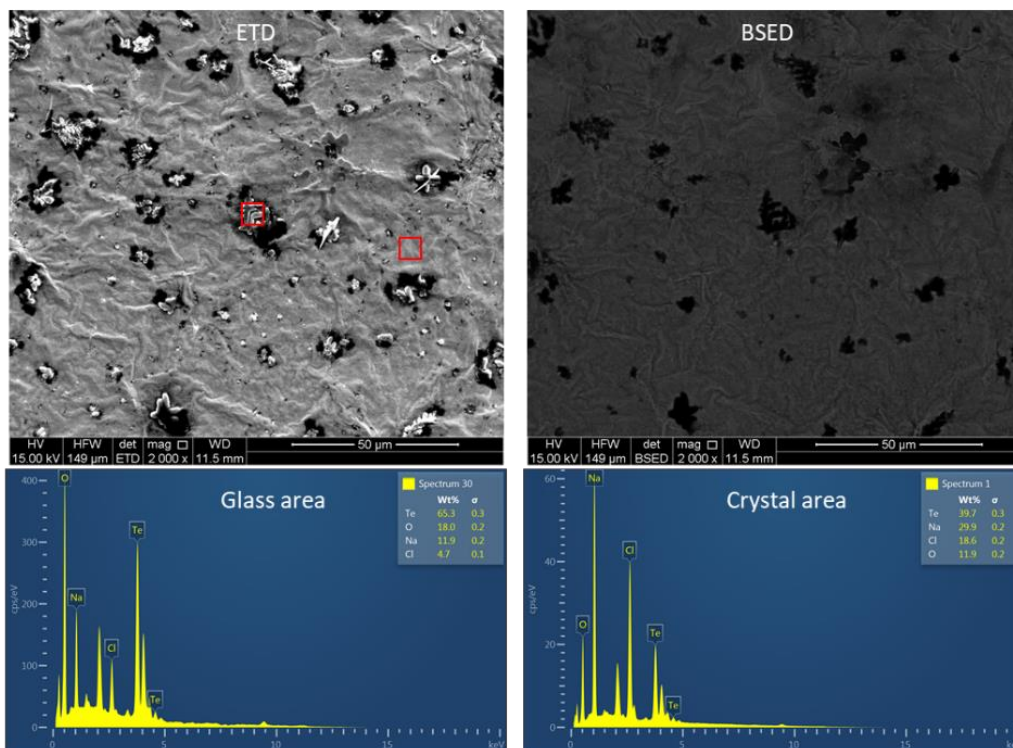
Figure S. 21 SEM images of Cl-12 glass with hydrolysed surface collected using ETD and BSED modes. The elemental concentrations (wt%) of crystal and glass regions are detected by EDX, showing the crystal has a higher concentration of Na.

Table S. 6 The $X_{surface}$ estimated from 4 samples.

	worst scenario estimated surface crystal
X-0	12.64% ± 6.04%
Cl-12	12.59% ± 5.57%
Br-22	10.93% ± 4.75%
I-19	10.76% ± 4.72%

References

1. Stanworth, J., Tellurite glasses. *Nature* **1952,** *169* (4301), 581-582.
2. El-Mallawany, R. A., *Tellurite glasses handbook: physical properties and data*. CRC press: 2014.
3. Smirnov, M.; Mirgorodsky, A.; Masson, O.; Thomas, P., Quantum mechanical study of pre-dissociation enhancement of linear and nonlinear polarizabilities of (TeO2) n oligomers as a key to understanding the remarkable dielectric properties of TeO2 glasses. *The Journal of Physical Chemistry A* **2012,** *116* (37), 9361-9369.
4. Mirgorodsky, A.; Soulis, M.; Thomas, P.; Merle-Méjean, T.; Smirnov, M., Ab initio study of the nonlinear optical susceptibility of Te O 2-based glasses. *Physical Review B* **2006,** *73* (13), 134206.
5. Condon, E. U., Physics of the glassy state. I. constitution and structure. *American Journal of Physics* **1954,** *22* (2), 43-53.
6. Zachariasen, W. H., The atomic arrangement in glass. *Journal of the American Chemical Society* **1932,** *54* (10), 3841-3851.
7. Bingham, P.; Hand, R.; Hannant, O.; Forder, S.; Kilcoyne, S. H., Effects of modifier additions on the thermal properties, chemical durability, oxidation state and structure of iron phosphate glasses. *Journal of Non-Crystalline Solids* **2009,** *355* (28-30), 1526-1538.
8. Desirena, H.; Schülzgen, A.; Sabet, S.; Ramos-Ortiz, G.; De la Rosa, E.; Peyghambarian, N., Effect of alkali metal oxides R2O (R= Li, Na, K, Rb and Cs) and network intermediate MO (M= Zn, Mg, Ba and Pb) in tellurite glasses. *Optical Materials* **2009,** *31* (6), 784-789.
9. Hodgson, S.; Weng, L., Preparation of tellurite thin films from tellurium isopropoxide precursor by sol–gel processing. *Journal of non-crystalline solids* **2000,** *276* (1-3), 195-200.
10. Pan, X.; Zhao, J.; Qian, G.; Zhang, X.; Ruan, Y.; Abell, A.; Ebendorff-Heidepriem, H., Mechanistic insight into the non-hydrolytic sol–gel process of tellurite glass films to attain a high transmission. *RSC Advances* **2020,** *10* (4), 2404-2415.
11. Wei, H.-y.; Lin, J.; Huang, W.-h.; Feng, Z.-b.; Li, D.-w., Preparation of TeO2 based thin films by nonhydrolytic sol–gel process. *Materials Science and Engineering: B* **2009,** *164* (1), 51-59.
12. Pietralunga, S. M.; Lanata, M.; Ferè, M.; Piccinin, D.; Cusmai, G.; Torregiani, M.; Martinelli, M., High-contrast waveguides in sputtered pure TeO 2 glass thin films. *Optics express* **2008,** *16* (26), 21662-21670.
13. Garaga, M. N.; Werner-Zwanziger, U.; Zwanziger, J.; DeCeanne, A.; Hauke, B.; Bozer, K.; Feller, S., Short-range structure of TeO2 glass. *The Journal of Physical Chemistry C* **2017,** *121* (50), 28117-28124.
14. Marple, M. A.; Jesuit, M.; Hung, I.; Gan, Z.; Feller, S.; Sen, S., Structure of TeO2 glass: Results from 2D 125Te NMR spectroscopy. *Journal of Non-Crystalline Solids* **2019,** *513*, 183-190.
15. Barney, E. R.; Hannon, A. C.; Holland, D.; Umesaki, N.; Tatsumisago, M.; Orman, R. G.; Feller, S., Terminal oxygens in amorphous TeO2. *The Journal of Physical Chemistry Letters* **2013,** *4* (14), 2312-2316.
16. Alderman, O.; Benmore, C. J.; Feller, S.; Kamitsos, E.; Simandiras, E.; Liakos, D. G.; Jesuit, M.; Boyd, M.; Packard, M.; Weber, R., Short-range disorder in TeO2 melt and glass. *The journal of physical chemistry letters* **2019,** *11* (2), 427-431.

17.	Basch, H.; Cohen, D.; Albeck, M., The electronic states of TeO2. *Chemical physics letters* **1988,** *144* (5-6), 450-454.

18.	Saddeek, Y.; Yahia, I.; Dobrowolski, W.; Kilanski, L.; Romcevic, N.; Arciszewska, M., Infrared, Raman spectroscopy and ac magnetic susceptibility of Gd2O3-TeO2-V2O5 glasses. *optoelectronics and advanced materials-rapid communications* **2009,** *3* (June 2009), 559-564.

19.	Wang, J.; Vogel, E.; Snitzer, E., Tellurite glass: a new candidate for fiber devices. *Optical materials* **1994,** *3* (3), 187-203.

20.	Jha, A.; Richards, B.; Jose, G.; Toney Fernandez, T.; Hill, C.; Lousteau, J.; Joshi, P., Review on structural, thermal, optical and spectroscopic properties of tellurium oxide based glasses for fibre optic and waveguide applications. *International Materials Reviews* **2012,** *57* (6), 357-382.

21.	Zhao, J.; Zheng, X.; Schartner, E. P.; Ionescu, P.; Zhang, R.; Nguyen, T. L.; Jin, D.; Ebendorff‐Heidepriem, H., Upconversion nanocrystal‐doped glass: a new paradigm for photonic materials. *Advanced Optical Materials* **2016,** *4* (10), 1507-1517.

22.	Lin, H.; Jiang, S.; Wu, J.; Song, F.; Peyghambarian, N.; Pun, E., Er3+ doped Na2O–Nb2O5–TeO2 glasses for optical waveguide laser and amplifier. *Journal of Physics D: Applied Physics* **2003,** *36* (7), 812.

23.	Li, Q.; Liu, L.; Jia, Z.; Qin, G.; Ohishi, Y.; Qin, W., Increased red frequency shift in coherent mid-infrared supercontinuum generation from tellurite microstructured fibers. *Journal of Lightwave Technology* **2017,** *35* (21), 4740-4746.

24.	Pandey, A.; Som, S.; Kumar, V.; Kumar, V.; Kumar, K.; Rai, V. K.; Swart, H., Enhanced upconversion and temperature sensing study of Er3+–Yb3+ codoped tungsten–tellurite glass. *Sensors and Actuators B: Chemical* **2014,** *202*, 1305-1312.

25.	Singh, A. K., Ho3+: TeO2 glass, a probe for temperature measurements. *Sensors and Actuators A: Physical* **2007,** *136* (1), 173-177.

26.	Yan, X.; Mont, F. W.; Poxson, D. J.; Schubert, M. F.; Kim, J. K.; Cho, J.; Schubert, E. F., Refractive-index-matched indium–tin-oxide electrodes for liquid crystal displays. *Japanese Journal of Applied Physics* **2009,** *48* (12R), 120203.

27.	Remes, Z.; Kromka, A.; Vanecek, M.; Grinevich, A.; Hartmannova, H.; Kmoch, S., The RF plasma surface chemical modification of nanodiamond films grown on glass and silicon at low temperature. *Diamond and related materials* **2007,** *16* (4-7), 671-674.

28.	Davis, B.; Keller, D., Undamped regular spiking of high energy ruby laser. *Applied Physics Letters* **1964,** *5* (4), 80-81.

29.	Hondow, N.; Brydson, R.; Wang, P.; Holton, M. D.; Brown, M. R.; Rees, P.; Summers, H. D.; Brown, A., Quantitative characterization of nanoparticle agglomeration within biological media. *Journal of Nanoparticle Research* **2012,** *14* (7), 977.

30.	Mizuno, Y.; Ikeda, M.; Yoshida, A., Application of tellurite bonding glasses to magnetic heads. *Journal of materials science letters* **1992,** *11* (24), 1653-1656.

31.	El-Mallawany, R.; Sayyed, M., Comparative shielding properties of some tellurite glasses: Part 1. *Physica B: Condensed Matter* **2018,** *539*, 133-140.

32.	Cankaya, H.; Sennaroglu, A., Bulk Nd 3+-doped tellurite glass laser at 1.37 μm. *Applied Physics B* **2010,** *99* (1), 121-125.

33.	Kityk, I. V.; AlZayed, N.; El-Naggar, A.; Reben, M.; Wasylak, J.; Lakshminarayana, G.; Reshak, A. H.; Brik, M., Er–Pr doped tellurite glass nanocomposites for white light emitting diodes. *Optics Communications* **2012,** *285* (5), 655-658.

34.   Arai, T., The study of the optical properties of conducting tin oxide films and their interpretation in terms of a tentative band scheme. *Journal of the Physical Society of Japan* **1960,** *15* (5), 916-927.

35.   Zhao, Y.; Meek, G. A.; Levine, B. G.; Lunt, R. R., Near‐infrared harvesting transparent luminescent solar concentrators. *Advanced Optical Materials* **2014,** *2* (7), 606-611.

36.   Lipomi, D. J.; Vosgueritchian, M.; Tee, B. C.; Hellstrom, S. L.; Lee, J. A.; Fox, C. H.; Bao, Z., Skin-like pressure and strain sensors based on transparent elastic films of carbon nanotubes. *Nature nanotechnology* **2011,** *6* (12), 788-792.

37.   LeChasseur, Y.; Dufour, S.; Lavertu, G.; Bories, C.; Deschênes, M.; Vallée, R.; De Koninck, Y., A microprobe for parallel optical and electrical recordings from single neurons in vivo. *Nature methods* **2011,** *8* (4), 319-325.

38.   Calahoo, C.; Wondraczek, L., Ionic glasses: Structure, properties and classification. *Journal of Non-Crystalline Solids: X* **2020**, 100054.

39.   Styskalik, A.; Skoda, D.; Barnes, C. E.; Pinkas, J., The power of non-hydrolytic sol-gel chemistry: A review. *Catalysts* **2017,** *7* (6), 168.

40.   Niederberger, M., Nonaqueous sol–gel routes to metal oxide nanoparticles. *Accounts of chemical research* **2007,** *40* (9), 793-800.

41.   Zheng, B.; Zhao, M.; Guo, Q.; Yu, Y.; Lu, S.; Jiang, X.; Zhou, S., A chip-based microcavity derived from multi-component tellurite glass. *J. Mater. Chem. C* **2015,** *3* (20), 5141-5144.

42.   Pan, X. Tellurite glass film for enhanced emission and collection efficiency of NV centre in nanodiamond. Thesis (M.Phil.)--University of Adelaide, School of Physical Sciences, 2017., 2017.

43.   Mahindaratne, M. P.; Wimalasena, K., Detailed characterization of p-toluenesulfonic acid monohydrate as a convenient, recoverable, safe, and selective catalyst for alkylation of the aromatic nucleus. *The Journal of Organic Chemistry* **1998,** *63* (9), 2858-2866.

44.   Zhang, Z.; Xie, C.; Feng, L.; Ma, C., PTSA-catalyzed one-pot synthesis of quinoxalines using DMSO as the oxidant. *Synthetic Communications* **2016,** *46* (18), 1507-1518.

45.   Girard, S. A.; Huang, H.; Zhou, F.; Deng, G.-J.; Li, C.-J., Catalytic dehydrogenative aromatization: an alternative route to functionalized arenes. *Organic Chemistry Frontiers* **2015,** *2* (3), 279-287.

46.   Ogbuu, O.; Du, Q.; Lin, H.; Li, L.; Zou, Y.; Koontz, E.; Smith, C.; Danto, S.; Richardson, K.; Hu, J.; Lucas, P., Impact of Stoichiometry on Structural and Optical Properties of Sputter Deposited Multicomponent Tellurite Glass Films. *Journal of the American Ceramic Society* **2015,** *98* (6), 1731-1738.

47.   Henderson, M.; Gibson, B.; Ebendorff‐Heidepriem, H.; Kuan, K.; Afshar V, S.; Orwa, J.; Aharonovich, I.; Tomljenovic‐Hanic, S.; Greentree, A.; Prawer, S., Diamond in tellurite glass: a new medium for quantum information. *Advanced Materials* **2011,** *23* (25), 2806-2810.

48.   Hayakawa, T.; Koyama, H.; Nogami, M.; Thomas, P., OPTICAL PROPERTIES OF TeO 2-TiO 2 THIN FILMS DOPED WITH Eu 3+ IONS FABRICATED BY SOL-GEL PROCESSING. *Journal of the University of Chemical Technology & Metallurgy* **2012,** *47* (4).

49.   Hodgson, S.; Weng, L., Sol-gel processing of tellurium oxide and suboxide thin films with potential for optical data storage application. *Journal of sol-gel science and technology* **2000,** *18* (2), 145-158.

50.   Lindqvist, O., The Crystal Structure of Tellurium (IV) Catecholate. *Acta Chemica Scandinavica* **1967,** *21* (0), 1473-1483.

51.   Cheng, Y.; Yan, N.; Han, X.; Zhang, Z.; Zhang, T.; Song, Z.; Liu, B.; Feng, S., Thermally induced phase separation of Si–Sb–Te alloy. *Journal of Non-Crystalline Solids* **2010,** *356* (18-19), 884-888.

52.   Nukui, A.; Taniguchi, T.; Miyata, M., In situ high-temperature X-ray observation of structural changes of tellurite glasses with p-block oxides; ZnO–TeO 2 glasses. *Journal of non-crystalline solids* **2001,** *293*, 255-260.

53.   Lee, D. W.; Ok, K. M., New Polymorphs of Ternary Sodium Tellurium Oxides: Hydrothermal Synthesis, Structure Determination, and Characterization of β-Na2Te4O9 and Na2Te2O6· 1.5 H2O. *Inorganic chemistry* **2014,** *53* (19), 10642-10648.

54.   Šantić, A.; Moguš-Milanković, A.; Furić, K.; Rajić-Linarić, M.; Ray, C. S.; Day, D. E., Structural properties and crystallization of sodium tellurite glasses. *Croatica Chemica Acta* **2008,** *81* (4), 559-567.

55.   Vioux, A., Nonhydrolytic sol− gel routes to oxides. *Chemistry of Materials* **1997,** *9* (11), 2292-2299.

56.   Vogel, W., *Glass chemistry*. Springer Science & Business Media: 2012.

57.   Tang, C. Y.; Kwon, Y.-N.; Leckie, J. O., Effect of membrane chemistry and coating layer on physiochemical properties of thin film composite polyamide RO and NF membranes: I. FTIR and XPS characterization of polyamide and coating layer chemistry. *Desalination* **2009,** *242* (1-3), 149-167.

58.   Yang, H.; Yan, R.; Chen, H.; Lee, D. H.; Zheng, C., Characteristics of hemicellulose, cellulose and lignin pyrolysis. *Fuel* **2007,** *86* (12), 1781-1788.

59.   Marshall, C. P.; Carter, E. A.; Leuko, S.; Javaux, E. J., Vibrational spectroscopy of extant and fossil microbes: relevance for the astrobiological exploration of Mars. *Vibrational Spectroscopy* **2006,** *41* (2), 182-189.

60.   Carrillo, F.; Colom, X.; Sunol, J.; Saurina, J., Structural FTIR analysis and thermal characterisation of lyocell and viscose-type fibres. *European Polymer Journal* **2004,** *40* (9), 2229-2234.

61.   Liu, B. H.; Dou, L. T.; He, F.; Yang, J.; Li, Z. P., A cobalt coordination compound with indole acetic acid for fabrication of a high performance cathode catalyst in fuel cells. *RSC Advances* **2016,** *6* (23), 19025-19033.

62.   Çelikbilek, M.; Erçin Ersundu, A.; Aydin, S., Glass Formation and Characterization Studies in the TeO2–WO3–Na2O System. *Journal of the American Ceramic Society* **2013,** *96* (5), 1470-1476.

63.   Marple, M. A.; Aitken, B. G.; Kim, S.; Sen, S., Fast Li-Ion Dynamics in Stoichiometric Li2S–Ga2Se3–GeSe2 Glasses. *Chemistry of Materials* **2017,** *29* (20), 8704-8710.

64.   Kumar, P. P.; Yashonath, S., Ionic conduction in the solid state. *Journal of Chemical Sciences* **2006,** *118* (1), 135-154.

65.   Hooton, I. E.; Jacobs, P., Ionic conductivity of pure and doped sodium chloride crystals. *Canadian journal of chemistry* **1988,** *66* (4), 830-835.

66.   Murch, G., The Nernst-Einstein equation in high-defect-content solids. *Philosophical Magazine A* **1982,** *45* (4), 685-692.

67.   Abe, Y.; Hosono, H.; Lee, W.-H.; Kasuga, T., Electrical conduction due to protons and alkali-metal ions in oxide glasses. *Physical Review B* **1993,** *48* (21), 15621.

68.	SCHULTZ, P. C.; MIZZONI, M. S., Anionic Conductivity in Halogen‑Containing Lead Silicate Glasses. *Journal of the American Ceramic Society* **1973,** *56* (2), 65-68.

69.	Abd El‑Mongy, A., Effect of halogen on the structure and ionic conductivity of silicate glasses. *physica status solidi (a)* **1994,** *144* (1), 17-22.

70.	Levasseur, A.; Brethous, J.-C.; Réau, J.-M.; Hagenmuller, P., Etude comparee de la conductivite ionique du lithium dans les halogenoborates vitreux. *Materials Research Bulletin* **1979,** *14* (7), 921-927.

71.	Jain, H.; Downing, H.; Peterson, N., The mixed alkali effect in lithium-sodium borate glasses. *Journal of non-crystalline solids* **1984,** *64* (3), 335-349.

72.	Martin, S. W., Ionic conduction in phosphate glasses. *Journal of the American Ceramic Society* **1991,** *74* (8), 1767-1784.

73.	Martin, S. W.; Angell, C., Dc and ac conductivity in wide composition range Li2O P2O5 glasses. *Journal of Non‑Crystalline Solids* **1986,** *83* (1-2), 185-207.

74.	Tanaka, K.; Yoko, T.; Kamiya, K.; Yamada, H.; Sakka, S., Properties of oxybromide tellurite glasses in the system LiBr	Li2O	TeO2. *Journal of non-crystalline solids* **1991,** *135* (2-3), 211-218.

75.	Poletto Rodrigues, B.; Limbach, R.; Buzatto de Souza, G.; Ebendorff-Heidepriem, H.; Wondraczek, L., Correlation between ionic mobility and plastic flow events in NaPO3-NaCl-Na2SO4 glasses. *Frontiers in Materials* **2019,** *6*, 128.

76.	Yoko, T.; Kamiya, K.; Yamada, H.; Tanaka, K., Glass‑Forming Region and Structure of Oxyhalide Glasses in the System LiCl‑Li2O‑TeO2. *Journal of the American Ceramic Society* **1988,** *71* (2), C‑70-C‑71.

77.	Yoko, T.; Kamiya, K.; Tanaka, K.; Yamada, H.; Sakka, S., Glass-forming region and structure of oxyhalide tellurite glasses containing LiX (X= F and Br) and Li2O. *Journal of the Ceramic Society of Japan* **1989,** *97* (1123), 289-294.

78.	Huheey, J. E., Bent's rule: energetics, electronegativity, and the structures of nonmetal fluorides. *Inorganic Chemistry* **1981,** *20* (11), 4033-4035.

79.	Wang, Y.; Osaka, A.; Miura, Y.; Takahashi, K., Effect of halide ions on Li+ ionic conductivity in oxyhalo-borate glasses. *Journal of Materials Research* **1987,** *2* (5), 606-609.

80.	Wang, Y.; Osaka, A.; Miura, Y.; Takahashi, K., Behavior of halide ions in borate glass. *Journal of Non-Crystalline Solids* **1987,** *95*, 571-576.

81.	Le, Q. H.; Palenta, T.; Benzine, O.; Griebenow, K.; Limbach, R.; Kamitsos, E. I.; Wondraczek, L., Formation, structure and properties of fluoro-sulfo-phosphate poly-anionic glasses. *Journal of Non-Crystalline Solids* **2017,** *477*, 58-72.

82.	Tanaka, K.; Yoko, T.; Yamada, H.; Kamiya, K., Structure and ionic conductivity of LiCl	Li2O	TeO2 glasses. *Journal of non-crystalline solids* **1988,** *103* (2-3), 250-256.

83.	Luo, Y.-R., *Comprehensive handbook of chemical bond energies*. CRC press: 2007.

84.	Shannon, R. T.; Prewitt, C. T., Effective ionic radii in oxides and fluorides. *Acta Crystallographica Section B: Structural Crystallography and Crystal Chemistry* **1969,** *25* (5), 925-946.

85.	Sidkey, M.; Gaafar, M., Ultrasonic studies on network structure of ternary TeO2–WO3–K2O glass system. *Physica B: Condensed Matter* **2004,** *348* (1-4), 46-55.

86.	Sekiya, T.; Mochida, N.; Ohtsuka, A.; Tonokawa, M., Raman spectra of MO1/2TeO2 (M= Li, Na, K, Rb, Cs and Tl) glasses. *Journal of non-crystalline solids* **1992,** *144*, 128-144.

87.   Murugavel, S.; Roling, B., AC conductivity spectra of alkali tellurite glasses: composition-dependent deviations from the Summerfield scaling. *Physical review letters* **2002,** *89* (19), 195902.

88.   Pan, A.; Ghosh, A., Activation energy and conductivity relaxation of sodium tellurite glasses. *Physical Review B* **1999,** *59* (2), 899.

89.   Kavaklıoğlu, K. B.; Aydin, S.; Çelikbilek, M.; Ersundu, A. E., The TeO2‑Na2O System: Thermal Behavior, Structural Properties, and Phase Equilibria. *International Journal of Applied Glass Science* **2015,** *6* (4), 406-418.

90.   Armstrong, J., Quantitative analysis of silicate and oxide materials: comparison of Monte Carlo, ZAF, and ψ (ρz) procedures. *Microbeam analysis* **1988**, 239-246.

91.   Donovan, J. J.; Tingle, T. N., An improved mean atomic number background correction for quantitative microanalysis. *Microscopy and Microanalysis* **1996,** *2* (1), 1-7.

92.   Donovan, J. J.; Singer, J. W.; Armstrong, J. T., A new EPMA method for fast trace element analysis in simple matrices. *American Mineralogist* **2016,** *101* (8), 1839-1853.

93.   Donovan, J. J.; Rowe, M., Techniques for improving quantitative analysis of mineral glasses. *Geochimica et Cosmochimica Acta Supplement* **2005,** *69* (10), A589.

94.   de Clermont-Gallerande, J.; Saito, S.; Colas, M.; Thomas, P.; Hayakawa, T., New understanding of TeO2–ZnO–Na2O ternary glass system. *Journal of Alloys and Compounds* **2021,** *854*, 157072.

95.   Reule, A., Errors in spectrophotometry and calibration procedures to avoid them. *Journal of research of the National Bureau of Standards. Section A, Physics and chemistry* **1976,** *80* (4), 609.

96.   Tagiara, N.; Palles, D.; Simandiras, E.; Psycharis, V.; Kyritsis, A.; Kamitsos, E. J. J. o. N.-C. S., Synthesis, thermal and structural properties of pure TeO2 glass and zinc-tellurite glasses. **2017,** *457*, 116-125.

97.   Shuker, R.; Gammon, R. W., Raman-scattering selection-rule breaking and the density of states in amorphous materials. *Physical Review Letters* **1970,** *25* (4), 222.

98.   Galeener, F.; Sen, P., Theory for the first-order vibrational spectra of disordered solids. *Physical Review B* **1978,** *17* (4), 1928.

99.   Kalampounias, A.; Yannopoulos, S.; Papatheodorou, G., Vibrational modes of sodium–tellurite glasses: Local structure and Boson peak changes. *Journal of Physics and Chemistry of Solids* **2007,** *68* (5-6), 1035-1039.

100.   Ando, M. F.; Benzine, O.; Pan, Z.; Garden, J.-L.; Wondraczek, K.; Grimm, S.; Schuster, K.; Wondraczek, L., Boson peak, heterogeneity and intermediate-range order in binary SiO 2-Al 2 O 3 glasses. *Scientific reports* **2018,** *8* (1), 1-14.

101.   Ferraro, J. R., *Introductory raman spectroscopy*. Elsevier: 2003.

102.   Sarkar, S.; Maity, I.; Pradeepa, H.; Nayak, G.; Marty, L.; Renard, J.; Coraux, J.; Bendiab, N.; Bouchiat, V.; Das, S., Anharmonicity in Raman-active phonon modes in atomically thin MoS 2. *Physical Review B* **2020,** *101* (20), 205302.

103.   Mills, I., *Quantities, units and symbols in physical chemistry/prepared for publication by Ian Mills...[et al.]*. Oxford; Boston: Blackwell Science; Boca Raton, Fla.: CRC Press [distributor]: 1993.

104.   White, R. P.; Lipson, J. E., Polymer free volume and its connection to the glass transition. *Macromolecules* **2016,** *49* (11), 3987-4007.

105.   Rouaud, M., Probability, statistics and estimation. *Propagation of uncertainties* **2013**, 191.

106.   Wolter, K., *Introduction to variance estimation*. Springer Science & Business Media: 2007.

107.   Nahir, T. M., Impedance Spectroscopy: Theory, Experiment, and Applications, Edited by Evgenij Barsoukov (Texas Instruments Inc.) and J. Ross Macdonald (University of North Carolina, Chapel Hill). John Wiley & Sons, Inc.: Hoboken, NJ. 2005. xvii+ 596 pp. $125.00. ISBN 0471-64749-7. ACS Publications: 2005.

108.   Khan, M. T.; Ali, S. M., A brief review of measuring techniques for characterization of dielectric materials. *International Journal of Information Technology and Electrical Engineering* **2012,** *1* (1).

109.   Macdonald, J. R., Impedance spectroscopy. *Annals of biomedical engineering* **1992,** *20* (3), 289-305.

110.   Von Hauff, E., Impedance spectroscopy for emerging photovoltaics. *The Journal of Physical Chemistry C* **2019,** *123* (18), 11329-11346.

111.   Medina, F. A., Impedance Spectroscopy Studies of Silica-Titania Glasses and Glass-Ceramics. **2009**.

112.   Chassagne, C.; Dubois, E.; Jiménez, M. L.; Van der Ploeg, J.; Van Turnhout, J., Compensating for electrode polarization in dielectric spectroscopy studies of colloidal suspensions: theoretical assessment of existing methods. *Frontiers in chemistry* **2016,** *4*, 30.

113.   Singh, M. B.; Kant, R., Theory of Electric Double Layer Dynamics at Blocking Electrode. *arXiv preprint arXiv:1103.0681* **2011**.

114.   technologies, n., High Performance Dielectric, Conductivity and Electrochemical Impedance Analyzers. 2013.

115.   Jayasinghe, G.; Coppo, D.; Bandaranayake, P.; Souquet, J., Electrical properties of TeO2 glasses with Na2O as network modifier. *Solid State Ionics* **1995,** *76* (3-4), 297-300.

116.   Ngai, K.; Wang, Y.; Moynihan, C., The mixed alkali effect revisited: the importance of ion–ion interactions. *Journal of non-crystalline solids* **2002,** *307*, 999-1011.

117.   Chen, Q.; Chen, Q.; Ferraris, M., Effect of Ceramic Crucibles on Magneto-Optical PbO-Bi2O3-B2O3Glasses Properties. *New Journal of Glass and Ceramics* **2012,** *2* (01), 41.

118.   Topping, J.; Cameron, N.; Murthy, M., Properties and Structure of Glasses in the System Bi2O3‐SiO2‐GeO2. *Journal of the American Ceramic Society* **1974,** *57* (12), 519-521.

119.   Weber, M. J.; Myers, J. D.; Blackburn, D. H., Optical properties of Nd3+ in tellurite and phosphotellurite glasses. *Journal of Applied Physics* **1981,** *52* (4), 2944-2949.

120.   Lezal, D.; Pedlikova, J.; Kostka, P.; Bludska, J.; Poulain, M.; Zavadil, J., Heavy metal oxide glasses: preparation and physical properties. *Journal of Non-Crystalline Solids* **2001,** *284* (1-3), 288-295.

121.   Kubliha, M.; Trnovcová, V.; Furár, I.; Kadlečíková, M.; Pedlíková, J.; Greguš, J., Structural peculiarities, and electrical and optical properties of 70TeO2· 30PbCl2 glasses doped with Pr3+, prepared in Pt or Au crucibles. *Journal of Non-Crystalline Solids* **2009,** *355* (37-42), 2035-2039.

122.   Sanz, O.; Haro-Poniatowski, E.; Gonzalo, J.; Navarro, J. F., Influence of the melting conditions of heavy metal oxide glasses containing bismuth oxide on their optical absorption. *Journal of non-crystalline solids* **2006,** *352* (8), 761-768.

123.   Blanchandin, S.; Marchet, P.; Thomas, P.; Champarnaud-Mesjard, J.; Frit, B.; Chagraoui, A., New investigations within the TeO2-WO3 system: phase equilibrium diagram and glass crystallization. *Journal of materials science* **1999,** *34* (17), 4285-4292.

124. Ebendorff-Heidepriem, H.; Kuan, K.; Oermann, M. R.; Knight, K.; Monro, T. M., Extruded tellurite glass and fibers with low OH content for mid-infrared applications. *Optical Materials Express* **2012,** *2* (4), 432-442.

125. Ebendorff-Heidepriem, H.; Ruan, Y.; Ji, H.; Greentree, A. D.; Gibson, B. C.; Monro, T. M., Nanodiamond in tellurite glass Part I: origin of loss in nanodiamond-doped glass. *Optical Materials Express* **2014,** *4* (12), 2608-2620.

126. Kabalci, I.; Zheng, J.; Wang, L.; Tan, L.; Xue, Y.; Zhang, Z.; Peng, M., Novel compositions of Bi2O3-ZnO-TeO2 glasses: Structure and hardness analysis. *Journal of Non-Crystalline Solids* **2017,** *464*, 23-29.

127. Clark, J. Halide Ions as Reducing Agents. https://chem.libretexts.org/@go/page/3700.

128. Vyverberg, K. L.; Jaeger, J. M.; Dutton, A., Quantifying detection limits and uncertainty in X-Ray diffraction mineralogical assessments of biogenic carbonates. *Journal of Sedimentary Research* **2018,** *88* (11), 1261-1275.

129. Tagiara, N.; Palles, D.; Simandiras, E.; Psycharis, V.; Kyritsis, A.; Kamitsos, E., Synthesis, thermal and structural properties of pure TeO2 glass and zinc-tellurite glasses. *Journal of Non-Crystalline Solids* **2017,** *457*, 116-125.

130. Awang, A.; Ghoshal, S. K.; Sahar, M.; Dousti, M. R.; Nawaz, F. In *Growth of Au nanoparticles stimulate spectroscopic properties of Er3+ doped TeO2-ZnO-Na2O glasses*, Advanced Materials Research, Trans Tech Publ: 2014; pp 254-259.

131. Budiaman, E.; Fennema, O., Linear rate of water crystallization as influenced by viscosity of hydrocolloid suspensions. *Journal of Dairy Science* **1987,** *70* (3), 547-554.

132. Jiusti, J.; Zanotto, E. D.; Feller, S. A.; Austin, H. J.; Detar, H. M.; Bishop, I.; Manzani, D.; Nakatsuka, Y.; Watanabe, Y.; Inoue, H., Effect of network formers and modifiers on the crystallization resistance of oxide glasses. *Journal of Non-Crystalline Solids* **2020,** *550*, 120359.

133. Spence, W., The UV absorption edge of tin oxide thin films. *Journal of Applied Physics* **1967,** *38* (9), 3767-3770.

134. Bürger, H.; Kneipp, K.; Hobert, H.; Vogel, W.; Kozhukharov, V.; Neov, S., Glass formation, properties and structure of glasses in the TeO2   ZnO system. *Journal of non-crystalline solids* **1992,** *151* (1-2), 134-142.

135. Gagné, O. C.; Hawthorne, F. C., Bond-length distributions for ions bonded to oxygen: alkali and alkaline-earth metals. *Acta Crystallographica Section B: Structural Science, Crystal Engineering and Materials* **2016,** *72* (4), 602-625.

136. Moon, J.; Kim, J., Spin–Orbit Effect on the Molecular Properties of TeX n (X= F, Cl, Br, and I; n= 1, 2, and 4): A Density Functional Theory and Ab Initio Study. *The Journal of Physical Chemistry A* **2016,** *120* (38), 7496-7502.

137. Pietrucci, F.; Caravati, S.; Bernasconi, M., TeO 2 glass properties from first principles. *Physical Review B* **2008,** *78* (6), 064203.

138. El-Mallawany, R. A., *Tellurite glasses handbook: physical properties and data*. CRC press: 2011.

139. Sakida, S.; Hayakawa, S.; Yoko, T., Part 2.125 Te NMR study of M2O–TeO2 (M= Li, Na, K, Rb and Cs) glasses. *Journal of non-crystalline solids* **1999,** *243* (1), 13-25.

140. Tagiara, N.; Moayedi, E.; Kyritsis, A.; Wondraczek, L.; Kamitsos, E., Short-range structure, thermal and elastic properties of binary and ternary tellurite glasses. *The Journal of Physical Chemistry B* **2019,** *123* (37), 7905-7918.

141.	SEKIYA, T.; MOCHIDA, N.; OHTSUKA, A.; TONOKAWA, M., Normal vibrations of two polymorphic forms of TeO2 crystals and assignments of Raman peaks of pure TeO2 glass. *Journal of the Ceramic Society of Japan* **1989,** *97* (1132), 1435-1440.

142.	Manning, S.; Ebendorff-Heidepriem, H.; Monro, T. M., Ternary tellurite glasses for the fabrication of nonlinear optical fibres. *Optical Materials Express* **2012,** *2* (2), 140-152.

143.	Jesuit, M.; Packard, M.; Boyd, M.; Tagiara, N. S.; Kamitsos, E. I.; Alderman, O.; Benmore, C.; Hannon, A.; Appler, M.; Feller, S., Analysis of Physical and Structural Properties of Alkali Oxide–Modified Tellurite Glasses. *Journal of Undergraduate Reports in Physics* **2020,** *30* (1), 100003.

144.	Wójcik, N. A.; Ali, S.; Möncke, D.; Tagiara, N.; Kamitsos, E.; Segawa, H.; Eriksson, M.; Jonson, B., The influence of Be addition on the structure and thermal properties of alkali-silicate glasses. *Journal of Non-Crystalline Solids* **2019,** *521*, 119532.

145.	Shishkin, O. V.; Pelmenschikov, A.; Hovorun, D. M.; Leszczynski, J., Theoretical analysis of low-lying vibrational modes of free canonical 2-deoxyribonucleosides. *Chemical Physics* **2000,** *260* (3), 317-325.

146.	Kalampounias, A. G., Low-frequency Raman scattering in alkali tellurite glasses. *Bulletin of Materials Science* **2008,** *31* (5), 781-785.

147.	Baggioli, M.; Zaccone, A., Universal origin of boson peak vibrational anomalies in ordered crystals and in amorphous materials. *Physical review letters* **2019,** *122* (14), 145501.

148.	Malinovsky, V. K.; Sokolov, A. P., The nature of boson peak in Raman scattering in glasses. *Solid state communications* **1986,** *57* (9), 757-761.

149.	Shintani, H.; Tanaka, H., Universal link between the boson peak and transverse phonons in glass. *Nature materials* **2008,** *7* (11), 870-877.

150.	Fan, J.; Zhang, Y.; Li, G.; Yue, Y., Tellurium nanoparticles enhanced electrochemical performances of TeO2-V2O5-Al2O3 glass anode for Lithium-ion batteries. *Journal of Non-Crystalline Solids* **2019,** *521*, 119491.

151.	Alıa, J.; Edwards, H.; García-Navarro, F., FT-Raman spectra of cis-bis (thiourea) tellurium (II) halides (Cl−, Br−, I−) and thiocyanate. *Journal of molecular structure* **1999,** *508* (1-3), 51-58.

152.	Zhu, D.; Ray, C. S.; Zhou, W.; Day, D. E., Glass transition and fragility of Na2O–TeO2 glasses. *Journal of non-crystalline solids* **2003,** *319* (3), 247-256.

153.	Rasband, W. S., ImageJ. Bethesda, MD: 1997.

154.	Macdonald, J. R.; Barsoukov, E., Impedance spectroscopy: theory, experiment, and applications. *History* **2005,** *1* (8), 1-13.

155.	Raju, G. G., *Dielectrics in electric fields*. CRC press: 2016.

156.	Morgan, V., Effects of frequency, temperature, compression, and air pressure on the dielectric properties of a multilayer stack of dry kraft paper. *IEEE transactions on dielectrics and electrical insulation* **1998,** *5* (1), 125-131.

157.	Wiener, O., Die Theorie des Mischkorpers fur das Feld der stationaren Stromung. *Abhandlungen der Sachsischen Gesellschaft der Akademischen Wissenschaften in Mathematik und Physik* **1912,** *32*, 507-604.

158.	Martin, S. W., Conductivity Activation Energy Relations in High‐Sodium‐Content Borate and Aluminoborate Glasses. *Journal of the American Ceramic Society* **1988,** *71* (6), 438-445.

159.   Jilani, A.; Abdel-Wahab, M. S.; Hammad, A. H., Advance deposition techniques for thin film and coating. *Modern Technologies for Creating the Thin-film Systems and Coatings* **2017,** *2*, 137-149.

160.   Shi, C.; Shi, G.; Chen, Z.; Yang, P.; Yao, M., Deposition of Cu2ZnSnS4 thin films by vacuum thermal evaporation from single quaternary compound source. *Materials Letters* **2012,** *73*, 89-91.

161.   Tanuševski, A.; Poelman, D., Optical and photoconductive properties of SnS thin films prepared by electron beam evaporation. *Solar energy materials and solar cells* **2003,** *80* (3), 297-303.

162.   Jeyachandran, Y.; Narayandass, S. K.; Mangalaraj, D.; Areva, S.; Mielczarski, J., Properties of titanium nitride films prepared by direct current magnetron sputtering. *Materials Science and Engineering: A* **2007,** *445*, 223-236.

163.   Lim, J. H.; Kang, C. K.; Kim, K. K.; Park, I. K.; Hwang, D. K.; Park, S. J., UV electroluminescence emission from ZnO light‐emitting diodes grown by high‐temperature radiofrequency sputtering. *Advanced Materials* **2006,** *18* (20), 2720-2724.

164.   Kern, W.; Ban, V. S., *Chemical vapor deposition of inorganic thin films*. Academic Press, New York: 1978; Vol. 257.

165.   Sanders, S.; Stümmler, D.; Pfeiffer, P.; Ackermann, N.; Simkus, G.; Heuken, M.; Baumann, P.; Vescan, A.; Kalisch, H., Chemical vapor deposition of organic-inorganic bismuth-based perovskite films for solar cell application. *Scientific reports* **2019,** *9* (1), 1-8.

166.   Nair, P.; Nair, M.; Garcıa, V.; Arenas, O.; Pena, Y.; Castillo, A.; Ayala, I.; Gomezdaza, O.; Sanchez, A.; Campos, J., Semiconductor thin films by chemical bath deposition for solar energy related applications. *Solar Energy Materials and Solar Cells* **1998,** *52* (3-4), 313-344.

167.   O'regan, B.; Grätzel, M., A low-cost, high-efficiency solar cell based on dye-sensitized colloidal TiO2 films. *nature* **1991,** *353* (6346), 737.

168.   Selvan, S. T.; Bullen, C.; Ashokkumar, M.; Mulvaney, P., Synthesis of Tunable, Highly Luminescent QD‐Glasses Through Sol‐Gel Processing. *Advanced Materials* **2001,** *13* (12‐13), 985-988.

169.   Korala, L.; Wang, Z.; Liu, Y.; Maldonado, S.; Brock, S. L., Uniform thin films of CdSe and CdSe (ZnS) core (shell) quantum dots by sol–gel assembly: enabling photoelectrochemical characterization and electronic applications. *Acs Nano* **2013,** *7* (2), 1215-1223.

170.   Jiang, R.; Kunz, H. R.; Fenton, J. M., Composite silica/Nafion® membranes prepared by tetraethylorthosilicate sol–gel reaction and solution casting for direct methanol fuel cells. *Journal of Membrane Science* **2006,** *272* (1-2), 116-124.

171.   Brinker, C. J.; Scherer, G. W., *Sol-gel science: the physics and chemistry of sol-gel processing*. Academic press: 2013.

172.   SCHOTT optical glass data sheets. https://refractiveindex.info/download/data/2017/schott_2017-01-20.pdf.

173.   Lin, J.-J.; Li, Z.-Q., Electronic conduction properties of indium tin oxide: single-particle and many-body transport. *Journal of Physics: Condensed Matter* **2014,** *26* (34), 343201.

174.   Pradel, A.; Ribes, M., Lithium chalcogenide conductive glasses. *Materials chemistry and physics* **1989,** *23* (1-2), 121-142.

175.   Swenson, J.; McGreevy, R.; Börjesson, L.; Wicks, J., Relations between structure and conductivity in fast ion conducting glasses. *Solid State Ionics* **1998,** *105* (1-4), 55-65.

176.   Zhang, L.; Zhou, Y.; Guo, L.; Zhao, W.; Barnes, A.; Zhang, H.-T.; Eaton, C.; Zheng, Y.; Brahlek, M.; Haneef, H. F., Correlated metals as transparent conductors. *Nature materials* **2016,** *15* (2), 204.

177.   Zhou, J., Indium tin oxide (ITO) deposition, patterning and Schottky contact fabrication. **2006**.

178.   Medvedeva, J. E.; Hettiarachchi, C. L., Tuning the properties of complex transparent conducting oxides: Role of crystal symmetry, chemical composition, and carrier generation. *Physical Review B* **2010,** *81* (12), 125116.

179.   Zhang, M.; Fang, S.; Zakhidov, A. A.; Lee, S. B.; Aliev, A. E.; Williams, C. D.; Atkinson, K. R.; Baughman, R. H., Strong, transparent, multifunctional, carbon nanotube sheets. *Science* **2005,** *309* (5738), 1215-1219.

180.   Warren, S. C.; Perkins, M. R.; Adams, A. M.; Kamperman, M.; Burns, A. A.; Arora, H.; Herz, E.; Suteewong, T.; Sai, H.; Li, Z., A silica sol–gel design strategy for nanostructured metallic materials. *Nature Materials* **2012,** *11* (5), 460-467.

181.   Langley, D.; Giusti, G.; Mayousse, C.; Celle, C.; Bellet, D.; Simonato, J.-P., Flexible transparent conductive materials based on silver nanowire networks: a review. *Nanotechnology* **2013,** *24* (45), 452001.

182.   Zeng, X. Y.; Zhang, Q. K.; Yu, R. M.; Lu, C. Z., A new transparent conductor: silver nanowire film buried at the surface of a transparent polymer. *Advanced materials* **2010,** *22* (40), 4484-4488.

183.   Wang, C.; Schindler, J. L.; Kannewurf, C. R.; Kanatzidis, M. G., Poly (3, 4-ethylenedithiathiophene). A new soluble conductive polythiophene derivative. *Chemistry of materials* **1995,** *7* (1), 58-68.

184.   Groenendaal, L.; Jonas, F.; Freitag, D.; Pielartzik, H.; Reynolds, J. R., Poly (3, 4‐ethylenedioxythiophene) and its derivatives: past, present, and future. *Advanced materials* **2000,** *12* (7), 481-494.

185.   Fujita, S.; Suzuki, A., *Electrical conduction in graphene and nanotubes*. John Wiley & Sons: 2013.

186.   Tilley, R. J., Electronic Conductivity in Solids. *Understanding Solids: The Science of Materials* **2004**, 391-429.

187.   Tsuda, N.; Nasu, K.; Fujimori, A.; Siratori, K., *Electronic conduction in oxides*. Springer Science & Business Media: 2013; Vol. 94.

188.   Suresh, B. V., *Solid State Devices and Technology*. Pearson Education India: 2010.

189.   McNaught, A. D.; Wilkinson, A., Compendium of chemical terminology. IUPAC recommendations. **1997**.

190.   Hu, C.; Muller-Karger, F. E.; Zepp, R. G., Absorbance, absorption coefficient, and apparent quantum yield: A comment on common ambiguity in the use of these optical concepts. *Limnology and Oceanography* **2002,** *47* (4), 1261-1267.

191.   Koirtyohann, S. R.; Pickett, E., Light Scattering by Particles in Atomic Absorption Spectrometry. *Analytical Chemistry* **1966,** *38* (8), 1087-1088.

192.   Gerfin, T.; Grätzel, M., Optical properties of tin‐doped indium oxide determined by spectroscopic ellipsometry. *Journal of applied physics* **1996,** *79* (3), 1722-1729.

193.   Wooten, F., *Optical properties of solids*. Academic press: 2013.

194.   E.Y.Tsymbal. Optical properties of solids 2018.

195.   Kuzmany, H., The Dielectric Function. In *Solid-State Spectroscopy: An Introduction*, Springer Berlin Heidelberg: Berlin, Heidelberg, 1998; pp 101-120.

196.   Rousselot, C.; Malugani, J.; Mercier, R.; Tachez, M.; Chieux, P.; Pappin, A.; Ingram, M., The origins of neutron-scattering prepeaks and conductivity enhancement in AgI-containing glasses. *Solid State Ionics* **1995,** *78* (3-4), 211-221.

197.   Malugani, J.; Tachez, M.; Mercier, R.; Dianoux, A.; Chieux, P., Small angle, quasielastic and inelastic neutron scattering from 0.85 AgPO3− 0.15 PbI2 glass. *Solid State Ionics* **1987,** *23* (3), 189-196.

198.   Minami, T., Fast ion conducting glasses. *Journal of Non-Crystalline Solids* **1985,** *73* (1-3), 273-284.

199.   Ravaine, D., Ionic transport properties in glasses. *Journal of Non-Crystalline Solids* **1985,** *73* (1-3), 287-303.

200.   Glass, A.; Nassau, K., Lithium ion conduction in rapidly quenched Li2O‐Al2O3, Li2O‐Ga2O3, and Li2O‐Bi2O3 glasses. *Journal of Applied Physics* **1980,** *51* (7), 3756-3761.

201.   Kincs, J.; Martin, S. W., Non-Arrhenius conductivity in glass: mobility and conductivity saturation effects. *Physical review letters* **1996,** *76* (1), 70.

202.   Ingram, M. D.; Mackenzie, M. A.; Müller, W.; Torge, M., Cluster and pathways: a new approach to ion migration in glass. *Solid State Ionics* **1988,** *28*, 677-680.

203.   Minami, T., Recent progress in superionic conducting glasses. *JNCS* **1987,** *95*, 107-118.

204.   Tuller, H.; Button, D.; Uhlmann, D. R., Fast ion transport in oxide glasses. *Journal of Non-Crystalline Solids* **1980,** *40* (1-3), 93-118.

205.   Rioux, M.; Ledemi, Y.; Viens, J.; Morency, S.; Ghaffari, S. A.; Messaddeq, Y., Optically-transparent and electrically-conductive AgI–AgPO 3–WO 3 glass fibers. *RSC Advances* **2015,** *5* (50), 40236-40248.

206.   Ohtomo, T.; Hayashi, A.; Tatsumisago, M.; Kawamoto, K., Glass electrolytes with high ion conductivity and high chemical stability in the system LiI-Li2O-Li2S-P2S5. *Electrochemistry* **2013,** *81* (6), 428-431.

207.   Tatsumisago, M.; Okuda, K.; Itakura, N.; Minami, T., Crystallization of α-AgI from AgI–Ag2O–MxOy (MxOy= B2O3, GeO2, WO3) melts and glasses. *Solid State Ionics* **1999,** *121* (1-4), 193-200.

208.   Wicks, J.; Börjesson, L.; Bushnell-Wye, G.; Howells, W.; McGreevy, R., Modelling the structure and ionic conduction of (AgI) x (AgPO3) 1–x glasses. *Physica Scripta* **1995,** *1995* (T57), 127.

209.   Rioux, M.; Ledemi, Y.; Messaddeq, Y., An experimental study of the effect of AgI on the optical and electrical properties of conductive glasses in the system AgI-AgPO 3-WO 3. *Journal of Non-Crystalline Solids* **2017,** *459*, 169-175.

210.   Fergus, J. W., Ceramic and polymeric solid electrolytes for lithium-ion batteries. *Journal of Power Sources* **2010,** *195* (15), 4554-4569.

211.   Song, S.; Duong, H. M.; Korsunsky, A. M.; Hu, N.; Lu, L., A Na+ superionic conductor for room-temperature sodium batteries. *Scientific reports* **2016,** *6*, 32330.

212.   Varshneya, A. K., *Fundamentals of inorganic glasses*. Elsevier: 2013.

213.   Wang, X.; Wei, X.; Dai, H.; Wu, Q. In *State estimation of lithium ion battery based on electrochemical impedance spectroscopy with on-board impedance measurement system*, 2015 IEEE Vehicle Power and Propulsion Conference (VPPC), IEEE: 2015; pp 1-5.

214.   Grossi, M.; Riccò, B., Electrical impedance spectroscopy (EIS) for biological analysis and food characterization: A review. **2017**.